

Boreal Ecosystem Recovery and Assessment (BERA)

Project Outline

Evaluation bird models produced by 1 or more GIS layers: The value of high-density LIDAR data in predicting boreal bird species	
Lead	Name and affiliation of person primarily responsible: Lionel Leston [BERA, Bioacoustic Unit, University of Alberta]
Collaborators	<ul style="list-style-type: none"> Gustavo Lopez Quieroz [BERA, University of Calgary] Mustafizur Rahman [BERA, University of Calgary] Silvia Alejandra Losada [BERA, University of Calgary] Erin Bayne [BERA, Bioacoustic Unit, University of Alberta] Julia Linke [BERA, University of Calgary] Greg McDermid [BERA, University of Calgary]
Data Requirements	<ul style="list-style-type: none"> Avian point count data (provided by the Bioacoustic Unit) Coarse-scale Alberta Vegetation Inventory habitat and footprint data (provided by the Alberta Biodiversity Monitoring Institute) Remote sensing vegetation data (Beaudoin layer) LIDAR point cloud data (provided by Greg McDermid and Mustafizur Rahman)
Project Dependencies & Contingency Plans	<p>Dependencies:</p> <ul style="list-style-type: none"> Transcription of remaining recordings from Kirby Grid (16 stations) Habitat and human footprint for Kirby Grid (Alberta Vegetation Inventory by ABMI, satellite data in Beaudoin layer) Point cloud layer (max veg ht., mean veg ht., pt hits on/near ground/at a certain height above ground (determine what scale of point cloud data, by next week) (available November 20) <p>Contingency Plans:</p> <ul style="list-style-type: none"> Alternate coarse layers available as rasters (Beaudoin layer) or with permission from Al-Pac, possibly Al-Pac AVI layer from 2016 Base analyses just on the already transcribed station data (98 stations)
Deliverables	<ul style="list-style-type: none"> Base model results (no fine-scale data) for 22 species of birds in different guilds or most common species (Nov 6) Interim report (Dec 2019): models incorporating point cloud data, snags, coarse woody debris Interim report (Mar 2019): models incorporating shrub layer (IF AVAILABLE) Final report (May 2020) Published paper (2020-2021)
Status	Start date: September 2019 Status: ongoing Scheduled completion: May 2020

Overview:

Introduction:

The structure of boreal forests in Alberta is changing with increasing forestry and energy sector development. There are much available vegetation and human footprint data at large extents within Alberta's boreal forests for predicting the effects of human footprint on wildlife. These data include both shapefiles (e.g. Alberta Vegetation Inventory, Alberta Biodiversity Monitoring Institute wall-to-wall human footprint and vegetation layer) and remotely sensed data processed into rasters. Given the amount of time spent ground-truthing and digitizing data to shapefiles, Alberta Vegetation Inventory data are not frequently updated, so the quality and accuracy of data is likely to be inconsistent and varying over a large area. There is also a potentially large loss of information when delineating shapefiles, because continuous, quantitative data like tree species composition are frequently summarized and assigned to categories, concealing variation of forest structure that may be important for abundance of some species. In contrast, remotely sensed data from satellites can be used to obtain measurements of vegetation data that are consistent in quality over a large region over a short period of time. However, these data are mainly available at a coarser scale of resolution (e.g. 250-m raster cells) or are summarized for shapefile polygons (e.g. stand type, % cover by dominant species in each stand).

Many recent studies suggest that models of bird abundance are improved by including fine-scale vegetation structural data (e.g. crown height, canopy cover, shrub density) (Bayne, Haché, and Hobson 2010). However, fine-scale vegetation data collected from field surveys are time-consuming and labor-intensive to obtain even over small extents, and the improvement in model fit from including fine-scale data may be insufficient relative to the expended effort (Bayne, Haché, and Hobson 2010).

Newer remote sensing techniques like LIDAR (Light Detection and Ranging) have become widespread and have been used to efficiently quantify fine-scale vegetation structure over large areas. Some recent studies have employed LIDAR based vegetation metrics at point count locations to predict bird abundance, and these studies have found that incorporating LIDAR-based fine-scale vegetation structural variables into models improves predictions of bird abundance (e.g. Hinsley et al. 2002, Hill and Thompson 2005, Broughton et al. 2006, Boehlmann et al. 2007, Clawges et al. 2008, Graf et al. 2009, Martinuzzi et al. 2009, Muller et al. 2009, Goetz et al. 2010, Muller et al. 2010, Seavy et al. 2009, Lesak et al. 2011, Tattoni et al. 2012, Wilsey et al. 2012, Vogeler et al. 2013, Eldegard et al. 2014, Garabedian et al. 2014, Vierling et al. 2014). Many of these studies have focused on single species or a few species. How well different kinds of point cloud metrics predict abundance of birds in different guilds or having different forest habitat requirements has not been assessed.

Objectives:

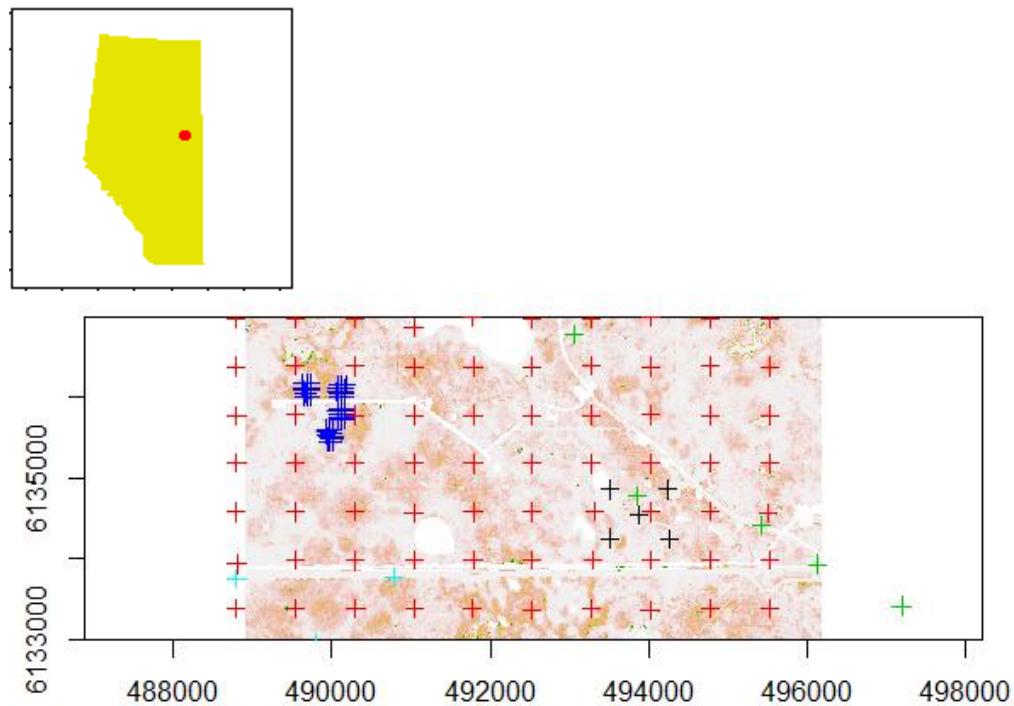
To model how well abundance of boreal bird species (species present at 10 % of sites) are predicted by different kinds of spatial data, from coarse-scale remotely sensed layers from satellites (e.g. Beaudoin layer [Beaudoin et al. 2013]) and forest resource inventory shapefiles (e.g. Alberta Vegetation Inventory [Alberta Biodiversity Monitoring Institute 2019]) to fine-scale LIDAR point cloud data. We will also evaluate whether 1) models containing variables from multiple sources predict bird abundance better than models containing variables from a single data source; and 2) whether averaged predicted abundances of each species from all data sources are more accurate than predicted abundances of species based on a single data source.

We predict that models including or using fine-scale data from LIDAR-based point clouds will predict bird abundance better than models that use only coarse-scale vegetation data. We also predict that averaging predictions of bird abundance from different methods may result in more accurate estimates of bird abundance than predictions based on a single kind of vegetation data.

Study Site:

The “Kirby” grid ~45 minutes north of Calling Lake (UTMs: 489525-494943, 6131568-6136993). If similar coarse-scale and fine-scale remote-sensed data are available alongside point count data outside of the Kirby grid in Alberta’s boreal forest region, then a larger study area might be considered. We will be using indices of bird abundance from autonomous recording unit (ARU) stations, and individual recordings (3-4 per station) will be the unit of analysis. Data consists of counts of each species detected in each recording; actual abundance is not known but estimated.

Figure 1. Location of Kirby grid in Alberta.



Study Species:

The most common species, in terms of the number of stations with at least one detection of a given species, are: Alder Flycatcher (*Empidonax alnorum*), American Robin (*Turdus migratorius*), Boreal Chickadee (*Poecile hudsonicus*), Cedar Waxwing (*Bombycilla cedrorum*), Chipping Sparrow (*Spizella passerina*), Common Yellowthroat (*Geothlypis trichas*), Dark-eyed Junco (*Junco*

hyemalis), Gray Jay (*Perisoreus canadensis*), Hermit Thrush (*Catharus guttatus*), Le Conte's Sparrow (*Ammodramus lecontei*), Lincoln's Sparrow (*Melospiza lincolni*), Olive-sided Flycatcher (*Contopus cooperi*), Ovenbird (*Seiurus aurocapillus*), Palm Warbler (*Setophaga palmarum*), Red-eyed Vireo (*Vireo olivaceus*), Ruby-crowned Kinglet (*Regulus calendula*), Swainson's Thrush (*Catharus ustulatus*), Swamp Sparrow (*Melospiza georgiana*), Tennessee Warbler (*Leiothlypis peregrina*), White-throated Sparrow (*Zonotrichia albicollis*), Winter Wren (*Troglodytes hiemalis*), and Yellow-rumped Warbler (*Setophaga coronata*). We ran models for these species.

Six of these species (Boreal Chickadee, Gray Jay, Ruby-crowned Kinglet, Swainson's Thrush, Winter Wren, and Yellow-rumped Warbler) are associated with boreal forests older than 80 years and Ovenbirds are most abundant in mature boreal forests (~60-80 years old). These species would be predicted to be more abundant at sites with a greater density of LIDAR points higher above the ground. The remaining species are habitat generalists or associated with younger boreal forests. At least some of these species would be predicted to be more abundant at sites with a greater density of LIDAR points closer to the ground.

Five of the 20 species (Dark-eyed Junco, Le Conte's Sparrow, Lincoln's Sparrow, Ovenbird, Palm Warbler, White-throated Sparrow) are shrub or ground nesters whose numbers are predicted to be strongly related to the density of LIDAR points closer to the ground. Such species are also predicted to vary with the amount of coarse woody debris on the ground, given that the amount of coarse woody debris might influence the amount of other ground cover types (e.g. bare ground, herbaceous vegetation, woody vegetation).

Fifteen of the 20 species are tree-nesting species that are predicted to vary with the density of LIDAR points higher above the ground. One species (Red-breasted Nuthatch) is a cavity nester that is predicted to increase with the density of snags.

Methods:

Bird Data: We used autonomous recording units (ARUs: Model SM4, Wildlife Acoustics Inc., Maynard, MA) to generate repeated point counts of bird abundance at the Kirby Grid in the summer of 2018. Point count stations were 600 m apart within a 10x10 grid. At each station location, field technicians located a tree that was large and strong enough to support the weight of an ARU screwed into the trunk on the north side of the tree, but whose diameter at breast height (~1.5 m) was small enough (~15 cm or less) that the trunk did not block the microphones on either side of the ARU from picking up sounds on the south side of the tree. Each ARU was attached at about breast height (~1.5 m) to the tree and was programmed to turn on for at least one 5-minute recording each day around sunrise (4:52 AM – 5:06 AM local time) until the ARU was either retrieved and returned to the lab or redeployed to another station location. When retrieved or redeployed, all recordings from a given location were stored within 1 or more SD cards inside the ARU: these SD cards were replaced with new cards if the ARU was redeployed to another location in the same season. We used recordings from May 20 to July 11 in our analyses. In the lab, field technicians listened to recordings and transcribed the number of distinct individuals heard from each species as a measure of abundance counted within each station visit. Technicians also recorded the date and time of day of individual recordings and estimated qualitative values of environmental variables within the recordings such as the strength of wind, rain, or environmental noise, which affect the probability of detecting birds

that are present. Up to 4 recordings per station that did not have excessive noise from wind, rain or other environmental noise were randomly selected and transcribed for the analyses in this paper.

Vegetation data from GIS layers: We summarized vegetation data from 3 kinds of GIS layers around ARU stations. We used 50-m, 150-m, and 500-m buffer zones around each point count for data extraction, to assess whether data from one particular spatial scale better predicted abundance of a species. Previous studies have summarized LIDAR and other spatial vegetation data at the extent of a study species' territory size or found that different species responded most strongly to LIDAR variables at a variety of spatial scales. Based on territory sizes reported in the literature, Gray Jays are predicted to respond most strongly at the 500-m scale (Bowman 2003); Chipping Sparrow, Red-breasted Nuthatch, and Winter Wren are predicted to respond most strongly at the 150-m scale (Odum et al. 1955, Matthysen et al. 1992, Toews and Irwin 2008); and the remaining species are predicted to respond most strongly to LIDAR data at the 50-m scale (Morse 1976, Wasserman 1980, Chandler et al. 1994, Wortman-Wunder 1997, Evans et al. 2000, Bowman 2003, Bourque and Desrochers 2006).

We obtained vegetation shapefile data (Alberta Vegetation Inventory) from Alberta Biodiversity Monitoring Institute. Shapefile data include the proportion of each 50, 150, and 500-m buffer occupied by a particular tree species or treed habitat (black spruce, jack pine, swamp, tamarack, trembling aspen, white birch, white spruce), non-treed-habitat (bog, fen, grassland, marsh shrubland), or water, and the weighted age of any forest stands within those buffers. In the original data, some stand types dominated by a particular tree species were further delineated according to secondary tree species (e.g. white spruce vs. white spruce/mixedwood-wet). The proportions of different stand types dominated by a particular species were summed together to simplify modelling (e.g. white spruce = white spruce + white spruce/mixedwood-wet).

We used remotely sensed Canada-wide vegetation data at 250-m resolution, described in Beaudoin et al. (2013). Vegetation layers from the Beaudoin rasters included the following variables used as predictors in models: the proportion of each cell dominated by different tree species, all broadleaf species combined, and all needle-leaved species combined; the biomass attributed to branches, foliage, stem bark, stem wood, total dead vegetation, total live above-ground vegetation, stand age, crown closure, stand height; vegetated and non-vegetated land cover; treed and non-treed vegetated cover (Table 1). To obtain the “buffers” for these data, we used a Gaussian filter (focalweight function in raster package [Hijmans and van Etten 2012]) to characterize vegetation and terrain variables at different spatial scales, with 50 m, 150 m, and 500 m selected as the distances for defining our filters. Gaussian filters differ from traditional GIS buffers in that features are weighted according to feature distance from point counts and the amount of weight is described by a Gaussian function, with more distant features carrying gradually less weight. Gaussian functions are partially defined by a distance value that determines when weights strongly decrease, and a Gaussian function with a larger distance threshold is analogous to a GIS buffer with a larger radius. A traditional GIS buffer would assign equal weight to all examples of a feature within the buffer radius whether or not those features are next to a point count or at the buffer periphery. A traditional GIS buffer also assigns very different weights to features that are just barely located on either side of a buffer boundary, which is unrealistic (Chandler and Hepinstall-Cymerman 2016) (Table 1).

Table 1. Predictors from remote-sensed data (Beaudoin 2013) used in mixture models of boreal bird abundance within a grid of autonomous recording unit point count stations in northern Alberta, 2018-2019. X indicates if a given predictor's effect was analyzed at a particular spatial scale (50, 150, or 500 m).

Predictor	Source	Unit of Measurement	50-m	150-m	500-m
<i>Abies balsamifera</i> (Species_Abie_Bal)	Beaudoin	%	X	X	X
<i>Abies lasiocarpa</i> (Species_Abie_Las)	Beaudoin	%	X	X	X
<i>Acer negundo</i> (Species_Acer_Neg)	Beaudoin	%	X	X	X
<i>Alnus</i> spp. (Species_Alnu_Spp)	Beaudoin	%	X	X	X
<i>Betula papyrifera</i> (Species_Betu_Pap)	Beaudoin	%	X	X	X
<i>Larix laricina</i> (Species_Lari_Lar)	Beaudoin	%	X	X	X
<i>Picea engelmanni</i> (Species_Pice_Eng)	Beaudoin	%	X	X	X
<i>Picea glauca</i> (Species_Pice_Gla)	Beaudoin	%	X	X	X
<i>Picea mariana</i> (Species_Pice_Mar)	Beaudoin	%	X	X	X
<i>Pinus alba</i> (Species_Pinu_Alb)	Beaudoin	%	X	X	X
<i>Pinus banksiana</i> (Species_Pinu_Ban)	Beaudoin	%	X	X	X
<i>Pinus contorta</i> (Species_Pinu_Con)	Beaudoin	%	X	X	X
<i>Pinus ponderosa</i> (Species_Pinu_Pon)	Beaudoin	%	X	X	X
<i>Populus balsamifera</i> (Species_Popu_Bal)	Beaudoin	%	X	X	X
<i>Populus tremuloides</i> (Species_Popu_Tre)	Beaudoin	%	X	X	X
<i>Prunus pensylvanicus</i> (Species_Prun_Pen)	Beaudoin	%	X	X	X
<i>Pseudotsuga mensiezii</i> (Species_Pseu_Men)	Beaudoin	%	X	X	X
<i>Salix</i> spp. (Species_Sali_Spp)	Beaudoin	%	X	X	X
SpeciesGroups_Broadleaf	Beaudoin	%	X	X	X
SpeciesGroups_Needleleaf	Beaudoin	%	X	X	X
Structure_Biomass_Branch	Beaudoin	Numeric	X	X	X
Structure_Biomass_Foliage	Beaudoin	Numeric	X	X	X
Structure_Biomass_StemBark	Beaudoin	Numeric	X	X	X
Structure_Biomass_StemWood	Beaudoin	Numeric	X	X	X
Structure_Biomass_TotalDead	Beaudoin	Numeric	X	X	X
Structure_Biomass_TotalLiveAboveGround	Beaudoin	Numeric	X	X	X
Structure_Stand_Age	Beaudoin	Numeric	X	X	X
Structure_Stand_CrownClosure	Beaudoin	Numeric	X	X	X
Structure_Stand_Height	Beaudoin	Numeric	X	X	X
LandCover_NonVeg	Beaudoin	%	X	X	X
LandCover_Veg	Beaudoin	%	X	X	X
LandCover_Veg_Treed	Beaudoin	%	X	X	X
LandCover_VegNonTreed	Beaudoin	%	X	X	X

Lidar data: Data consisted of mean maximum height of hits, standard deviation in percent canopy cover, and the density of point returns within 0.5-m and 1-m height intervals off the ground that were collected when scanning the Kirby Grid (Lesak et al. 2011). The density of point returns within lower height intervals (e.g. 0.5-1, 1-1.5, 1.5-2 m) can be used to indicate shrubby understory (Wilsey et al. 2012), while point return density in greater height intervals

can indicate canopy vegetation (Vogeler et al. 2013). The raw point returns can then be summarized at two spatial scales. First, the points can be summarized within a fine-resolution raster layer like an intermediate digital elevation/terrain/surface model (e.g. 1 m to distinguish individual shrubs) to identify denser spots and gaps in canopy vegetation and shrubby understory (Broughton et al. 2006, Boehlmann et al. 2007, Graf et al. 2009, Eldegard et al. 2014, Garabedian et al. 2014). Percent cover of point returns is defined as the percentage of points within each 1-m pixel that are at or above one of the four cut-off heights out of all point returns including the ground points.

Analysis: We used *N*-mixture models (Royle and Nichols 2005) to account for varying detection probability across sites and visits (Anderson 2001) when predicting effects of each GIS layer's variables on bird abundance across multiple visits. The basic *N*-mixture model assumes 1) population closure, i.e. animal numbers do not change during the survey period due to births, deaths, immigration or emigration, and 2) independence of survey locations. Since survey points in our study were within a grid, abundance or occupancy may be more strongly correlated at points closer to each other in space, violating the second assumption. We tested for spatial autocorrelation by first running generalized least-squares models using the gls function in the nlme package in R (Pinheiro et al. 2017), in which we used the variables from different GIS layers to predict mean count of each species per visit at each station. We generated variograms for the model residuals for each species and assessed how pairwise variance in residuals changed with distance between stations and at what distance pairwise variance no longer increased, i.e. spatial autocorrelation became insignificant. We determined from these variograms that spatial autocorrelation was generally not significant across species; thus we opted to run non-spatial mixture models using the unmarked package in R (Fiske and Chandler 2011), rather than using spatial mixture models in the hSDM package in R (Vieilledent et al. 2015).

We used the MuMin package (Barton and Barton 2019) to initially evaluate 9 model sets for each bird species: 3 model sets containing only AVI-based predictors at the 50-m, 150-m, and 500-m spatial scales; 3 model sets containing only satellite-based predictors at the 50-m, 150-m, and 500-m spatial scales; and 3 model sets containing only LIDAR-based predictors at the 50-m, 150-m, and 500-m spatial scales. The dredge function in the MuMin package was used to select the combination of abundance covariates from a GIS layer and detection covariates (either a null model or a model with the Julian date of a recording) with the lowest AIC in each model set. To reduce processing time and issues of multicollinearity, we excluded models with > 3 abundance and/or detection covariates and predictors with correlation coefficients whose absolute values were > 0.7.

Averaging predictions from the separate models: We obtained estimated abundance of each species at each station from the AVI, Beaudoin, and LIDAR-based vegetation models and compared estimated abundance against the maximum count of each species at each station, to assess how well models based on different kinds of GIS data predicted species counts at each station. We then calculated an average predicted abundance for each species at each station from the 3 kinds of predictions based on AVI, Beaudoin, and LIDAR-based vegetation models, to see if the average prediction performed better than the individual model predictions.

Combining predictors from different GIS data: For each species, we identified the predictors with the strongest influence on bird abundance at each station by generating 95 % confidence intervals for the point estimates of each predictor. We selected those predictors from each

model whose confidence interval limits were both negative or both positive and excluded zero. We then combined these predictors in a fourth N-mixture model for each species to determine if combining predictors from different kinds of GIS data resulted in more accurate predictions of species.

For the top AVI, satellite, lidar, and composite models, we assessed the goodness-of-fit of the model by testing for overdispersion in Dunn-Smyth residuals (marginal, site-sum, observation), in which $c\text{-hat}$ values closer to 1 indicated acceptable fit and $c\text{-hat}$ values $>> 1$ indicated overdispersion. We also plotted residuals against fitted values to check for heteroscedasticity and plotted residuals within Q-Q plots to assess normality in the residuals (Knape et al. 2017).

To compare if averaged predicted abundances of each species from each kind of data source, we generated maps where predicted abundances were averaged from the predictions of the top AVI, satellite and lidar models, and we compared those mean predictions to the predictions from the top composite model, for those species in which a composite model better explained abundance than models based on a single data source.

Results:

Alder Flycatcher. Alder Flycatcher detection probability increased with Julian day in general and abundance was positively associated with variables in the different GIS layers related to short deciduous vegetation. In the AVI layer, Alder Flycatcher abundance was most strongly predicted by and negatively related to the amount of black spruce within 500 m (Fig. 2). In the satellite layer, abundance increased with the proportion of trembling aspen within 50 m and decreased with the total live above-ground biomass within 50 m (Fig. 3). In the lidar layer, abundance increased with standard deviation in percent canopy density and density of hits 1-1.5 m above ground and decreased with density of hits 1.5-2 m above ground, within 150 m (Fig. 4). When variables from different layers were modelled together, a composite model best predicted Alder Flycatcher abundance. In the composite model, Alder Flycatcher abundance was best predicted by and increased with the proportion of trembling aspen within 50 m and standard deviation in percent canopy density within 150 m (Fig. 5).

American Robin. American Robin detection probability decreased with Julian day in general and abundance was positively associated with variables in the different GIS layers related to short vegetation. In the AVI layer, American Robin abundance decreased with weighted mean forest age and increased with the amounts of bog and shrubland habitats within 500 m (Fig. 6). In the satellite layer, abundance decreased with the proportion of balsam fir within 500 m and increased with the total dead above-ground biomass within 500 m (Fig. 7). In the lidar layer, abundance decreased with mean maximum height of hits and increased with the density of hits 4-5 m above ground, within 150 m (Fig. 8). When variables from different layers were modelled together, a composite model best predicted American Robin abundance. In the composite model, American Robin abundance decreased with mean maximum height of hits within 150 m and the proportion of balsam fir within 500 m and increased with the total dead above-ground biomass within 500 m (Fig. 9).

Boreal Chickadee. Boreal Chickadee abundance was positively associated with variables in the different GIS layers related to older, shorter coniferous forests. In the AVI layer, Boreal Chickadee abundance increased with weighted mean forest age and decreased with the

amounts of trembling aspen and open water within 50 m (Fig. 10). In the satellite layer, abundance increased with the proportions of balsam fir and willow within 500 m and with the weighted average forest age within 500 m (Fig. 11). In the lidar layer, abundance increased with the density of hits 3-4 m above ground, within 150 m (Fig. 12). When variables from different layers were modelled together, a composite model best predicted Boreal Chickadee abundance. In the composite model, Boreal Chickadee abundance increased with weighted mean forest age from the AVI layer within 50 m and the density of hits 3-4 m above ground from the lidar layer within 150 m, and decreased with the amounts of trembling aspen from the AVI layer within 50 m (Fig. 13). Boreal Chickadee abundance was overpredicted by the AVI and satellite layers and model had low goodness-of-fit according to examination of Dunn-Smyth model residuals.

Cedar Waxwing. Cedar Waxwing detection probability decreased with Julian day and abundance was positively associated with variables in the different GIS layers related to shorter deciduous vegetation. In the AVI layer, Cedar Waxwing abundance increased with the amount of birch and decreased with the amount of black spruce within 150 m (Fig. 14). Abundance was not well predicted by any satellite layer variables, in that the null model had a lower AIC than any variables at any spatial scale (Fig. 15). In the lidar layer, abundance increased with the density of hits 0.5-1 m above ground and decreased with the density of hits 1.5-2 m above ground, within 500 m (Fig. 16). When variables from different layers were modelled together, the top AVI model was more parsimonious than any satellite model, lidar model, or composite model (Fig. 17). Cedar Waxwing was overpredicted by models except for AVI variables at the 500-m scale, and models had low goodness-of-fit based on analyses of Dunn-Smyth model residuals.

Chipping Sparrow. Chipping Sparrow abundance was positively associated with variables in the different GIS layers related to shorter coniferous forests. In the AVI layer, Chipping Sparrow abundance decreased with the amount of trembling aspen within 50 m (Fig. 18). In the satellite layer, abundance decreased with the proportion of all broad-leaved trees and total live above-ground biomass within 500 m (Fig. 19). In the lidar layer, abundance increased with standard deviation in percent canopy cover and density of hits 4-5 m above ground, and decreased with mean maximum height, within 150 m (Fig. 20). When variables from different layers were modelled together, a composite model best predicted Chipping Sparrow abundance. In the composite model, Chipping Sparrow abundance increased with standard deviation in percent canopy cover and density of hits 4-5 m above ground within 150 m, decreased with mean maximum height within 150 m, and decreased with total above-ground biomass within 500 m (Fig. 21). Chipping Sparrow was overpredicted by LIDAR variables at the 150-m but not the 500-m scale.

Common Yellowthroat. Common Yellowthroat abundance was positively associated with variables in the different GIS layers related to shorter vegetation. In the AVI layer, Common Yellowthroat abundance increased with shrubland and decreased with the amounts of trembling aspen and black spruce within 50 m (Fig. 22). In the satellite layer, abundance decreased with crown closure, non-vegetated cover, and cover of all needle-leaved tree species within 500 m (Fig. 23). In the lidar layer, abundance increased with the density of hits 1-1.5 m above ground and decreased with mean maximum height and density of hits 1.5-2 m above ground, within 150 m (Fig. 24). When variables from different layers were modelled together, a composite model best predicted Common Yellowthroat abundance. In the lidar layer, abundance increased with the density of hits 1-1.5 m above ground and decreased with density

of hits 1.5-2 m above ground, within 150 m, and decreased with the amounts of trembling aspen from the AVI layer within 50 m (Fig. 25). However, while trembling aspen was selected in the top AVI and composite models, there was a high amount of uncertainty associated with its estimated effect size.

Dark-eyed Junco. Dark-eyed Junco abundance was positively associated with variables in the different GIS layers related to coniferous forests and dense understory. In the AVI layer, Dark-eyed Junco abundance increased with the amounts of black spruce, jack pine, and tamarack within 150 m (Fig. 26). In the satellite layer, abundance decreased with the proportion of black spruce within 50 m but increased with the proportion of all needle-leaved trees and total dead above-ground biomass within 50 m (Fig. 27). In the lidar layer, abundance increased with density of hits 1-1.5 m and 3-4 m above ground, within 150 m (Fig. 28). When variables from different layers were modelled together, a composite model best predicted Dark-eyed Junco abundance. In the composite model, Dark-eyed Junco abundance increased with the density of hits 3-4 m above ground within 150 m, and increased with the amounts of black spruce and tamarack within 150 m (Fig. 29).

Gray Jay. Gray Jay detection probability increased with Julian day and abundance was positively associated with variables in the different GIS layers related to open coniferous forests. In the AVI layer, Gray Jay abundance decreased with the amounts of trembling aspen and white birch within 150 m (Fig. 30). In the satellite layer, abundance decreased with crown closure and the proportion of willow within 50 m but increased with the proportion of jack pine within 50 m (Fig. 31). In the lidar layer, abundance increased with increasing standard deviation in percent canopy cover and density of hits 2-3 m above ground, within 500 m (Fig. 32). When variables from different layers were modelled together, a composite model best predicted Gray Jay abundance. In the composite model, Gray Jay abundance increased with increasing standard deviation in percent canopy cover and decreased with increasing aspen cover from the AVI layer and willow cover from the satellite layer (Fig. 33).

Hermit Thrush. Like Gray Jay, Hermit Thrush detection probability increased with Julian day and abundance was positively associated with variables in the different GIS layers related to open coniferous forests. In the AVI layer, Hermit Thrush abundance decreased with the amounts of trembling aspen and shrubland within 150 m (Fig. 34). In the satellite layer, abundance decreased with the total live above-ground biomass within 500 m but increased with the proportion of jack pine within 500 m (Fig. 35). In the lidar layer, abundance increased with increasing standard deviation in percent canopy cover and density of hits 2-3 m above ground, within 500 m (Fig. 36). When variables from different layers were modelled together, a composite model best predicted Hermit Thrush abundance. In the composite model, Hermit Thrush abundance decreased with the total live above-ground biomass within 500 m but increased with the proportion of jack pine and density of hits 2-3 m above ground, within 500 m (Fig. 37).

Le Conte's Sparrow. Le Conte's Sparrow abundance was positively associated with variables in the different GIS layers related to open tamarack wetlands. In the AVI layer, Le Conte's Sparrow abundance decreased with the amounts of swamp and white spruce and increased with the amounts of tamarack within 150 m (Fig. 38). In the satellite layer, abundance decreased with increasing crown closure and non-vegetated land within 50 m (Fig. 39). In the lidar layer, abundance increased with increasing standard deviation in percent canopy cover and decreased

with increasing density of hits 1.5-2 and 10-11 m above ground, within 150 m (Fig. 40). When variables from different layers were modelled together, a composite model best predicted Le Conte's Sparrow abundance. In the composite model, Le Conte's Sparrow abundance increased with increasing amount of tamarack and standard deviation in percent canopy cover within 150 m but decreased with increasing density of hits 1.5-2 m above ground, within 150 m (Fig. 41).

Lincoln's Sparrow. Lincoln's Sparrow detection probability decreased with Julian date and abundance was positively associated with variables in the different GIS layers related to open tamarack wetlands. In the AVI layer, Lincoln's Sparrow abundance decreased with the amount of trembling aspen and increased with the amounts of tamarack within 150 m (Fig. 42). In the satellite layer, abundance decreased with increasing crown closure and proportion of all needle-leaved tree species combined within 150 m (Fig. 43). In the lidar layer, abundance decreased with increasing density of hits 2-3 and 10-11 m above ground, within 150 m (Fig. 44). When variables from different layers were modelled together, the top lidar model predicted Lincoln's Sparrow abundance better than the top AVI, satellite, and composite models (Fig. 45). Lincoln's Sparrow was overpredicted by lidar variables at the 150-m but not the 500-m scale.

Olive-sided Flycatcher. Olive-sided Flycatcher abundance was positively associated with variables in the different GIS layers related to short white spruce. In the AVI layer, Olive-sided Flycatcher abundance decreased with increasing amounts of pine, shrubland, and trembling aspen within 500 m (Fig. 46). In the satellite layer, abundance decreased with increasing crown closure and proportion of nonvegetated land within 500 m but increased with the amount of white spruce within 500 m (Fig. 47). In the lidar layer, abundance decreased with increasing density of hits 2-3 and 9-10 m above ground, within 500 m but increased with increasing density of hits 1-1.5 m above ground (Fig. 48). When variables from different layers were modelled together, the top lidar model predicted Olive-sided Flycatcher abundance better than the top AVI, satellite, and composite models (Fig. 49).

Ovenbird. Ovenbird detection probability decreased with Julian date and abundance was positively associated with variables in the different GIS layers related to older, taller broadleaf stands. In the AVI layer, Ovenbird abundance decreased with the amount of birch and increased with the amounts of trembling aspen within 500 m (Fig. 50). In the satellite layer, abundance decreased with increasing proportion of white spruce and increased with increasing stand age and proportion of all broad-leaved tree species within 500 m (Fig. 51). In the lidar layer, abundance increased with increasing mean maximum height and density of hits 1-1.5m above ground, within 150 m (Fig. 52). When variables from different layers were modelled together, the top AVI model predicted Ovenbird abundance better than the top satellite, lidar, and composite models (Fig. 53).

Palm Warbler. Palm Warbler abundance was positively associated with variables in the different GIS layers related to shorter conifers with shrubs or wet areas. In the AVI layer, Palm Warbler abundance decreased with the amount of fen and trembling aspen and increased with the amounts of swamp within 150 m (Fig. 54). In the satellite layer, abundance decreased with increasing crown closure and increased with increasing proportion of all needle-leaved tree species after accounting for total needle-leaf cover, also the proportion of white spruce within 500 m (Fig. 55). In the lidar layer, abundance increased with increasing density of hits 0.5-1 m above ground and decreased with density of hits 1-1.5 and 10-11 m above ground, within 500 m (Fig. 56). When variables from different layers were modelled together, a composite model best

predicted Palm Warbler abundance. In the composite model, Palm Warbler abundance increased with increasing swamp within 150 m but decreased with increasing fen within 150 m and increasing density of hits 10-11 m above ground, within 500 m (Fig. 57). Palm Warbler was overpredicted by the top models for all layers, and models had low goodness-of-fit based on analyses of Dunn-Smyth model residuals.

Red-eyed Vireo. Red-eyed Vireo detection probability increased with Julian date and abundance was positively associated with variables in the different GIS layers related to older, taller broadleaf stands. In the AVI layer, Red-eyed Vireo abundance decreased with the amount of birch and increased with the amounts of trembling aspen and white spruce within 500 m (Fig. 58). In the satellite layer, abundance decreased with increasing total live above-ground biomass and proportion of willow and increased with increasing crown closure within 500 m (Fig. 59). In the lidar layer, abundance increased with increasing mean maximum height, within 500 m (Fig. 60). When variables from different layers were modelled together, a composite model best predicted Red-eyed Vireo abundance. In the composite model, Red-eyed Vireo abundance increased with increasing amount of trembling aspen from the AVI layer within 500 m but decreased with increasing birch from the AVI layer and willow from the satellite layer, within 500 m (Fig. 61).

Ruby-crowned Kinglet. Ruby-crowned Kinglet detection probability decreased with Julian date and abundance was positively associated with variables in the different GIS layers related to coniferous forests including balsam fir. In the AVI layer, Ruby-crowned Kinglet abundance decreased with the amount of white spruce within 150 m (Fig. 62). In the satellite layer, abundance increased with the proportion of all needle-leaved tree species combined within 500 m, and with the amount of balsam fir (Fig. 63). In the lidar layer, abundance increased with increasing density of hits 5-6 m above ground, within 150 m (Fig. 64). When variables from different layers were modelled together, a composite model best predicted Ruby-crowned Kinglet abundance. In the composite model, Ruby-crowned Kinglet abundance increased with the amount of balsam fir from the satellite layer within 500 m and with the density of hits 5-6 m above ground, within 150 m (Fig. 65).

Swainson's Thrush. Swainson's Thrush abundance was positively associated with variables in the different GIS layers related to older coniferous forests. In the AVI layer, Swainson's Thrush abundance decreased with the amount of open water and increased with amounts of shrubland and white spruce within 500 m (Fig. 66). In the satellite layer, abundance increased with stand age and the proportion of jack pine within 150 m, and decreased with the amount of willow (Fig. 67). In the lidar layer, abundance increased with increasing density of hits 1-1.5 and 2-3 m above ground and decreased with the density of hits 1.5-2 m above ground, within 500 m (Fig. 68). When variables from different layers were modelled together, the top satellite model predicted Swainson's Thrush abundance better than the top AVI, top lidar, and top composite model (Fig. 69).

Swamp Sparrow. Swamp Sparrow detection probability decreased with Julian date and abundance was positively associated with variables in the different GIS layers related to shrublands. In the AVI layer, Swamp Sparrow abundance increased with the amounts of shrubland and tamarack within 150 m (Fig. 70). In the satellite layer, abundance decreased with increasing crown closure and nonvegetated land and increased with the total live above-ground biomass within 150 m (Fig. 71). In the lidar layer, abundance increased with increasing density of

hits 1-1.5 m above ground and decreased with mean maximum height and the number of hits 1.5-2 m above ground, within 150 m (Fig. 72). When variables from different layers were modelled together, a composite model best predicted Swamp Sparrow abundance. In the composite model, Swamp Sparrow abundance increased with the amount of shrubland and tamarack and decreased with the amount of non-vegetated land, within 150 m (Fig. 73). Swamp Sparrow was overpredicted by the top models for the AVI, lidar, and composite layers, and models had low goodness-of-fit based on analyses of Dunn-Smyth model residuals.

Tennessee Warbler. Tennessee Warbler detection probability decreased with Julian date and abundance was positively associated with variables in the different GIS layers related to broad-leaved forests. In the AVI layer, Tennessee Warbler abundance increased with the amounts of trembling aspen and fen and decreased with the amount of swamp within 500 m (Fig. 74). In the satellite layer, abundance increased with increased with the proportion of all broad-leaved tree species but decreased with the proportion of willow within 500 m (Fig. 75). In the lidar layer, abundance increased with increasing density of hits 1-1.5 and 3-4 m above ground and decreased with mean maximum height and the number of hits 1.5-2 m above ground, within 150 m (Fig. 76). When variables from different layers were modelled together, a composite model best predicted Tennessee Warbler abundance. In the composite model, Tennessee Warbler abundance increased with the amounts of fen from the AVI layer and all broad-leaved tree species from the satellite layer and decreased with the amount of swamp from the AVI layer, within 500 m (Fig. 77).

Winter Wren. Winter Wren detection probability decreased with Julian date and abundance was positively associated with variables in the different GIS layers related to older forests. In the AVI layer, Winter Wren abundance decreased with the amount of white spruce and with weighted mean forest age within 500 m (Fig. 78). In the satellite layer, abundance increased with increased with the total amount of live above-ground biomass within 500 m (Fig. 79). In the lidar layer, abundance increased with the density of hits 8-9 and 10-11 m above ground and decreased with density of hits 9-10 m above ground, within 500 m (Fig. 80). When variables from different layers were modelled together, the top lidar model predicted Winter Wren abundance better than the top AVI, top satellite, and top composite model (Fig. 81).

White-throated Sparrow. White-throated Sparrow detection probability decreased with Julian date and abundance was positively associated with variables in the different GIS layers related to older and open broad-leaved forests. In the AVI layer, White-throated Sparrow abundance increased with the amounts of open water and trembling aspen and with weighted mean forest age within 500 m (Fig. 82). In the satellite layer, abundance increased with increased with the proportion of balsam poplar and non-vegetated land but decreased with the amount of willow within 500 m (Fig. 83). In the lidar layer, abundance increased with increasing standard deviation in percent canopy density, within 150 m (Fig. 84). When variables from different layers were modelled together, a composite model best predicted White-throated Sparrow abundance. In the composite model, White-throated Sparrow abundance increased with weighted average forest age from the AVI layer and proportion of balsam poplar from the satellite layer and decreased with the proportion of willow from the satellite layer (Fig. 85).

Yellow-rumped Warbler. Yellow-rumped Warbler detection probability decreased with Julian date and abundance was positively associated with variables in the different GIS layers related

to coniferous forests. In the AVI layer, Tennessee Warbler abundance increased with the amount of jack pine within 50 m (Fig. 86). In the satellite layer, abundance increased with increased with the proportion of white spruce but decreased with the amount of dead above-ground biomass within 50 m (Fig. 87). In the lidar layer, abundance decreased with the number of hits 3-4 and 4-5 m above ground, within 150 m (Fig. 88). When variables from different layers were modelled together, a composite model best predicted Yellow-rumped Warbler abundance. In the composite model, Yellow-rumped Warbler abundance increased with the amounts of pine from the AVI layer and white spruce from the satellite layer, within 50 m (Fig. 89).

Averaging predictions from different GIS layers vs. composite model predictions. When we averaged the predicted abundances from the top AVI, satellite and lidar models and compared the locations of those predicted abundances with predictions from the composite models, the two kinds of predictions identified the same stations with highest predicted abundance for many, though not all of the bird species analyzed (Figs. 90-94). When abundance was predicted by taking the mean of the top AVI, satellite, and lidar model predictions it tended to be lower than predicted abundance from the composite model for most species. For extremely overpredicted species like Cedar Waxwing, Palm Warbler, and Swamp Sparrow, predicted abundance was still extremely high when based on means from the top AVI, satellite, and lidar models.

Discussion:

Nearly two-thirds (64%) of the analyzed bird species were either best predicted by lidar variables or by a composite model that included lidar variables. Species that were associated with older forests were not usually better predicted by higher density of LIDAR points at greater heights above ground: although Ruby-crowned Kinglet and Winter Wren were more abundant in forests with more vegetation 5-6 and 10-11 m above ground respectively, other species (Boreal Chickadee, Gray Jay, Swainson's Thrush) were more abundant at sites with more vegetation near the ground. Some tree-nesting habitat generalists like Chipping Sparrow and American Robin increased at sites with a greater density of hits 4-5 m above ground. Some species associated with taller broad-leaved forests increased with mean maximum height of lidar hits (e.g. Ovenbird, Red-eyed Vireo) and several species increased with standard deviation in percent canopy density (Alder Flycatcher, Chipping Sparrow, Gray Jay, Hermit Thrush, Le Conte's Sparrow, White-throated Sparrow), which could reflect a mosaic of denser forest patches with open areas. Other species that are associated with shrublands, open lands or younger forests increased with the density of lidar hits closer to the ground (e.g. Alder Flycatcher, Cedar Waxwing, Common Yellowthroat, Dark-eyed Junco, Olive-sided Flycatcher, Palm Warbler, Swamp Sparrow, Tennessee Warbler) or decreased with mean maximum height of lidar hits (e.g. American Robin).

Most (73%) of the bird species that were analyzed were best predicted by a model that combined variables from multiple GIS layers, suggesting that shapefile, satellite, and lidar data may have distinct characteristics from each other that are useful for modelling bird abundance. The AVI and satellite layers contain information on dominant tree species or habitat types that are missing from lidar data, while lidar data contains information about vegetation density at different height intervals. While some AVI and satellite variables like stand height or above-ground biomass may be correlated with vegetation density, these layers do not provide the same detailed information about how vegetation density varies vertically or horizontally in

space. Lidar data also provides density data at a finer resolution than available for density-related metrics from the AVI and satellite layers. However, the tree species data from the AVI and satellite layers were strong predictors of most bird species, with AVI variables included in the top model (composite or otherwise) for 59 % of species and satellite variables included in the top model for 54 % of species. Habitat predictors from AVI and satellite layers were generally consistent with the ecology of individual species, e.g. birds that are associated with coniferous forests being more abundant as the proportion of different conifer species increased at a given spatial scale).

The top AVI, satellite, lidar, and composite models appeared to have adequate goodness-of-fit for predicting most species of birds in these analyses, based on diagnostics of Dunn-Smyth residuals. A few species were clearly overpredicted (e.g. Cedar Waxwing, Palm Warbler, Swamp Sparrow), and these species also had poor goodness-of-fit statistics (residuals overdispersed relative to a Poisson distribution, heteroscedastic relative to fitted values, and non-normally distributed within Q-Q plots). Basing predicted abundance on the means of the top AVI, satellite, and lidar models resulted in less overprediction than the composite model, but overpredicted abundance was still sever for these species. The mixture models in this study generally predict larger numbers of birds than were observed, since N -mixture models assume and account those birds that are present but fail to be detected during visits; however, dozens of Cedar Waxwing, Palm Warbler, and Swamp Sparrow were predicted at 1 to many stations within the Kirby grid. Models might be improved by accounting for nonlinear functions of habitat features since linear functions of some rare habitat features may result in extreme overpredictions of species that happen to co-occur with rare habitat features at stations. In the case of Cedar Waxwings, however, the actual site variables may not be important since very large numbers were predicted at stations even by a null abundance model.

While a composite model generally predicted abundance of most bird species better than models based on a single data source, averaging predictions from top models based on a single data source identified the same stations having the highest abundance of a species, for most species. Where there was less agreement between predictions based on averaging different data sources and predictions from the top composite model, this lack of agreement was observed more for common, widespread species on the Kirby grid like White-throated Sparrow and Yellow-rumped Warbler.

Storyline:

Boreal forest bird communities are difficult to monitor effectively because much of their habitat is not easily accessible, especially since multiple visits to each survey point are necessary to accurately quantify bird abundance or occupancy as well as habitat features influencing abundance or occupancy. However, quantification of bird and habitat data in remote areas can be achieved efficiently for large numbers of sites by a combination of 1) remote sensing with drones or planes to collect fine-scale habitat data, and 2) use of programmable acoustic recorders or autonomous recording units to collect bird data over multiple recordings in place of human visits. Newer analysis techniques like N -mixture or occupancy models are then well-suited for estimating true abundance or occupancy of bird species at sites from multiple recorded visits while accounting for detection probability of each species on different visits due to weather, time of season and day, and environmental noise.

Constraints, limitations, things to be aware of:

Unless certain conditions are met (distances to individual birds in the recordings are known or can be estimated, either from noise levels, triangulation by closely-spaced ARUs, or simultaneous point count data collected by human observers with distance-sampling methods), point count data collected by ARUs can only provide measures of relative abundance, not densities of birds. The point counts in the Kirby grid are spaced 600 m apart, so cannot be used to triangulate bird locations and distances from ARUs. There are also no corresponding human observations of birds at the ARUs to use for estimating distances to birds. Forest bird communities are difficult to monitor effectively because much of their habitat is not easily accessible, especially since multiple visits to each survey point are necessary to accurately quantify bird abundance or occupancy as well as habitat features influencing abundance or occupancy. Finally, counts of birds within ARU recordings are reliant on detection of bird sounds, so quietly or infrequently vocalizing bird species are less likely to be detected, and birds that are seen rather than heard will not be detected within recordings.

Eighty-four ARU point count stations and 3-4 recordings per ARU are currently available for analysis. This sample size will probably be insufficient for rarer species of interest such as owls, and some species of interest (e.g. Canada Warbler) have not been detected in the recordings transcribed so far.

Literature Cited:

Alberta Biodiversity Monitoring Institute. ABMI Wall-to-wall Human Footprint Map 2017 Version 1, 2019. [online] URL: <http://www.abmi.ca>. Alberta Biodiversity Monitoring Institute, Alberta, Canada.

Anderson, D.R. 2001. The need to get the basics right in wildlife field studies. *Wildlife Society Bulletin* 29:1294-1297.

Ball, J. R., P. Sólymos, F. K. A. Schmiegelow, S. Haché, J. Schieck, and E. M. Bayne. 2016. Regional habitat needs of a nationally listed species, Canada Warbler *Cardellina canadensis*, in Alberta, Canada. *Avian Conservation and Ecology* 11(2):10.

Barton, K., and M. K. Barton. 2019. Package ‘MuMIn’. R package version, 1(6).

Bayne, E. M., S. Haché, and K. A. Hobson. 2010. Comparing the predictive capability of forest songbird habitat models based on remotely sensed versus ground-based vegetation information. *Canadian Journal of Forest Research* 40: 65-71. Doi:10.1139/X09-170

Beaudoin, A., P. Y. Bernier, L. Guindon, P. Villemaire, X. J. Guo, G. Stinson, T. Bergeron, S. Magnussen, and R. J. Hall. 2013. Mapping attributes of Canada’s forests at moderate resolution through kNN and MODIS imagery. *Canadian Journal of Forest Research* 44: 521–532.

Boehlmann, N.T., G.P. Asner, P.J. Hart, and R.E. Martin. 2007. Multi-trophic invasion resistance in Hawaii: bioacoustics, field surveys, and airborne remote sensing. *Ecological Applications* 17:2137-2144.

Bourque, J., and A. Desrochers. 2006. Spatial aggregation of forest songbird territories and possible implications for area sensitivity. *Avian Conservation and Ecology* 1, no. 2.

Bowman, J. 2003. Is dispersal distance of birds proportional to territory size? Canadian Journal of Zoology 81:195-202.

Broughton, R.K., S.A. Hinsley, P.E. Bellamy, R.A. Hill, and P. Rothery. 2006. Marsh Tit *Poecile palustris* territories in a British broad-leaved wood. Ibis 148:744–752.

Buckland, S. T., D. R. Anderson, K. P. Burnham, and J. L. Laake (Editors) (2005). Distance Sampling. John Wiley & Sons, Ltd.

Chandler, C.R., E.D. Ketterson, V. Nolan Jr, and C. Ziegenfus. 1994. Effects of testosterone on spatial activity in free-ranging male dark-eyed juncos, *Junco hyemalis*. Animal Behaviour 47:1445-1455.

Chandler, R. and J. Hepinstall-Cymerman. 2016. Estimating the spatial scales of landscape effects on abundance. Landscape Ecology 31:1383-1394.

Clawges, R., K. Vierling, L. Vierling, and E. Rowell. 2008. The use of airborne lidar to assess avian species diversity, density, and occurrence in a pine/aspen forest. Remote Sensing of Environment 112:2064-2073.

Eldegard, K., J.W. Dirksen, H.O. Ørka, R. Halvorsen, E. Næsset, T. Gobakken, and M. Ohlson. 2014. Modelling bird richness and bird species presence in a boreal forest reserve using airborne laser-scanning and aerial images. Bird Study 61:204-219.

Evans et al. 2000. Swainson's Thrush (*Catharus ustulatus*). In A. Poole and F. Gill, eds. The Birds of North America, No. 540. The Birds of North America, Inc., Philadelphia, PA.

Farnsworth, G.L., K.H. Pollock, J.D. Nichols, T.R. Simons, J.E. Hines, and J.R. Sauer. 2002. A removal model for estimating detection probabilities from point-count surveys. The Auk 119: 414-425.

Fiske, I., and R. Chandler. 2011. Unmarked: an R package for fitting hierarchical models of wildlife occurrence and abundance. Journal of Statistical Software 43: 1-23.

Garabedian, J.E., R.J. McGaughey, S.E. Reutebuch, B.R. Parresol, J.C. Kilgo, C.E. Moorman, and M.N. Peterson. 2014. Quantitative analysis of woodpecker habitat using high-resolution airborne LiDAR estimates of forest structure and composition. Remote Sensing of Environment 145: 68-80.

Goetz, S.J., D. Steinberg, M.G. Betts, R.T. Holmes, P.J. Doran, R. Dubayah, and M. Hofton. 2010. Lidar remote sensing variables predict breeding habitat of a Neotropical migrant bird. Ecology 91: 1569–1576.

Graf, R.F., L. Mathys, and K. Bollmann. 2009. Habitat assessment for forest dwelling species using LiDAR remote sensing: Capercaille in the Alps. Forest Ecology and Management 257:160-167.

Hijmans, R. J., and J. van Etten. 2012. raster: Geographic analysis and modeling with raster data. R package version 2.0-12. <http://CRAN.R-project.org/package=raster>.

Hill, R.A., and A.G. Thompson 2005. Mapping woodland species composition and structure using airborne spectral and LiDAR data. International Journal of Remote Sensing 26:3763-3779.

Hinsley, , S.A., R.A. Hill, D.L.A. Gaveau, and P.E. Bellamy. 2002. Quantifying woodland structure and habitat quality for birds using airborne laser scanning. Functional Ecology 16:851–857.

Kéry, M., J.A. Royle, and H. Schmid. 2005. Modeling avian abundance from replicated counts using binomial mixture models. Ecological Applications 15:1450-1461.

Knape, J., D. Arlt, F. Barraquand, Å. Berg, M. Chevalier, T. Pärt, A. Ruete, and M. Zmihorski. 2017. Goodness of fit checks for binomial N-mixture models. bioRxiv: 194340.

Lesak, A.A., V.C. Radeloff, T.J. Hawbaker, A.M. Pidgeon, T. Gobakken, and K. Contrucci. 2011. Modeling forest songbird species richness using LiDAR-derived measures of Remote Sensing of Environment 115:2823-2835.

Matthysen, E., D. Cimprich, and T.C. Grubb Jr. 1992. Is social organization in winter determined by ahort- or long-term benefits? A case study on migrant red-breasted nuthatches *Sitta canadensis*. Ornis Scandinavica 23:43-48

Morse, D. M. 1976. Variables affecting the density and territory size of breeding spruce-woods warblers. Ecology 57:290-301.

Muller, J., C. Moning, C. Baessler, M. Heurich, and R. Brandl. 2009. Using airborne laser scanning to model potential abundance and assemblages of forest passerines. Basic and Applied Ecology 10:671-681.

Muller, J., J. Stadler, and R. Brandl. 2010. Composition versus physiognomy of vegetation as predictors of bird assemblages:The role of lidar. Remote Sensing of Environment 114:490–495

Odum, E. P. and E. J. Kuenzler. 1955. Measurement of territory and home range size in birds. The Auk 72:128-137.

Pinheiro, J., D. Bates, S. DebRoy, D. Sarkar, S. Heisterkamp, B. Van Willigen, B., and R. Maintainer. 2017. Package ‘nlme’. Linear and nonlinear mixed effects models, version, 3-1.

Royle, J.A., J.D. Nichols, and M. Kéry. 2005. Modelling occurrence and abundance of species when detection is imperfect. Oikos 110: 353-359.

Seavy, N.E., J.H. Viers, and J.K. Wood. 2009. Riparian bird response to vegetation structure: a multiscale analysis using LiDAR measurements of canopy height. Ecological Applications 19:1848–1857.

Sólymos, P., L. Mahon, T. Fontaine, and E. M. Bayne. 2015. Predictive models for estimating the cumulative effects of human development on migratory landbirds in the oil sands areas of

Alberta. Technical Report, Joint Oil Sands Monitoring: Cause-Effects Assessment of Oil Sands Activity on Migratory Landbirds, Edmonton, AB, Canada.

Tattoni, C., F. Rizzolli, and P. Pedrini. 2012. Can LiDAR data improve bird habitat suitability models? *Ecological Modelling* 245:103– 110.

Toews, D.P.L., and D.E. Irwin 2008. Cryptic speciation in a Holarctic passerine revealed by genetic and bioacoustic analyses. *Molecular Ecology* 17:2691-2705.

Vieilledent, G., Merow, C., Guélat, J., Latimer, A.M., Kéry, M., Gelfand, A.E., Wilson, A.M., Mortier, F. and Silander Jr, J.A., 2015. Hierarchical Bayesian species distribution models with the hSDM R Package.

Vierling, K.T., C.E. Swift, A.T. Hudak, J.C. Vogeler, and L.A. Vierling. 2014. How much does the time lag between wildlife field-data collection and LiDAR-data acquisition matter for studies of animal distributions? A case study using bird communities. *Remote Sensing Letters* 5: 185-193.

Vogeler, J.C., A.T. Hudak, L.A. Vierling, and K.T. Vierling. 2013. Lidar-derived canopy architecture predicts brown creeper occupancy of two western coniferous forests. *Condor* 115:614–622

Wasserman, F.E. 1980. Territorial behavior in a pair of white-throated sparrows. *Wilson Bulletin* 92:74-87.

Wilsey, C.B., J.J. Lawler, and D.A. Cimprich. 2012. Performance of habitat suitability models for the endangered black-capped vireo built with remotely-sensed data. *Remote Sensing of Environment* 119:35-42.

Wortman-Wunder, E. 1997. Territory size in Lincoln's Sparrows (*Melospiza lincolni*). *The Southwestern Naturalist* 42: 446-453

Figure 2. Model coefficients for the best N-mixture model predicting abundance of Alder Flycatcher *Empidonax alnorum* from Alberta Vegetation Inventory (AVI) shapefile-based data at the 50-m scale (AIC= 172.04) (A), 150-m scale (AIC= 171.61) (C), and 500-m scale (AIC= 168.14) (E), along with predicted abundances of this species in the Kirby grid from these respective models (B,D,F).

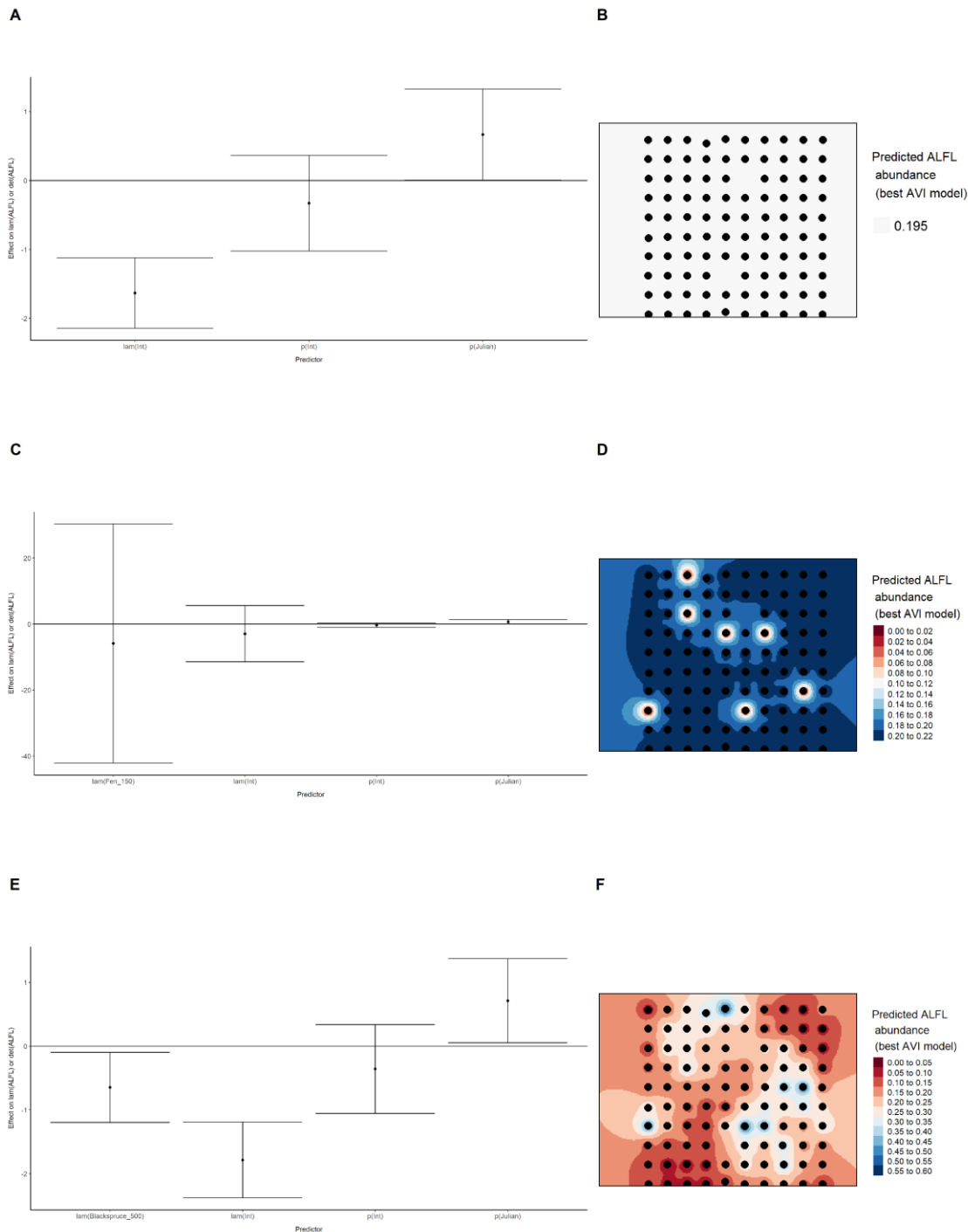


Figure 3. Model coefficients for the best N -mixture model predicting abundance of Alder Flycatcher *Empidonax alnorum* from satellite-based data at the 50-m scale (AIC= 160.34) (A), 150-m scale (AIC= 162.19) (C), and 500-m scale (AIC= 165.38) (E), along with predicted abundances of this species in the Kirby grid from these respective models (B,D,F).

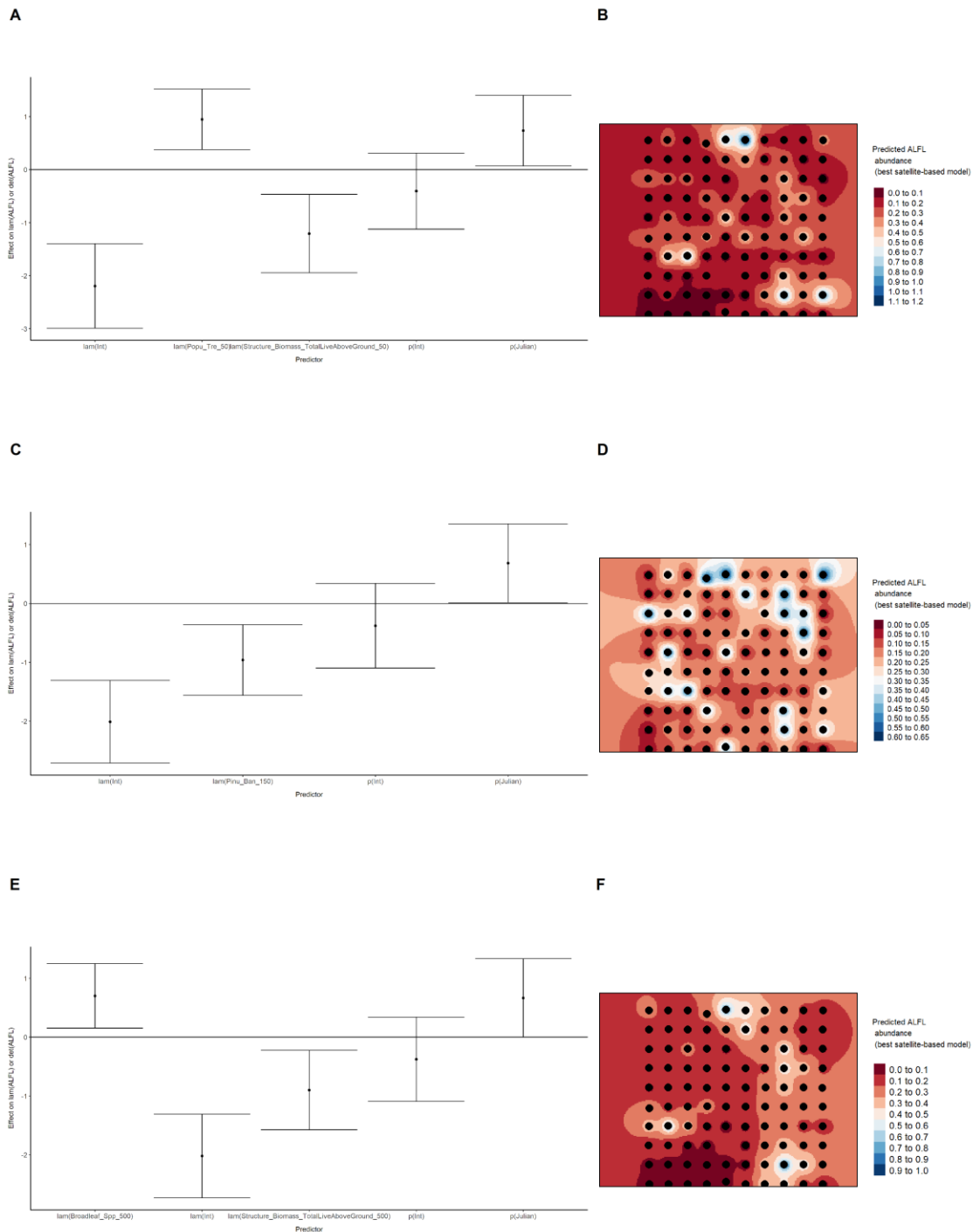


Figure 4. Model coefficients for the best N -mixture model predicting abundance of Alder Flycatcher *Empidonax alnorum* from LIDAR-based data at the 150-m scale (AIC= 145) (A), and 500-m scale (AIC= 152.18) (C), along with predicted abundances of this species in the Kirby grid from these respective models (B,D).

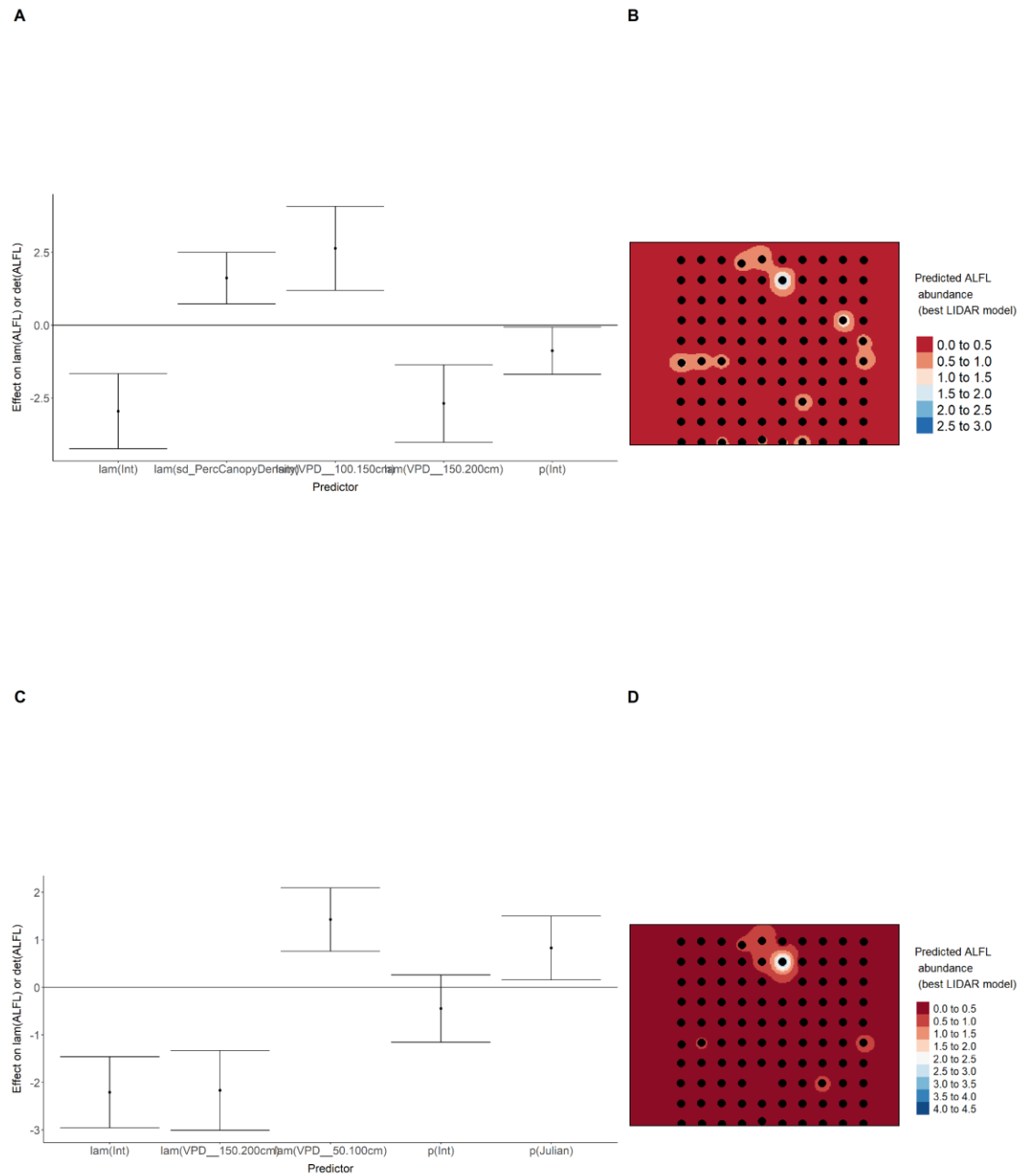


Figure 5. Model coefficients for the A) AVI-based (AIC= 168.14), C) satellite-based (AIC= 160.34), E) lidar-based (AIC= 145), and G) composite (AIC= 136.11) N -mixture models predicting abundance of Alder Flycatcher *Empidonax alnorum*, along with predicted abundances of this species in the Kirby grid from these respective models (B,D,F,H).

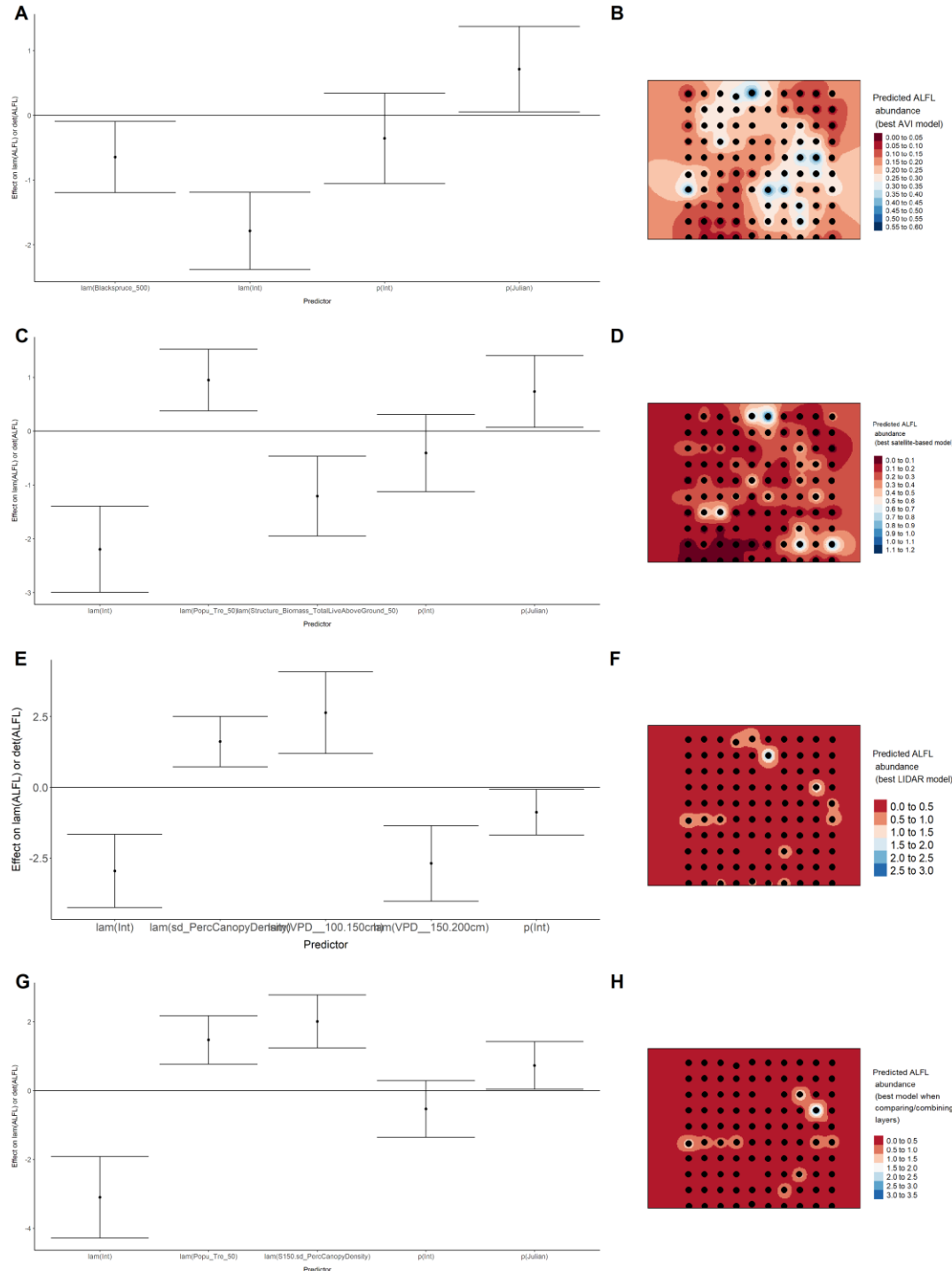


Figure 6. Model coefficients for the best N -mixture model predicting abundance of American Robin *Turdus migratorius* from Alberta Vegetation Inventory (AVI) shapefile-based data at the

50-m scale (AIC= 289.41) (A), 150-m scale (AIC= 291.6) (C), and 500-m scale (AIC= 284.87) (E), along with predicted abundances of this species in the Kirby grid from these respective models (B,D,F).

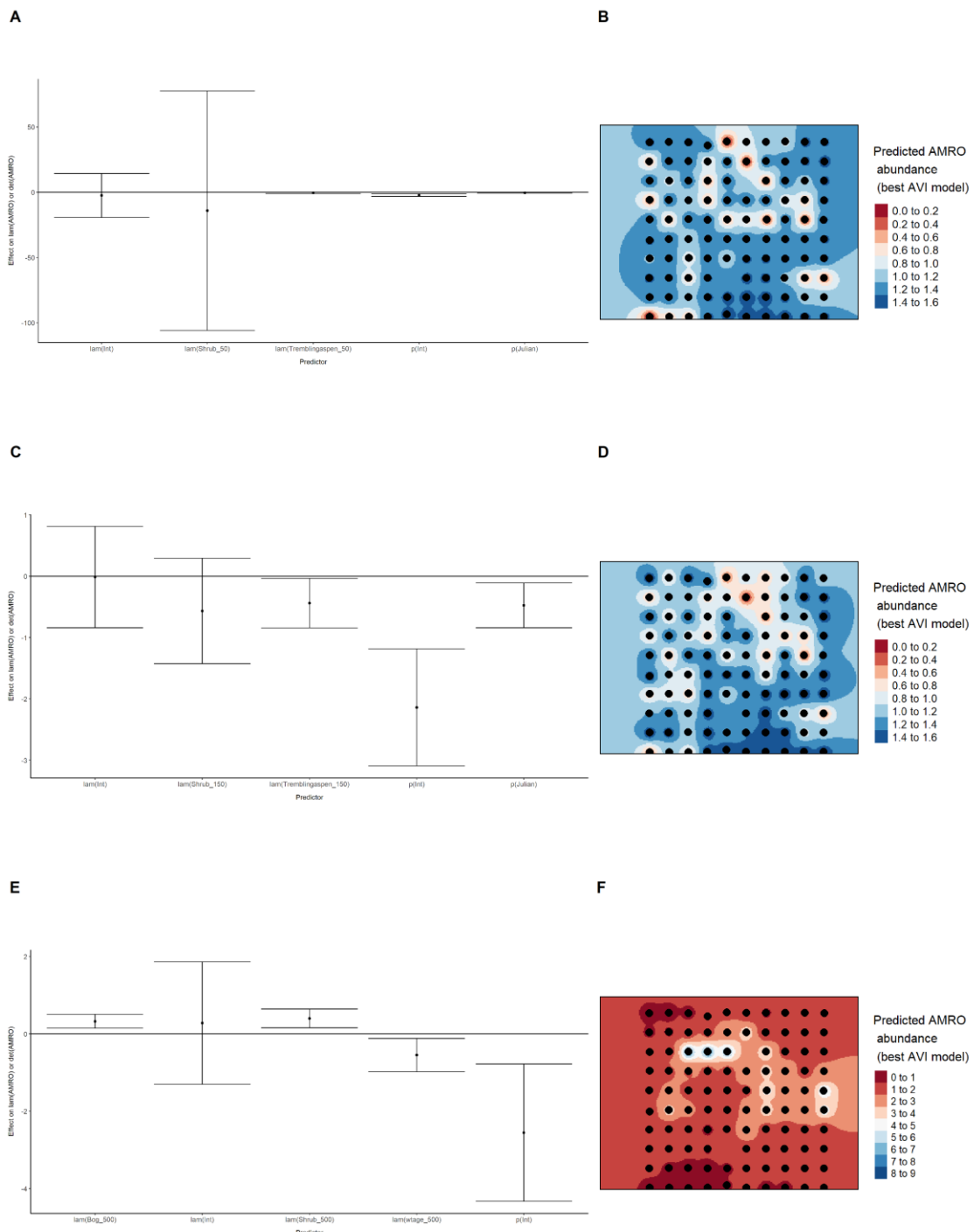


Figure 7. Model coefficients for the best N -mixture model predicting abundance of American Robin *Turdus migratorius* from satellite-based data at the 50-m scale (AIC= 291.12) (A), 150-m scale (AIC= 289.69) (C), and 500-m scale (AIC= 282.86) (E), along with predicted abundances of this species in the Kirby grid from these respective models (B,D,F).

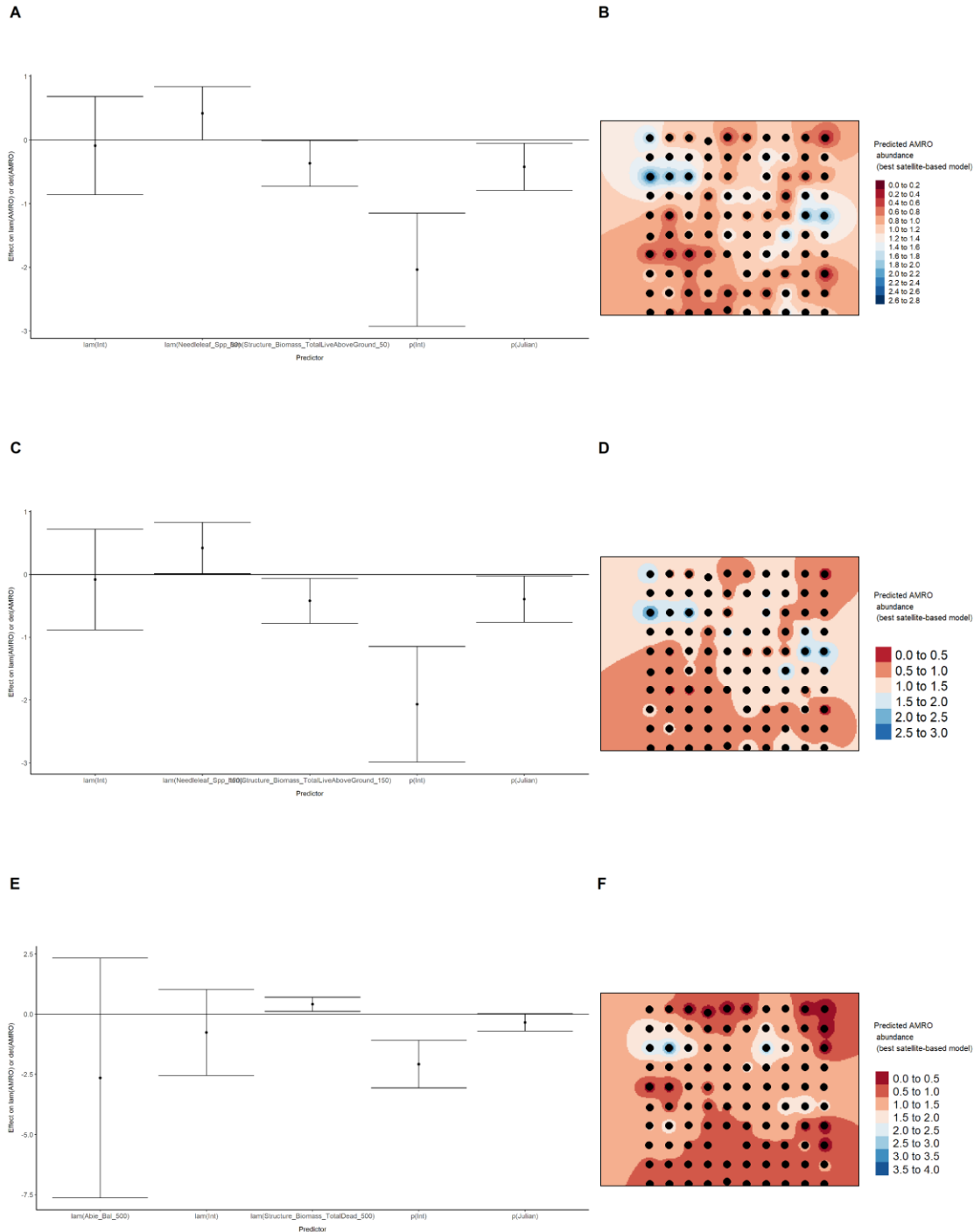


Figure 8. Model coefficients for the best N -mixture model predicting abundance of American Robin *Turdus migratorius* from LIDAR-based data at the 150-m scale (AIC= 285.99) (A), and 500-m scale (AIC= 286.04) (C), along with predicted abundances of this species in the Kirby grid from these respective models (B,D).

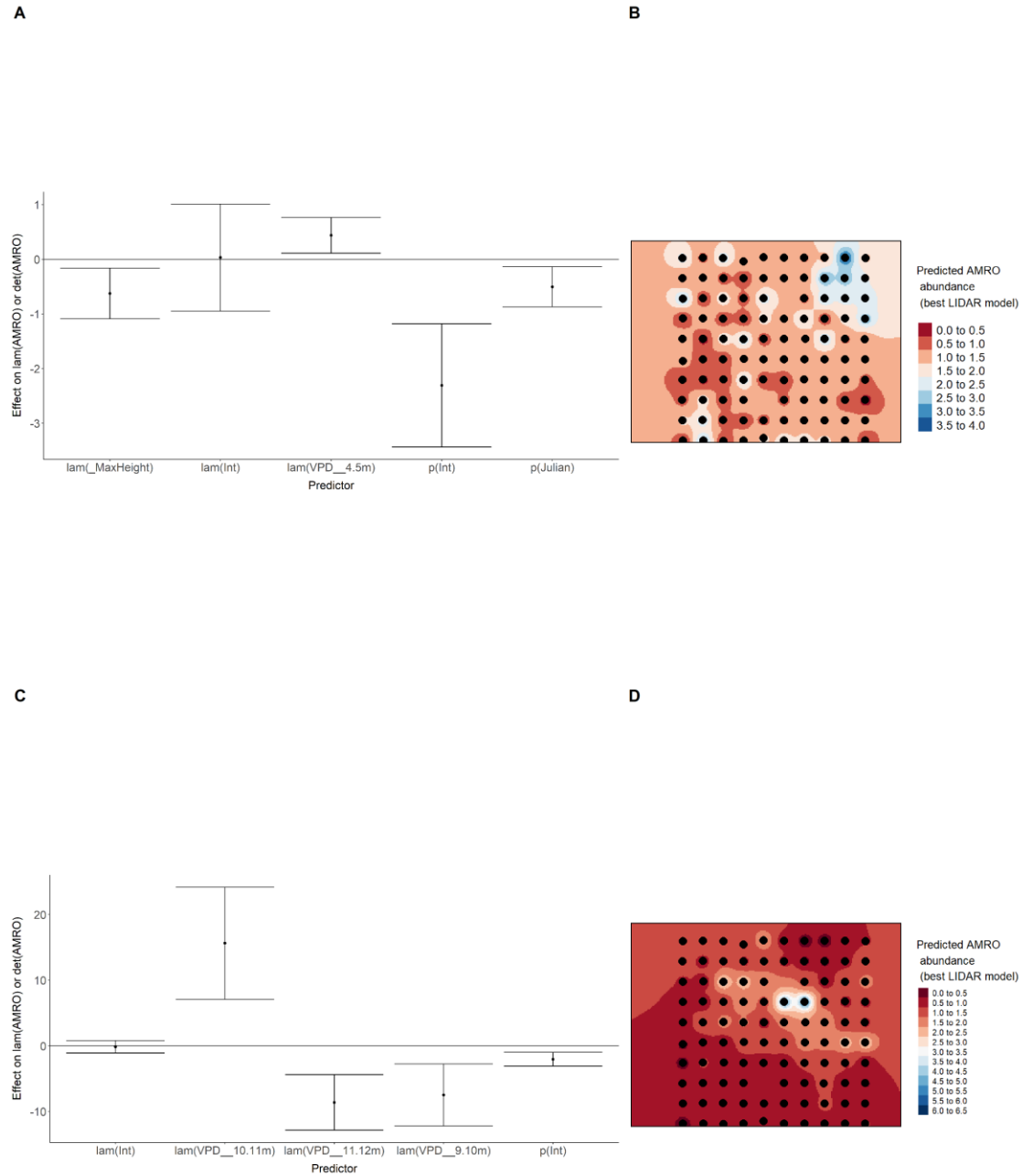


Figure 9. Model coefficients for the A) AVI-based (AIC= 284.87), C) satellite-based (AIC= 282.86), E) lidar-based (AIC= 285.99), and G) composite (AIC= 277.73) *N*-mixture models predicting abundance of American Robin *Turdus migratorius*, along with predicted abundances of this species in the Kirby grid from these respective models (B,D,F,H).

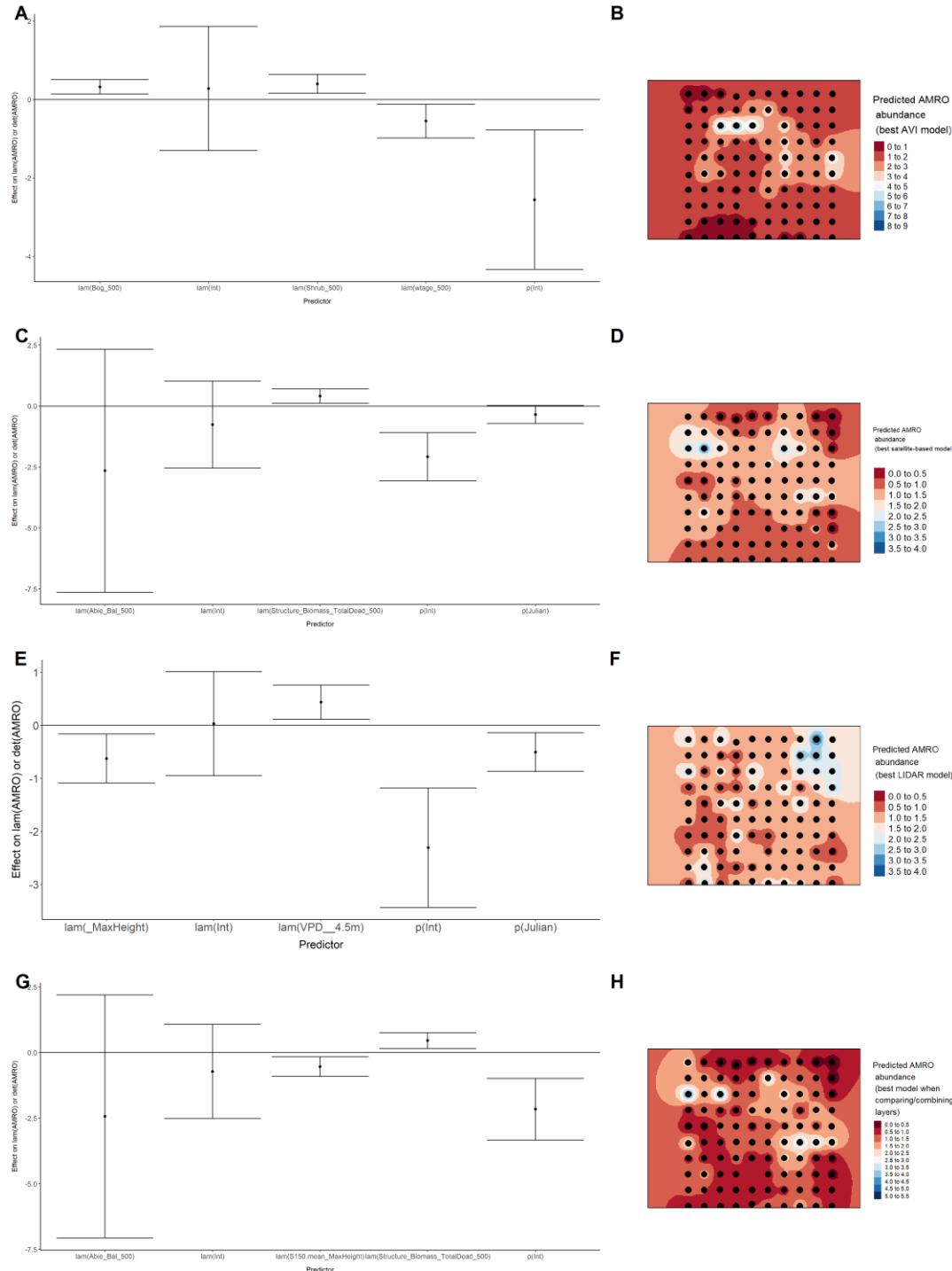
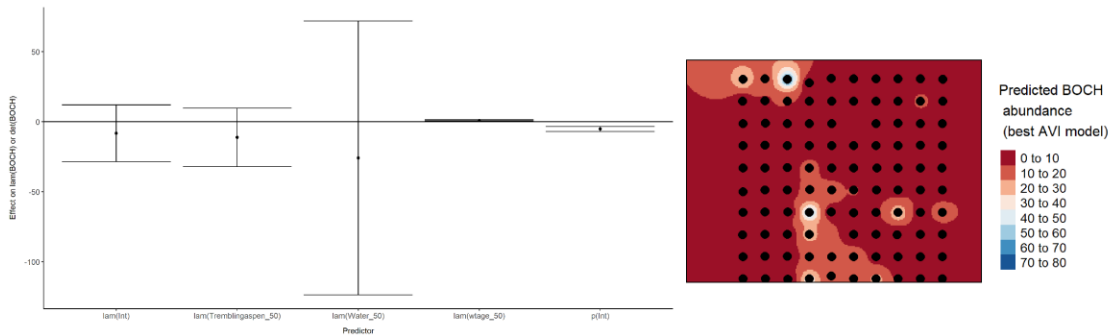


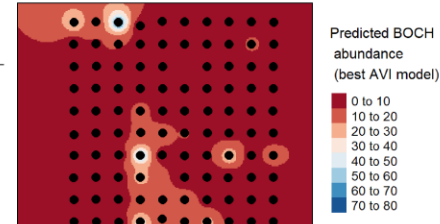
Figure 10. Model coefficients for the best *N*-mixture model predicting abundance of Boreal Chickadee *Poecile hudsonicus* from Alberta Vegetation Inventory (AVI) shapefile-based data at

the 50-m scale (AIC= 126.92) (A), 150-m scale (AIC= 129.92) (C), and 500-m scale (AIC= 135.31) (E), along with predicted abundances of this species in the Kirby grid from these respective models (B,D,F).

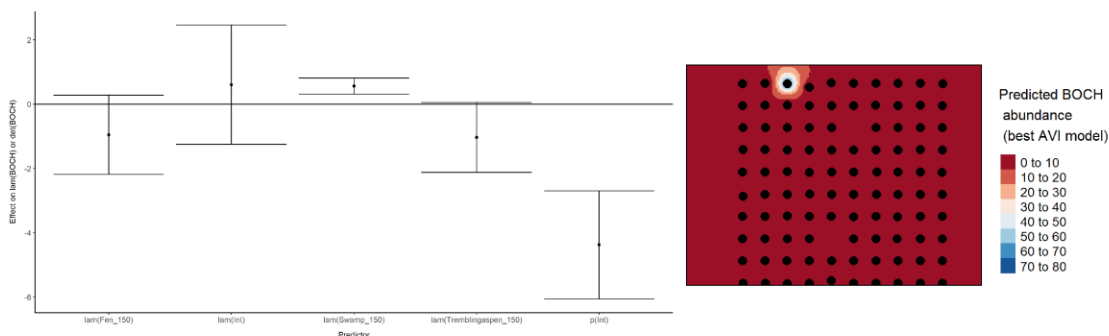
A



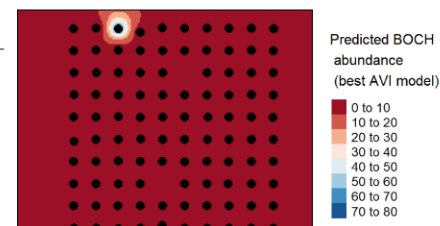
B



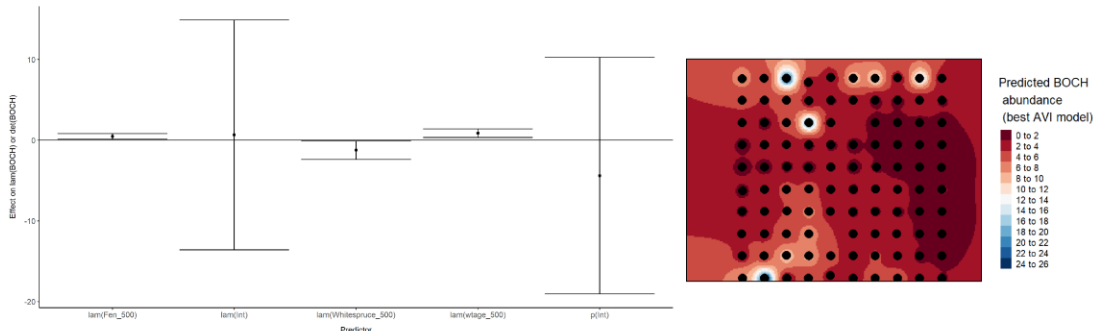
C



D



E



F

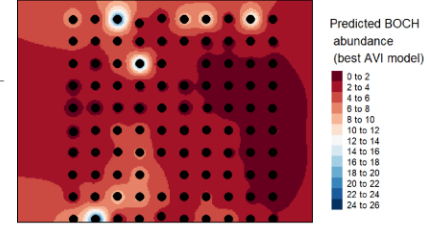


Figure 11. Model coefficients for the best N -mixture model predicting abundance of Boreal Chickadee *Poecile hudsonicus* from satellite-based data at the 50-m scale (AIC= 139.85) (A), 150-m scale (AIC= 141.04) (C), and 500-m scale (AIC= 135.83) (E), along with predicted abundances of this species in the Kirby grid from these respective models (B,D,F).

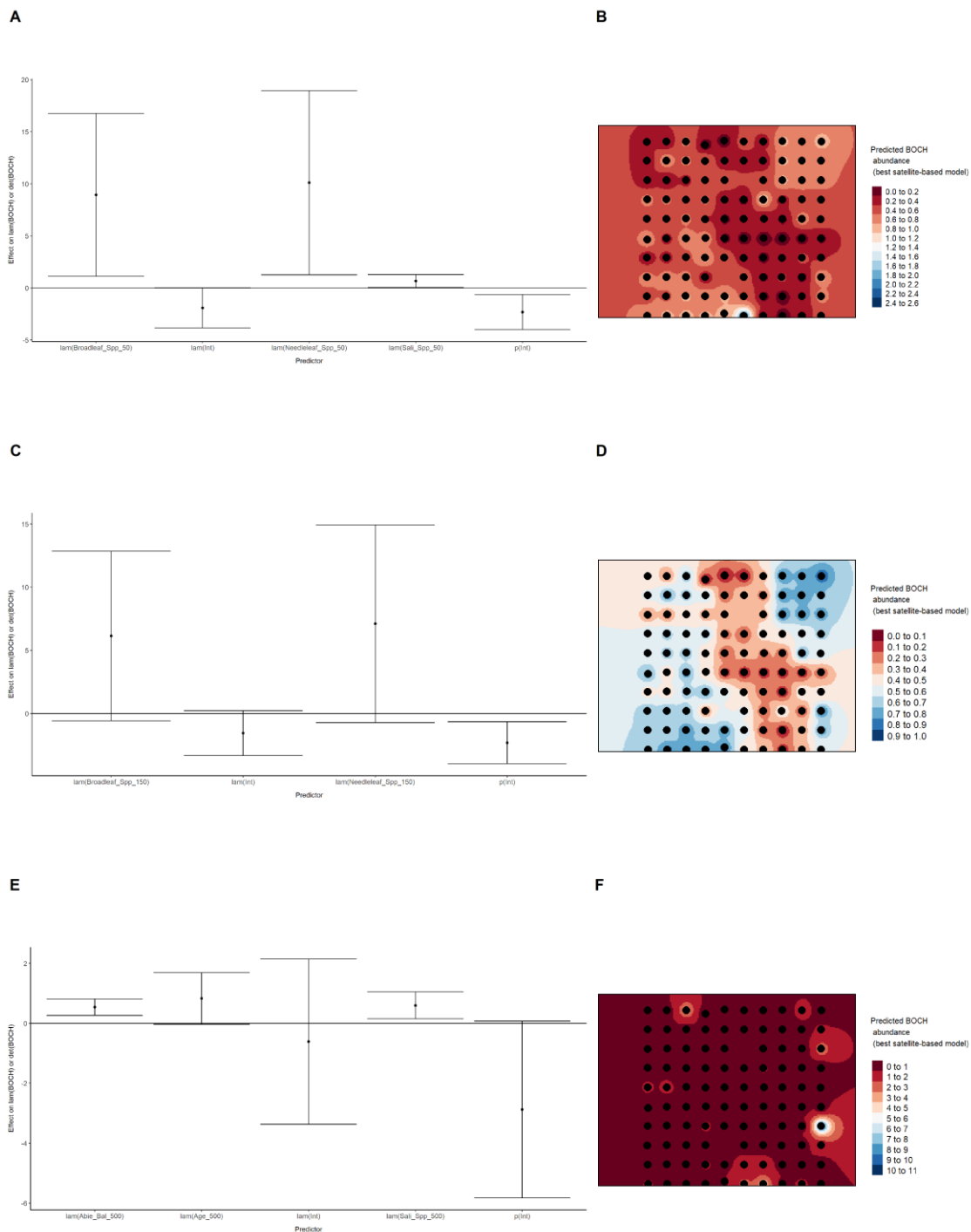


Figure 12. Model coefficients for the best N -mixture model predicting abundance of Boreal Chickadee *Poecile hudsonicus* from LIDAR-based data at the 150-m scale (AIC= 127.93) (A), and 500-m scale (AIC= 130.84) (C), along with predicted abundances of this species in the Kirby grid from these respective models (B,D).

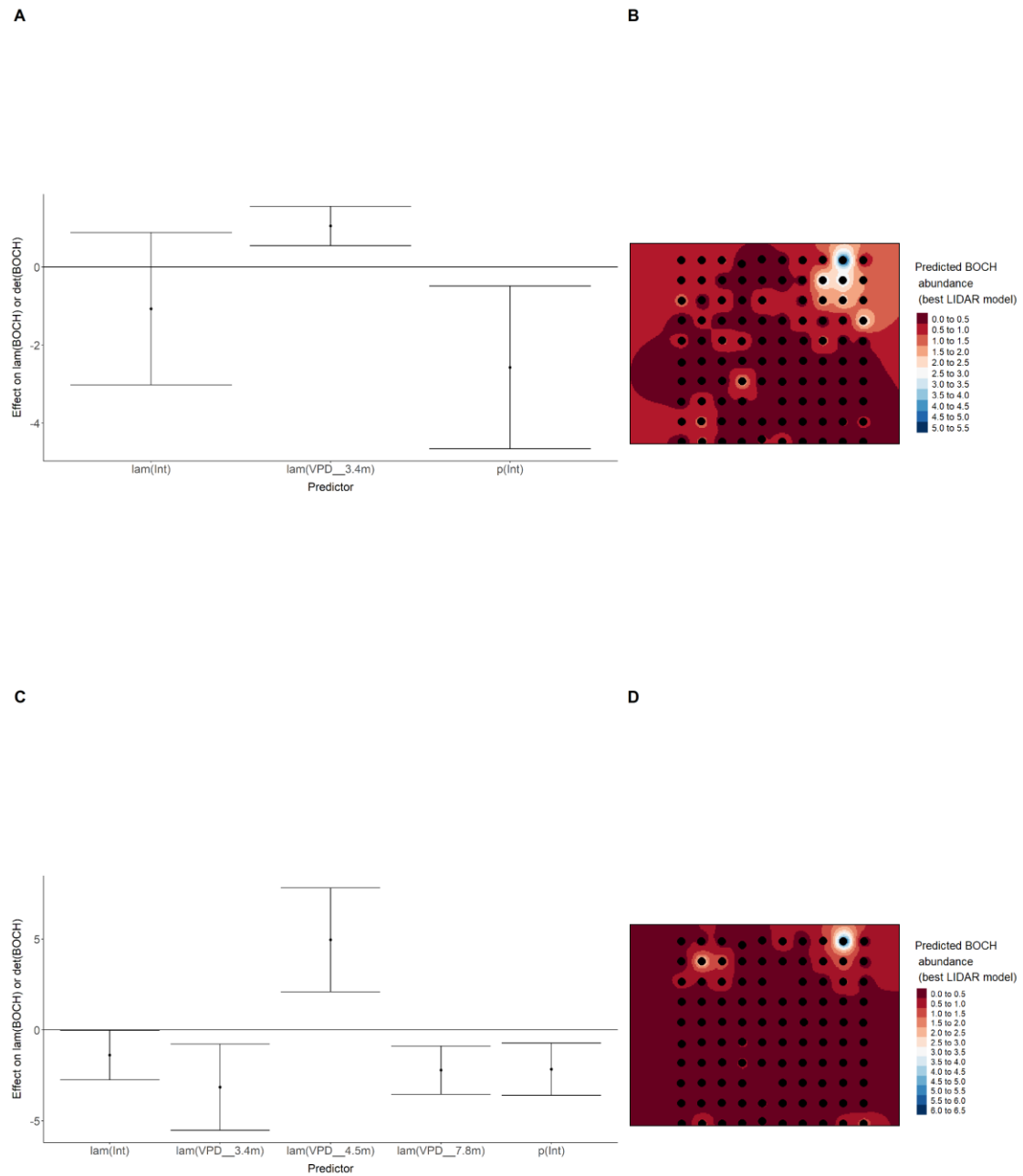


Figure 13. Model coefficients for the A) AVI-based (AIC= 126.92), C) satellite-based (AIC= 135.83), E) lidar-based (AIC= 127.93), and G) composite (AIC= 118.64) *N*-mixture models predicting abundance of Boreal Chickadee *Poecile hudsonicus*, along with predicted abundances of this species in the Kirby grid from these respective models (B,D,F,H).

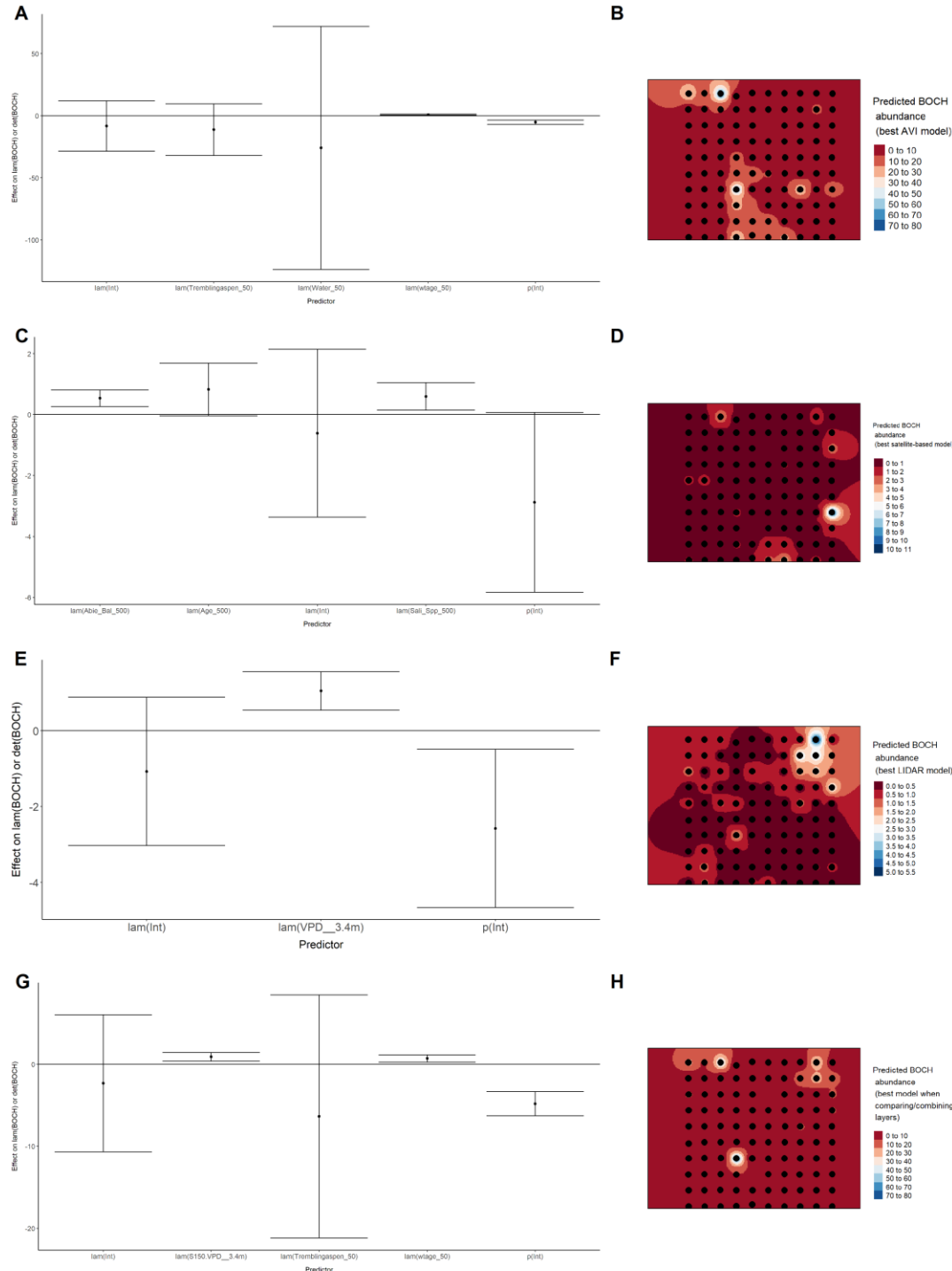
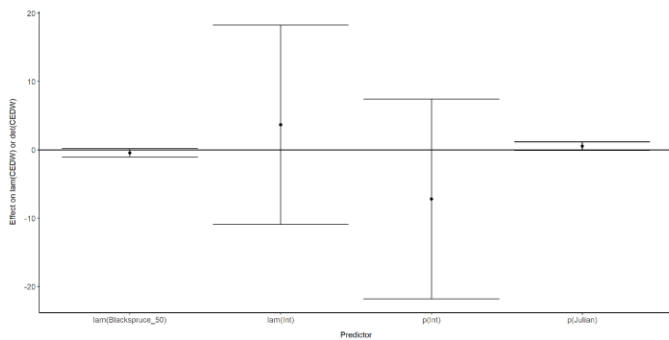


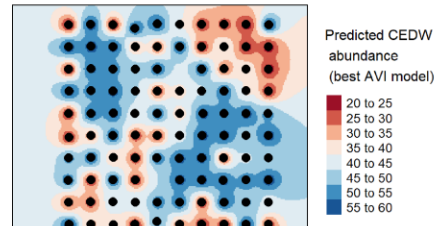
Figure 14. Model coefficients for the best *N*-mixture model predicting abundance of Cedar Waxwing *Bombycilla cedrorum* from Alberta Vegetation Inventory (AVI) shapefile-based data at

the 50-m scale ($AIC= 126.2$) (A), 150-m scale ($AIC= 118.63$) (C), and 500-m scale ($AIC= 123.4$) (E), along with predicted abundances of this species in the Kirby grid from these respective models (B,D,F).

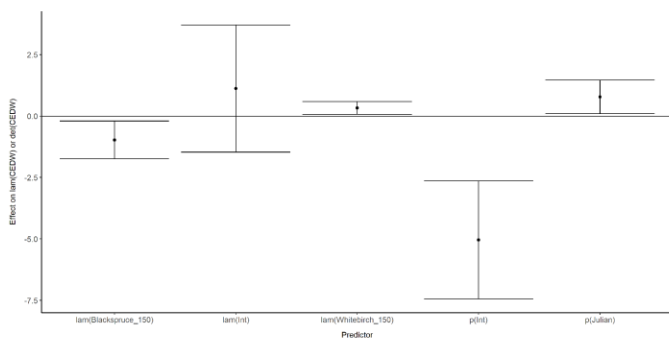
A



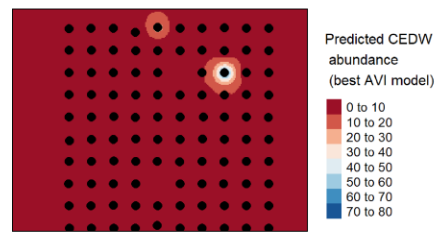
B



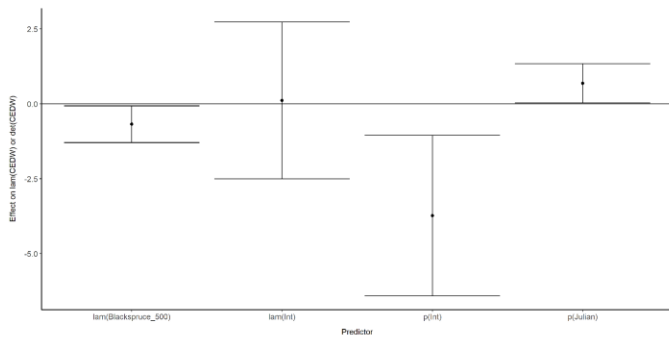
C



D



E



F

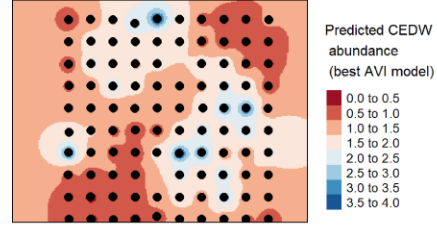


Figure 15. Model coefficients for the best N -mixture model predicting abundance of Cedar Waxwing *Bombycilla cedrorum* from satellite-based data at the 50-m scale (AIC= 126.43) (A), 150-m scale (AIC= 126.43) (C), and 500-m scale (AIC= 126.43) (E), along with predicted abundances of this species in the Kirby grid from these respective models (B,D,F).

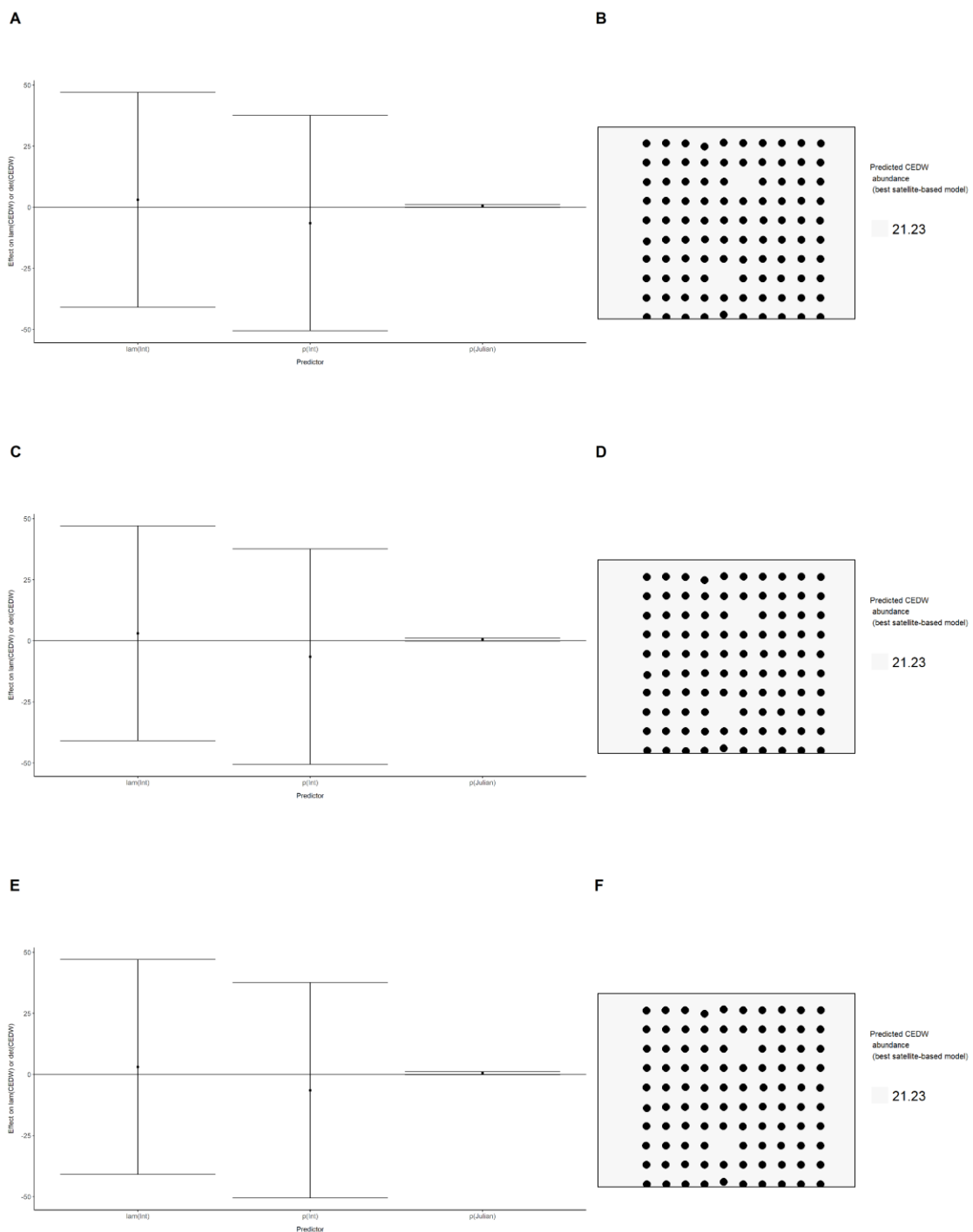


Figure 16. Model coefficients for the best N -mixture model predicting abundance of Cedar Waxwing *Bombycilla cedrorum* from LIDAR-based data at the 150-m scale (AIC= 126.29) (A), and 500-m scale (AIC= 123.71) (C), along with predicted abundances of this species in the Kirby grid from these respective models (B,D).

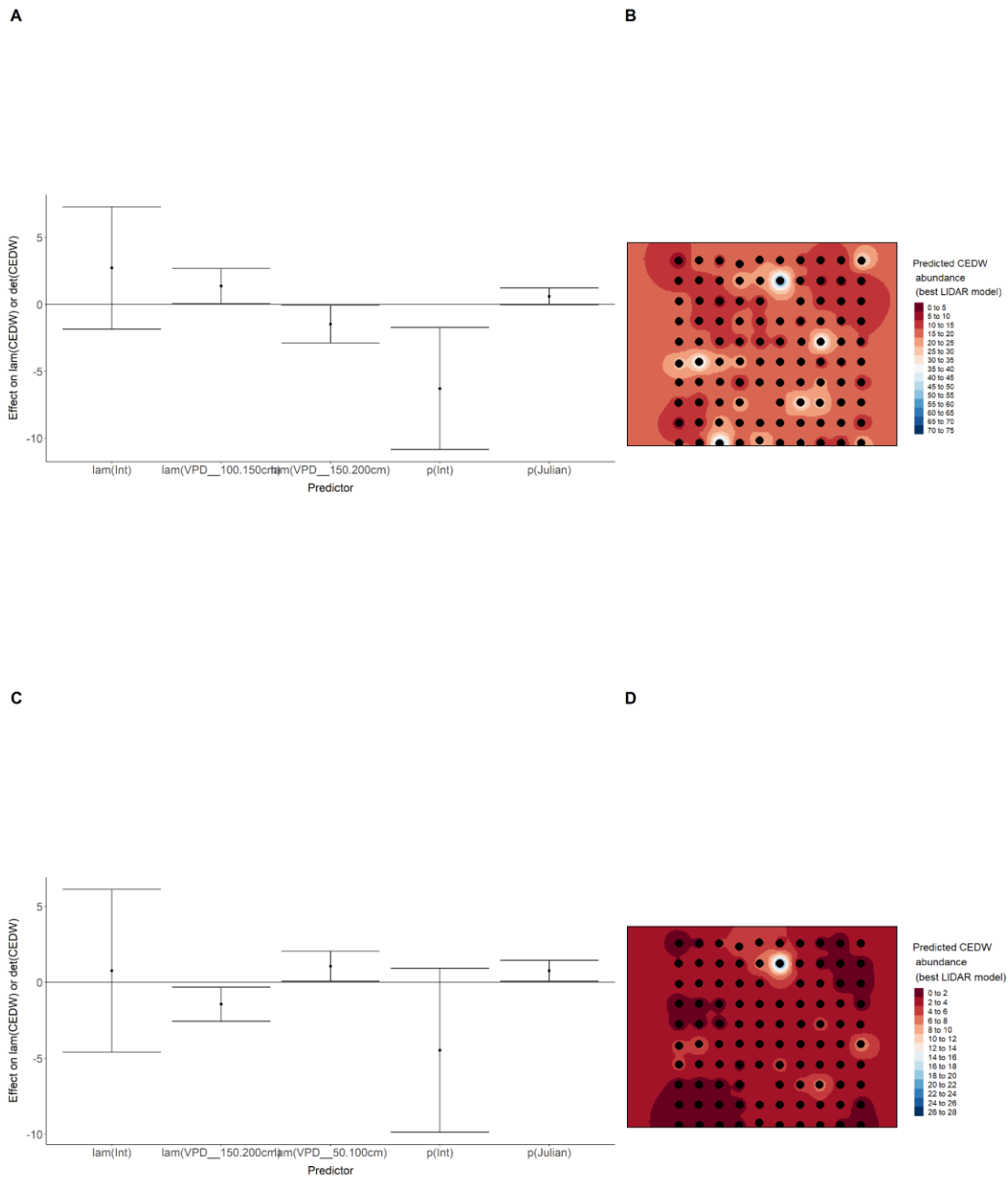


Figure 17. Model coefficients for the A) AVI-based (AIC= 118.63), C) satellite-based (AIC= 126.43), E) lidar-based (AIC= 123.71), and G) composite (AIC= 118.63) N-mixture models predicting abundance of Cedar Waxwing *Bombycilla cedrorum*, along with predicted abundances of this species in the Kirby grid from these respective models (B,D,F,H).

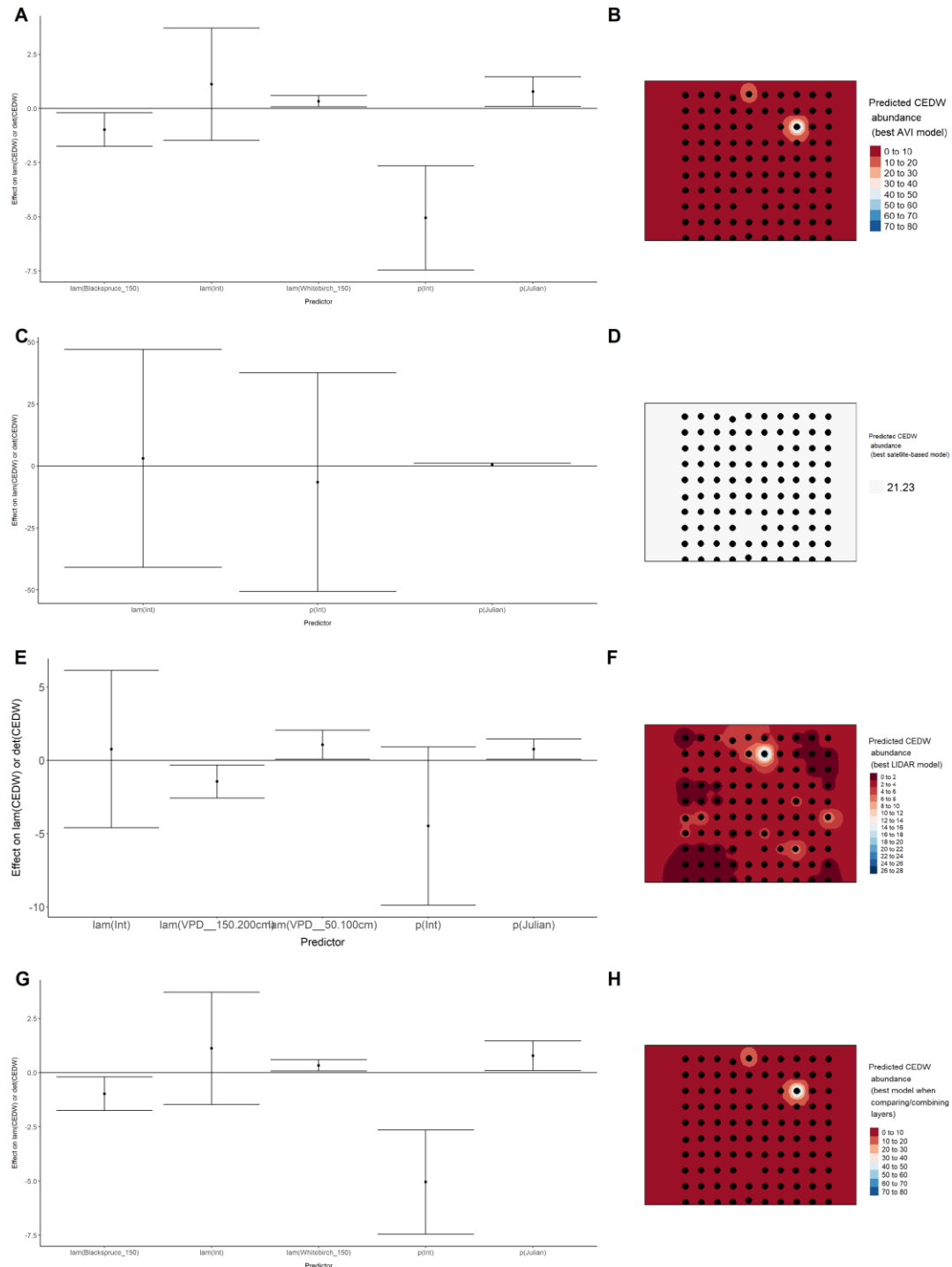
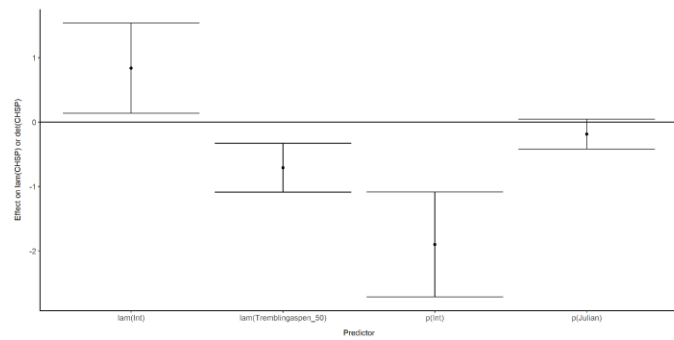


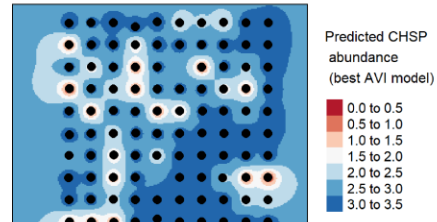
Figure 18. Model coefficients for the best N-mixture model predicting abundance of Chipping Sparrow *Spizella passerina* from Alberta Vegetation Inventory (AVI) shapefile-based data at the

50-m scale (AIC= 566.71) (A), 150-m scale (AIC= 567.49) (C), and 500-m scale (AIC= 576.64) (E), along with predicted abundances of this species in the Kirby grid from these respective models (B,D,F).

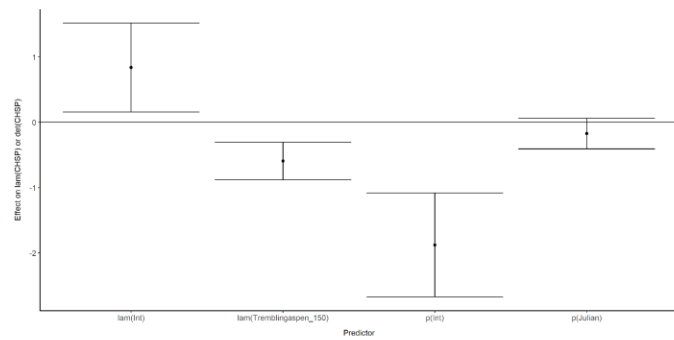
A



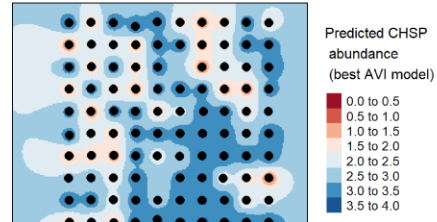
B



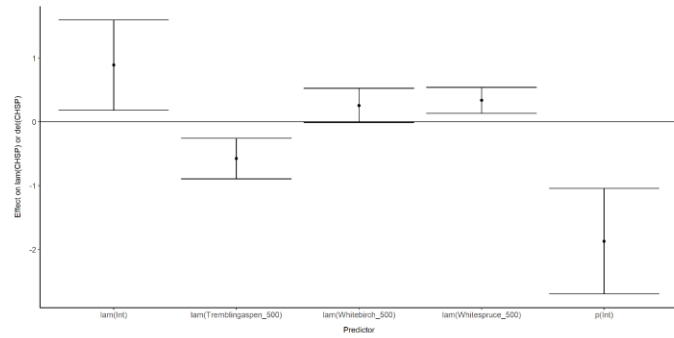
C



D



E



F

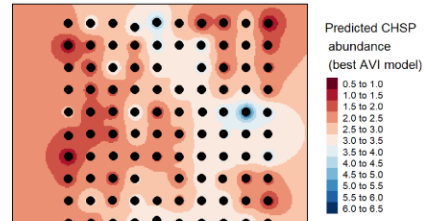


Figure 19. Model coefficients for the best N -mixture model predicting abundance of Chipping Sparrow *Spizella passerina* from satellite-based data at the 50-m scale (AIC= 578.98) (A), 150-m scale (AIC= 576.92) (C), and 500-m scale (AIC= 573) (E), along with predicted abundances of this species in the Kirby grid from these respective models (B,D,F).

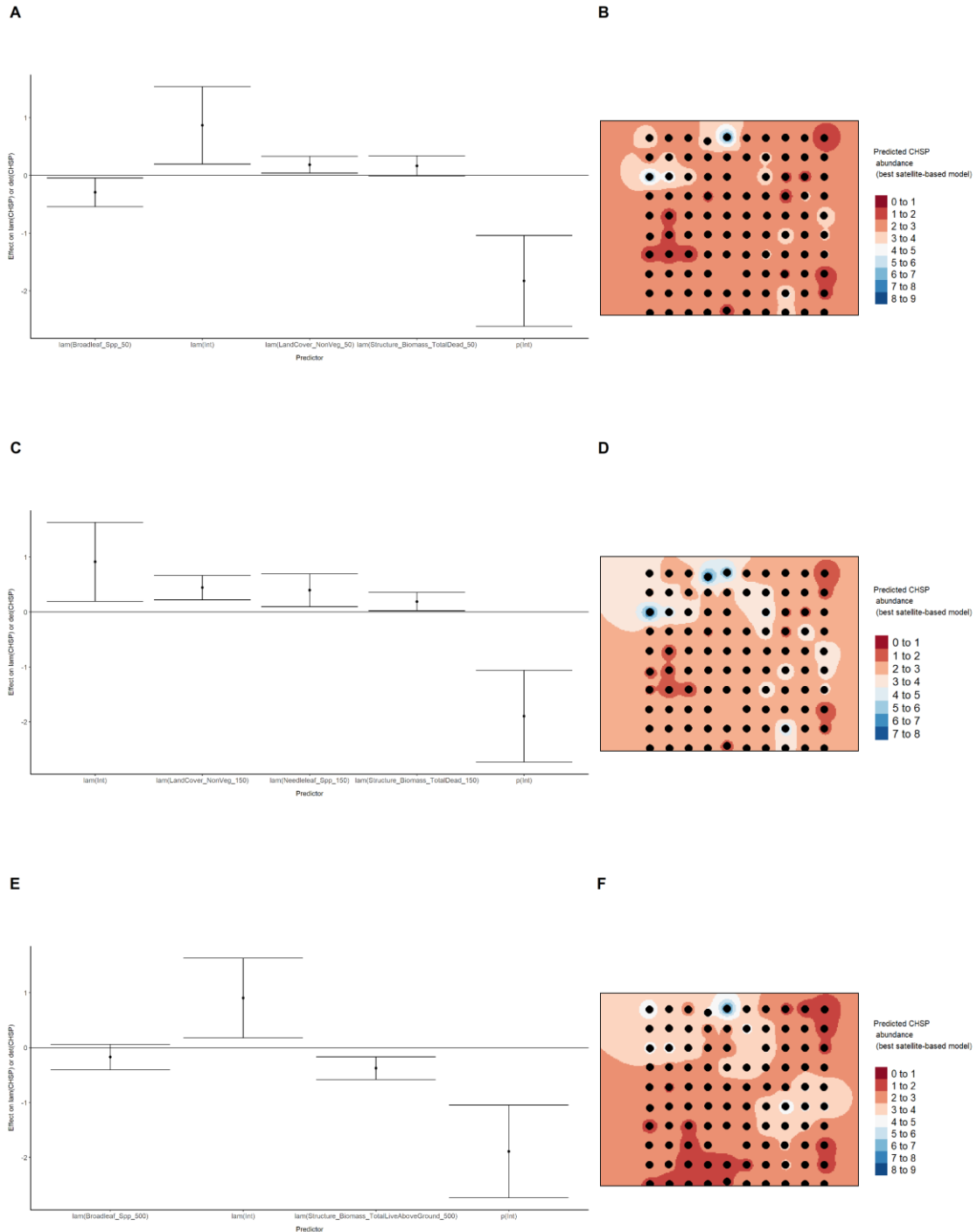


Figure 20. Model coefficients for the best N -mixture model predicting abundance of Chipping Sparrow *Spizella passerina* from LIDAR-based data at the 150-m scale (AIC= 550.27) (A), and 500-m scale (AIC= 574.45) (C), along with predicted abundances of this species in the Kirby grid from these respective models (B,D).

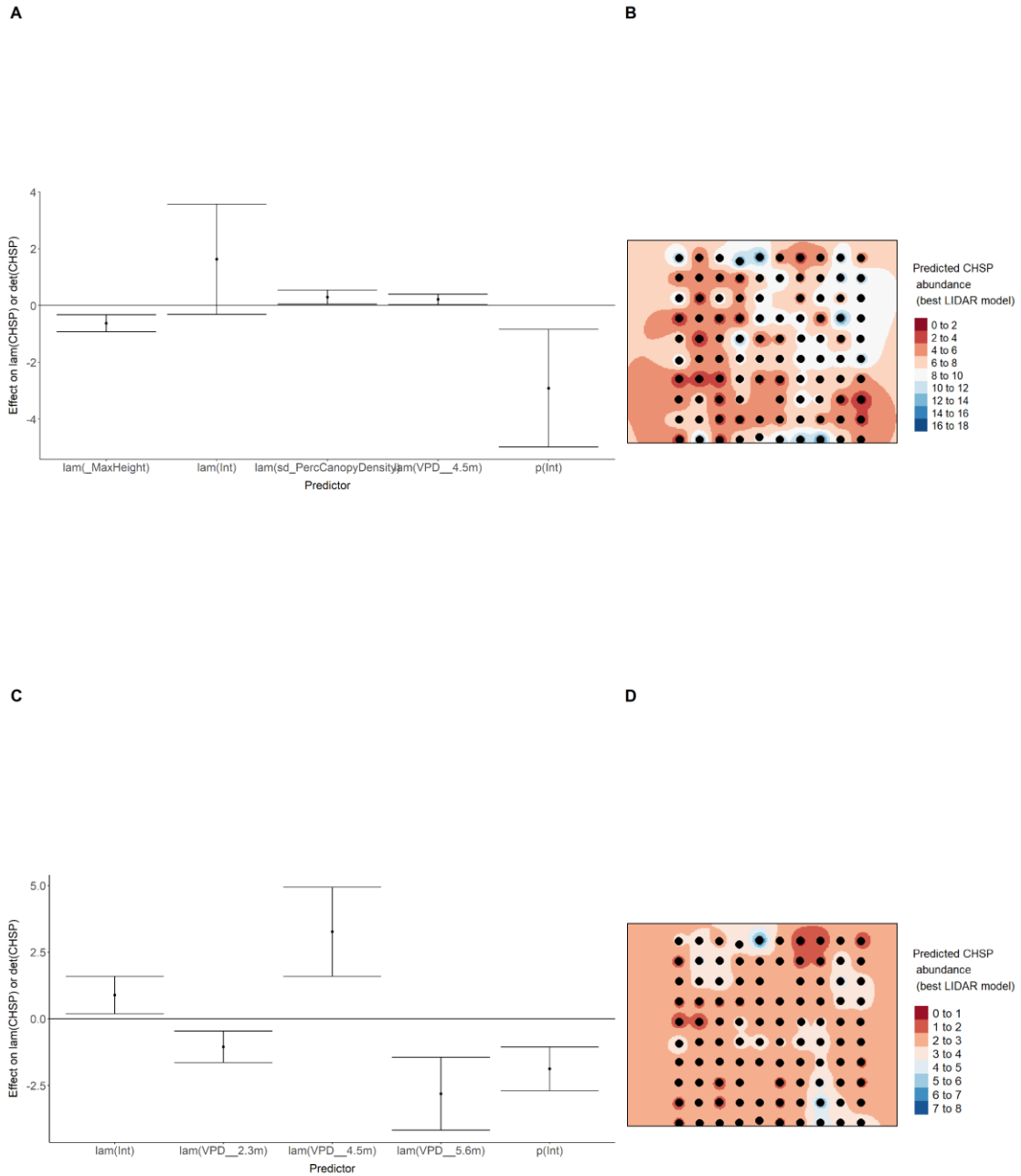


Figure 21. Model coefficients for the A) AVI-based (AIC= 566.71), C) satellite-based (AIC= 573), E) lidar-based (AIC= 550.27), and G) composite (AIC= 550.23) *N*-mixture models predicting abundance of Chipping Sparrow *Spizella passerina*, along with predicted abundances of this species in the Kirby grid from these respective models (B,D,F,H).

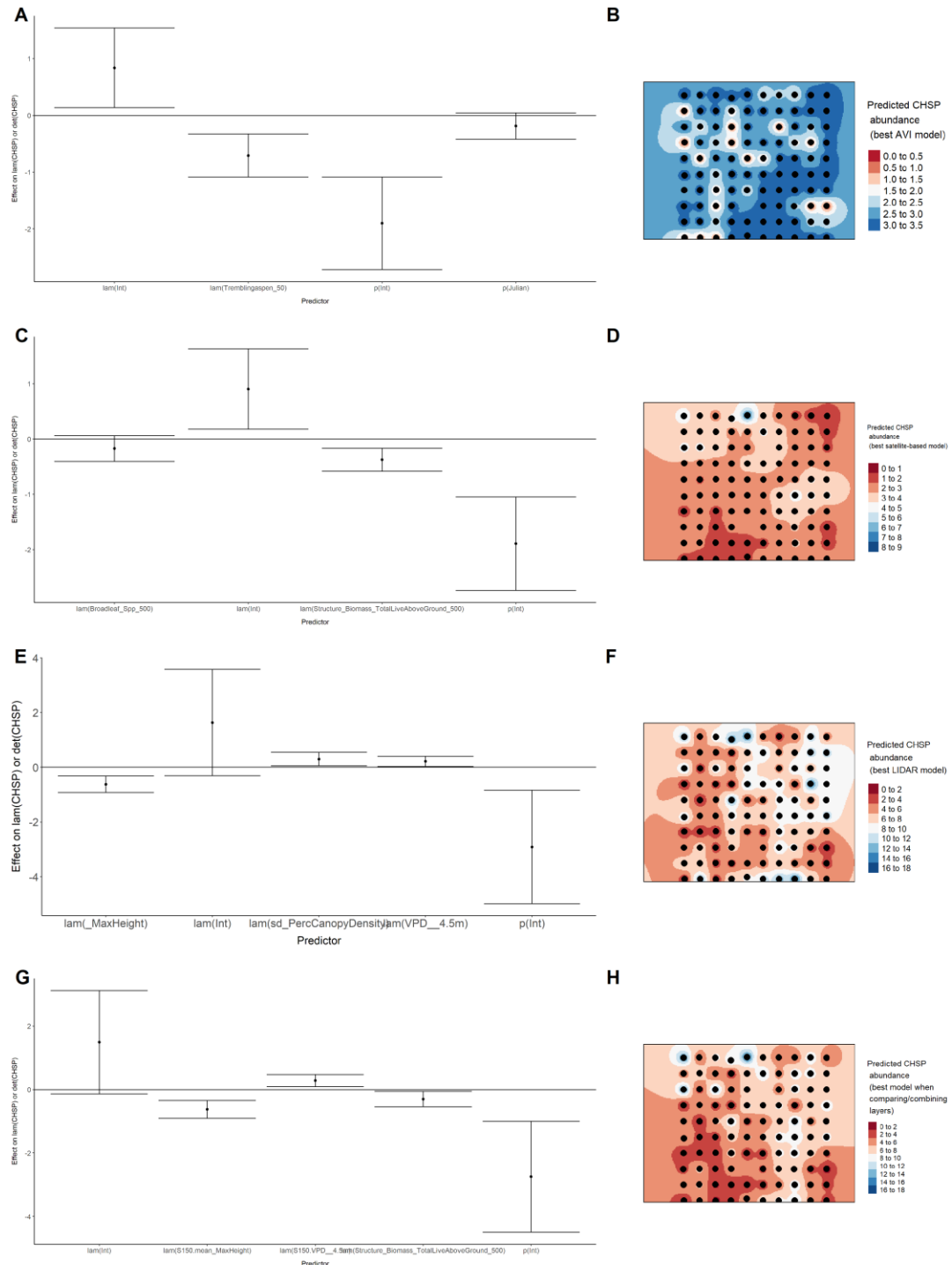
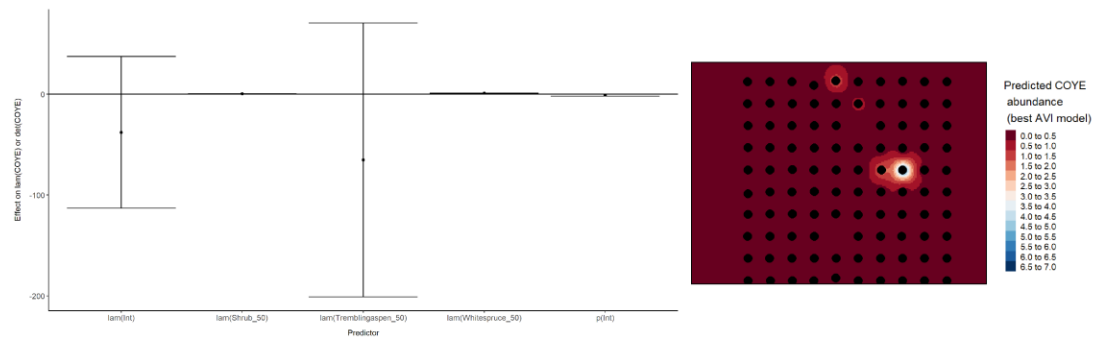


Figure 22. Model coefficients for the best *N*-mixture model predicting abundance of Common Yellowthroat *Geothlypis trichas* from Alberta Vegetation Inventory (AVI) shapefile-based data at

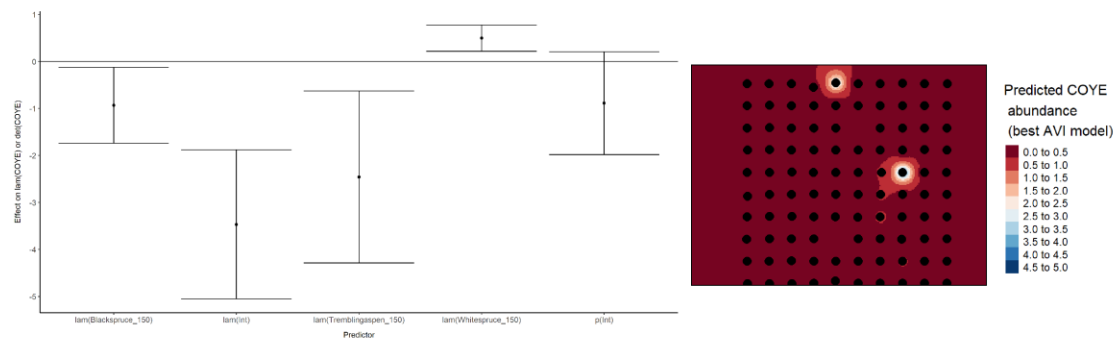
the 50-m scale (AIC= 109.5) (A), 150-m scale (AIC= 111) (C), and 500-m scale (AIC= 118.97) (E), along with predicted abundances of this species in the Kirby grid from these respective models (B,D,F).

A



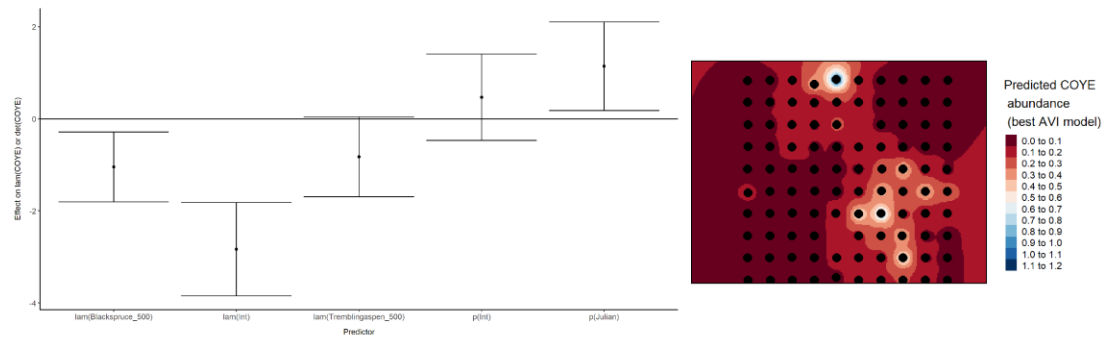
B

C



D

E



F

Figure 23. Model coefficients for the best N -mixture model predicting abundance of Common Yellowthroat *Geothlypis trichas* from satellite-based data at the 50-m scale (AIC= 124.84) (A), 150-m scale (AIC= 123.88) (C), and 500-m scale (AIC= 120) (E), along with predicted abundances of this species in the Kirby grid from these respective models (B,D,F).

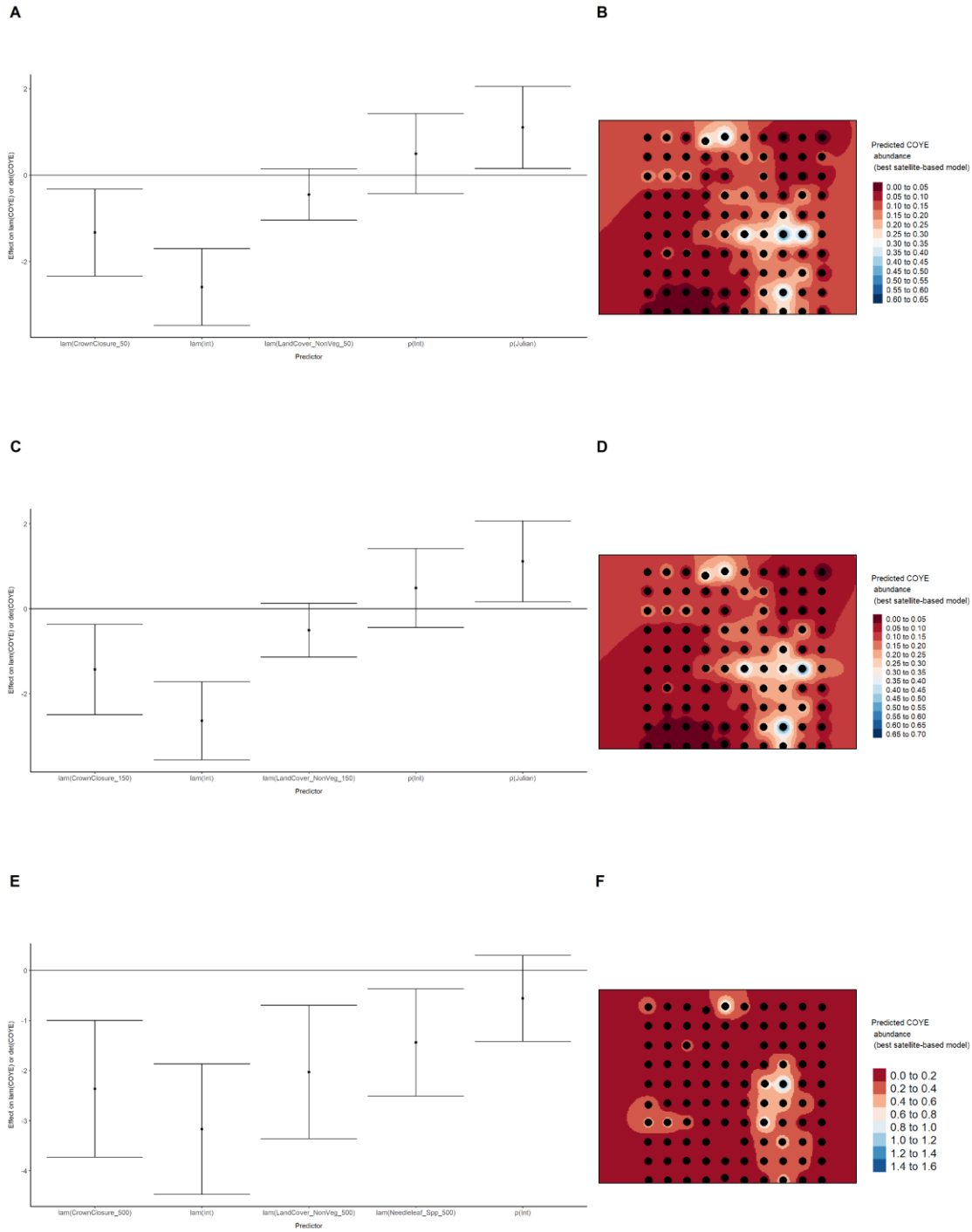
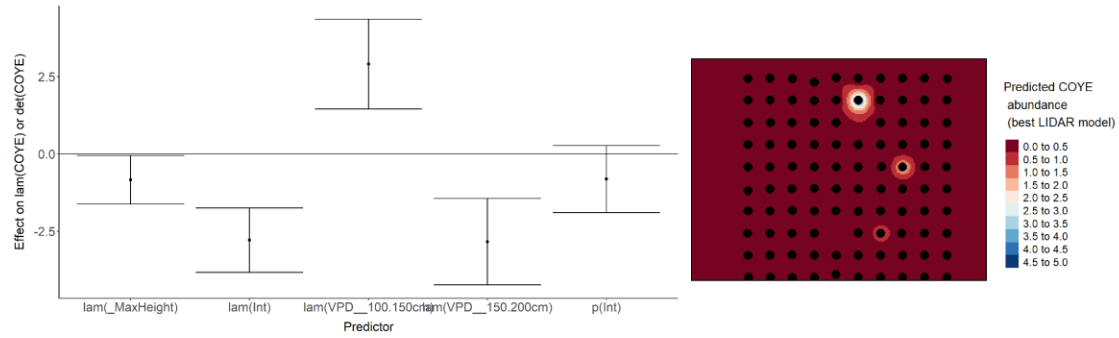
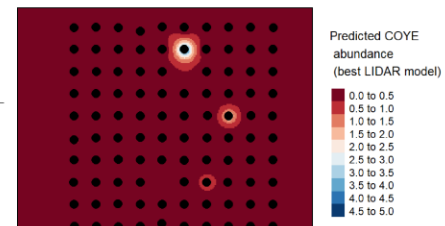


Figure 24. Model coefficients for the best N -mixture model predicting abundance of Common Yellowthroat *Geothlypis trichas* from LIDAR-based data at the 150-m scale (AIC= 113.58) (A), and 500-m scale (AIC= 114.43) (C), along with predicted abundances of this species in the Kirby grid from these respective models (B,D).

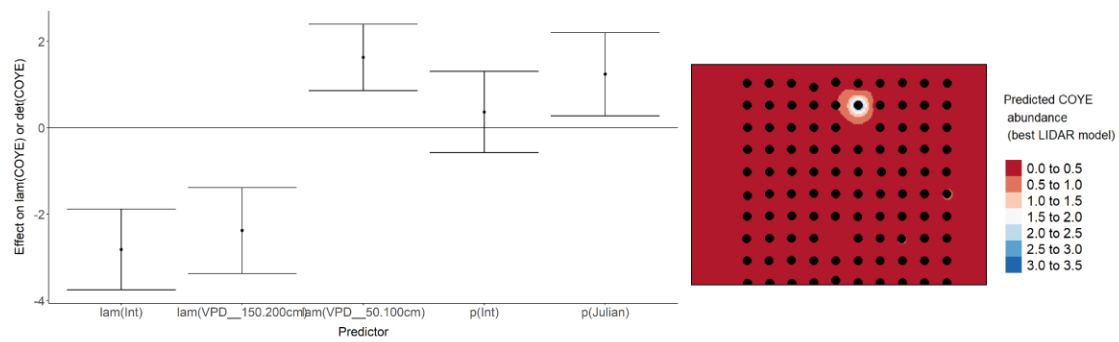
A



B



C



D

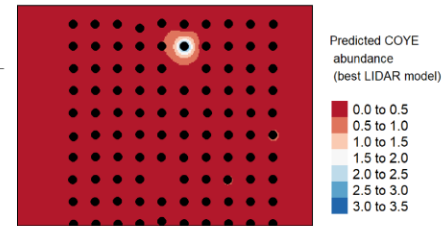


Figure 25. Model coefficients for the A) AVI-based (AIC= 109.5), C) satellite-based (AIC= 120), E) lidar-based (AIC= 113.58), and G) composite (AIC= 108.68) N-mixture models predicting abundance of Common Yellowthroat *Geothlypis trichas*, along with predicted abundances of this species in the Kirby grid from these respective models (B,D,F,H).

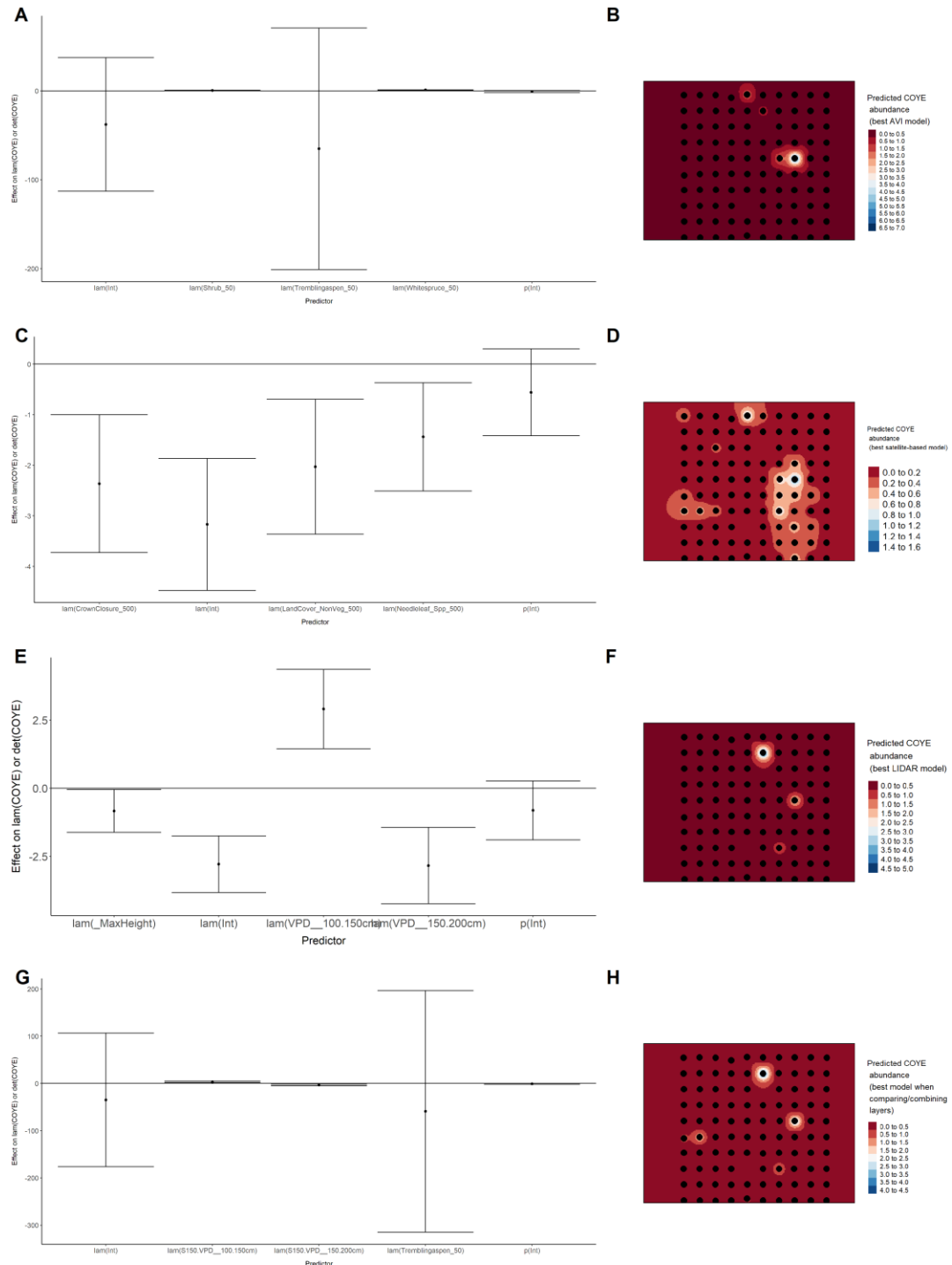


Figure 26. Model coefficients for the best N-mixture model predicting abundance of Dark-eyed Junco *Junco hyemalis* from Alberta Vegetation Inventory (AVI) shapefile-based data at the 50-m

scale ($AIC= 426.85$) (A), 150-m scale ($AIC= 422$) (C), and 500-m scale ($AIC= 437.79$) (E), along with predicted abundances of this species in the Kirby grid from these respective models (B,D,F).

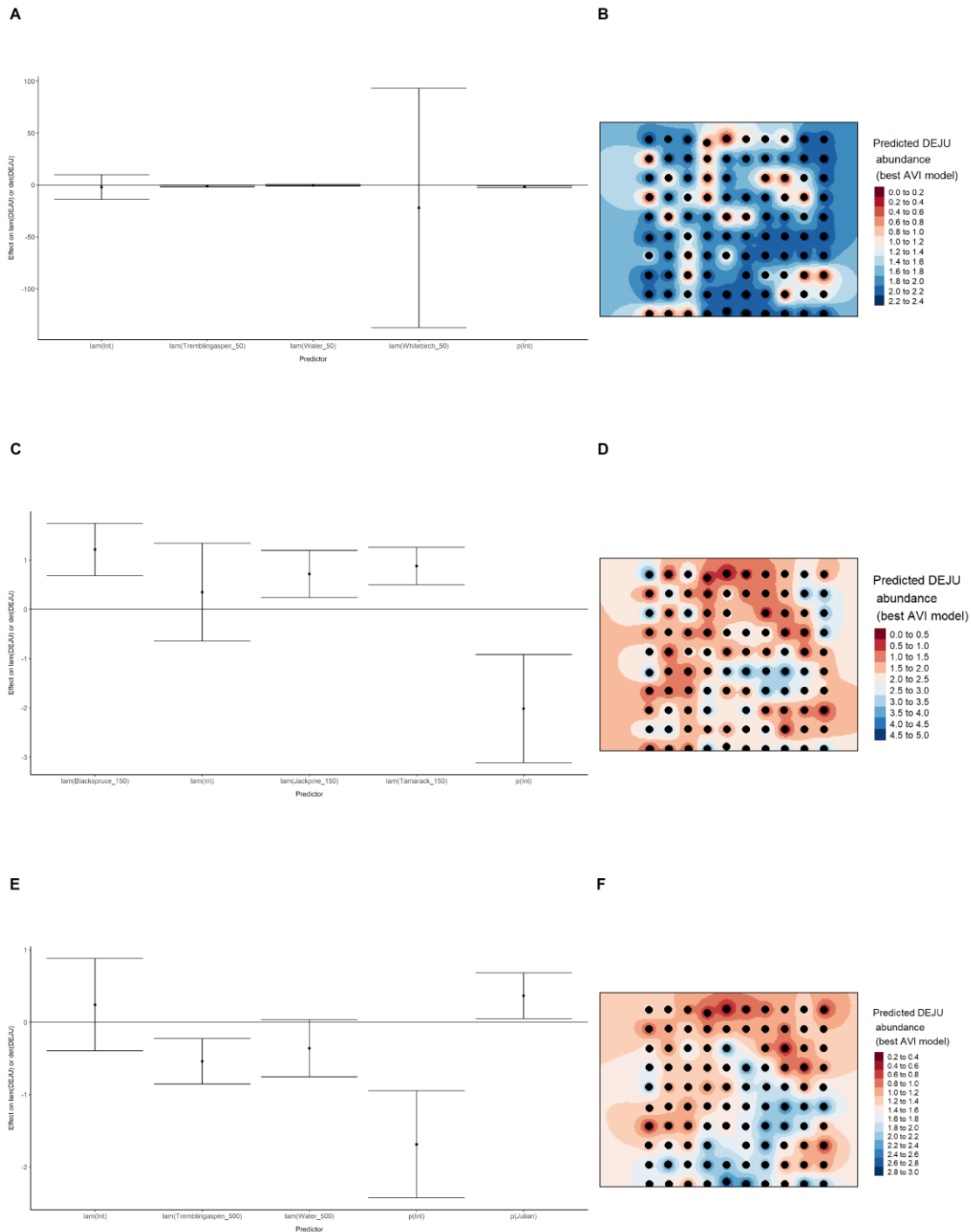


Figure 27. Model coefficients for the best N -mixture model predicting abundance of Dark-eyed Junco *Juncos hyemalis* from satellite-based data at the 50-m scale ($AIC= 436.37$) (A), 150-m scale

(AIC= 438.02) (C), and 500-m scale (AIC= 443) (E), along with predicted abundances of this species in the Kirby grid from these respective models (B,D,F).

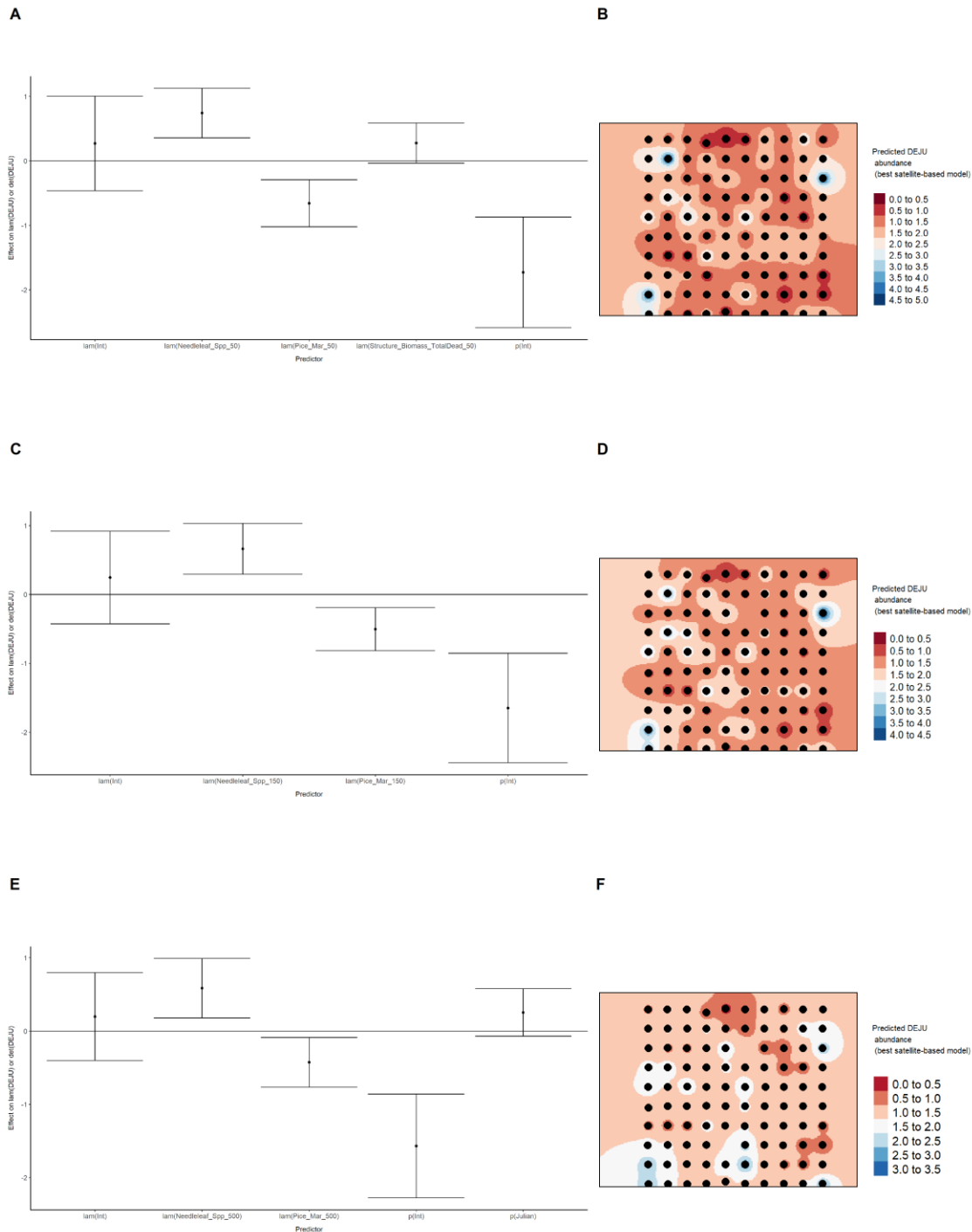
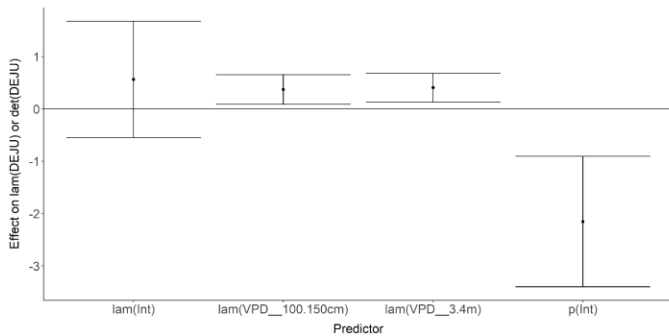


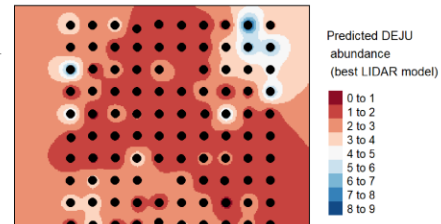
Figure 28. Model coefficients for the best *N*-mixture model predicting abundance of Dark-eyed Junco *Junco hyemalis* from LIDAR-based data at the 150-m scale (AIC= 422.02) (A), and 500-m

scale (AIC= 430.56) (C), along with predicted abundances of this species in the Kirby grid from these respective models (B,D).

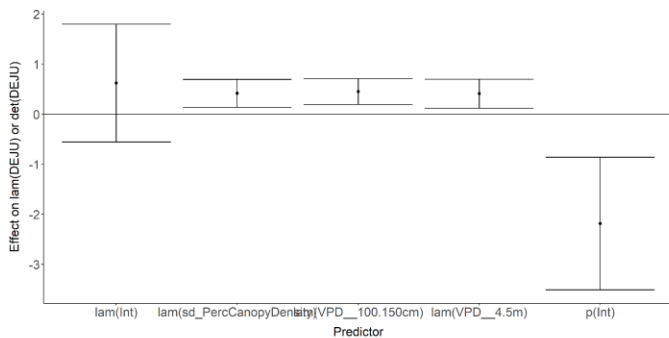
A



B



C



D

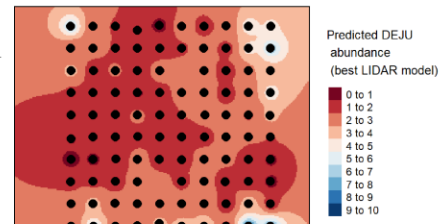


Figure 29. Model coefficients for the A) AVI-based (AIC= 422), C) satellite-based (AIC= 436.37), E) lidar-based (AIC= 422.02), and G) composite (AIC= 418.04) N-mixture models predicting

abundance of Dark-eyed Junco *Junco hyemalis*, along with predicted abundances of this species in the Kirby grid from these respective models (B,D,F,H).

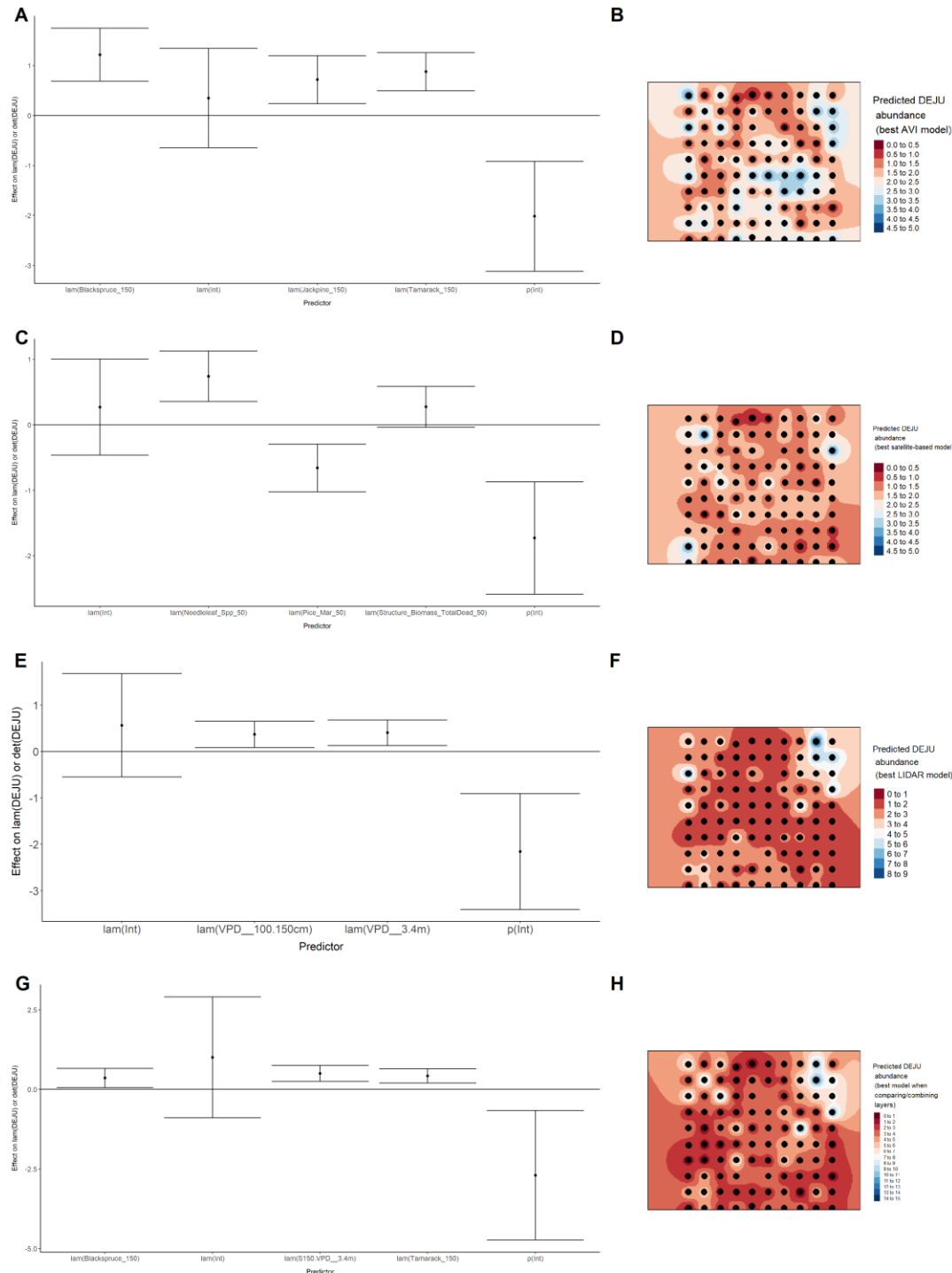


Figure 30. Model coefficients for the best *N*-mixture model predicting abundance of Gray Jay *Perisoreus canadensis* from Alberta Vegetation Inventory (AVI) shapefile-based data at the 50-m

scale (AIC= 466.06) (A), 150-m scale (AIC= 459.33) (C), and 500-m scale (AIC= 465.1) (E), along with predicted abundances of this species in the Kirby grid from these respective models (B,D,F).

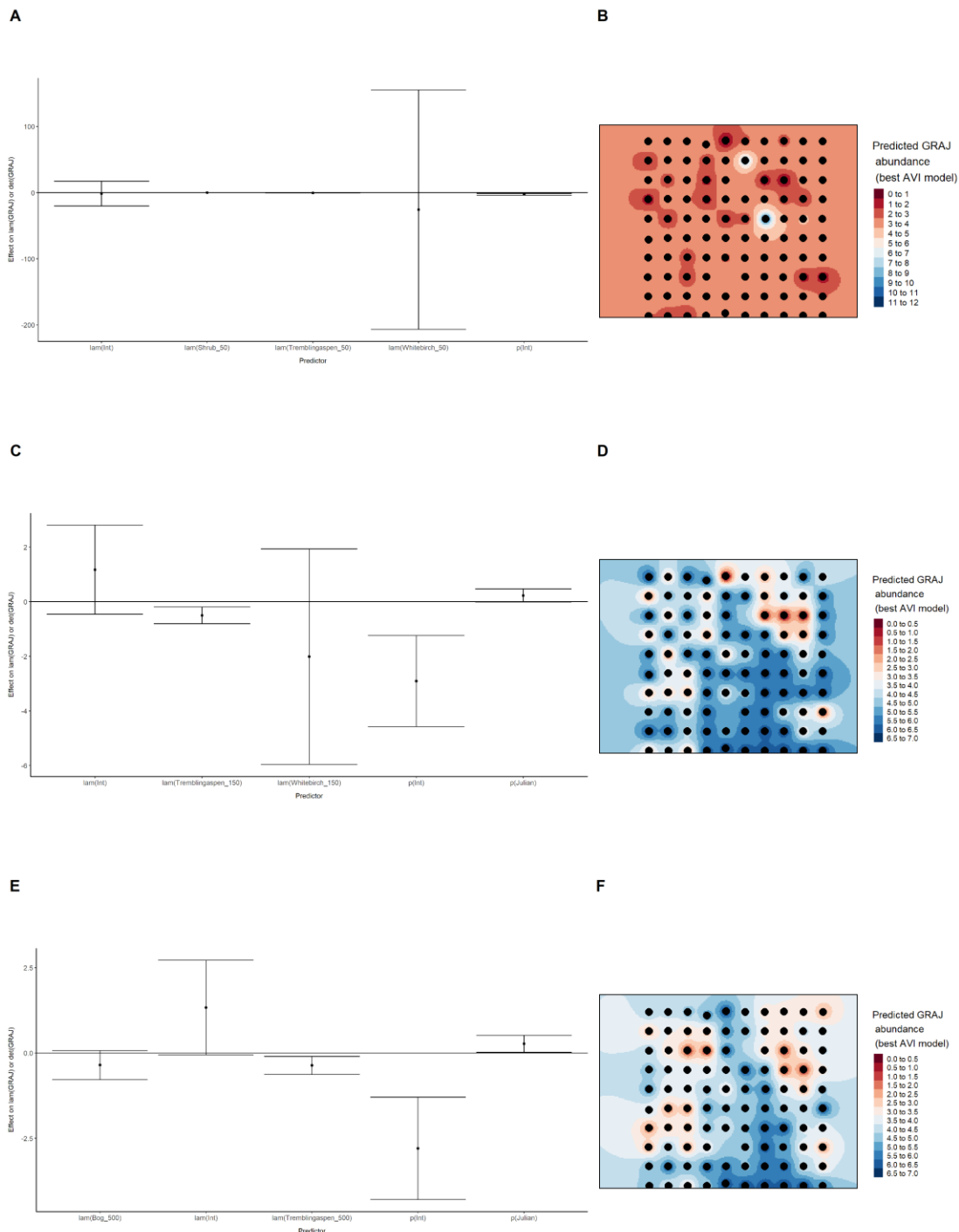


Figure 31. Model coefficients for the best N -mixture model predicting abundance of Gray Jay *Perisoreus canadensis* from satellite-based data at the 50-m scale (AIC= 460.21) (A), 150-m scale

(AIC= 462.02) (C), and 500-m scale (AIC= 461.91) (E), along with predicted abundances of this species in the Kirby grid from these respective models (B,D,F).

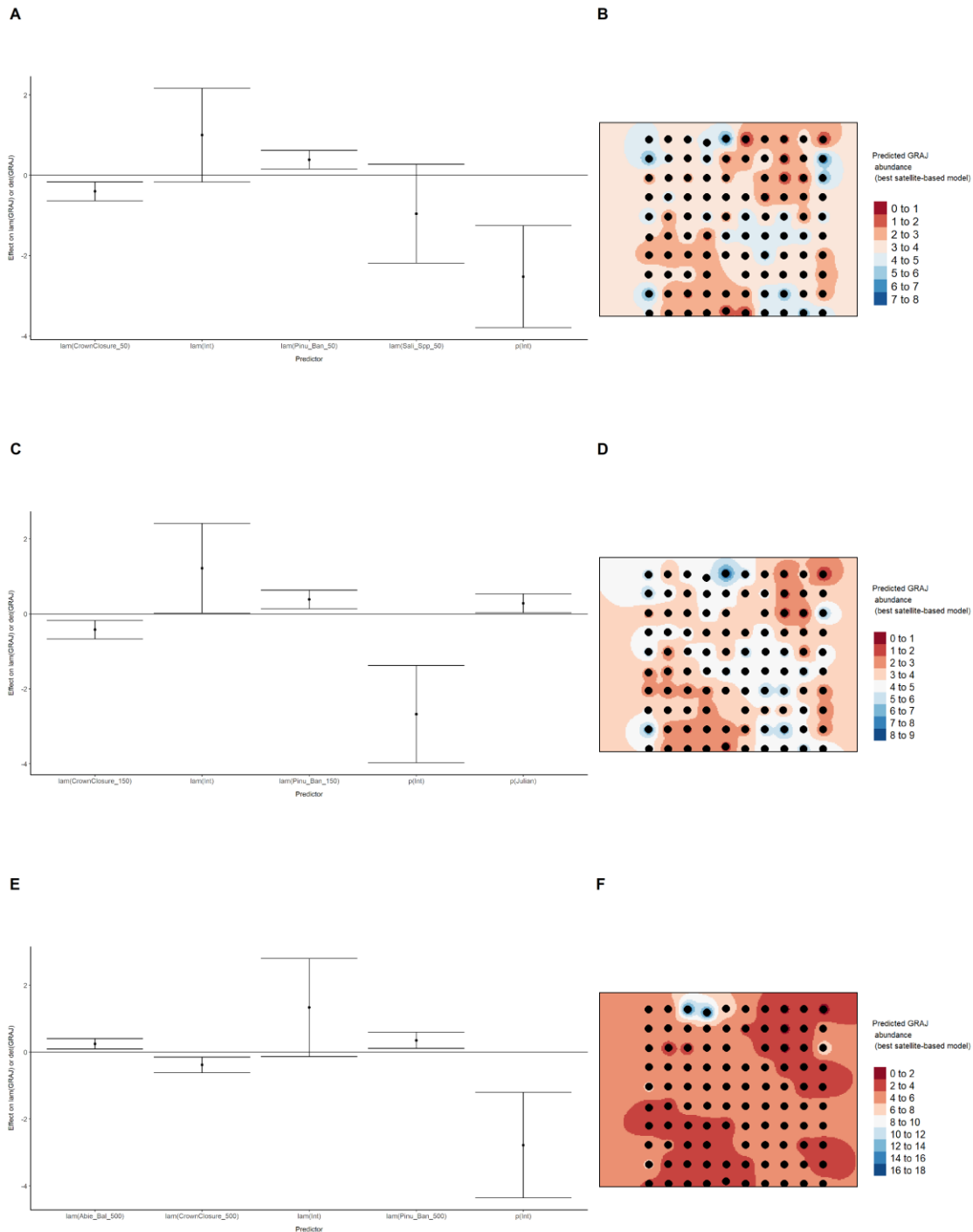
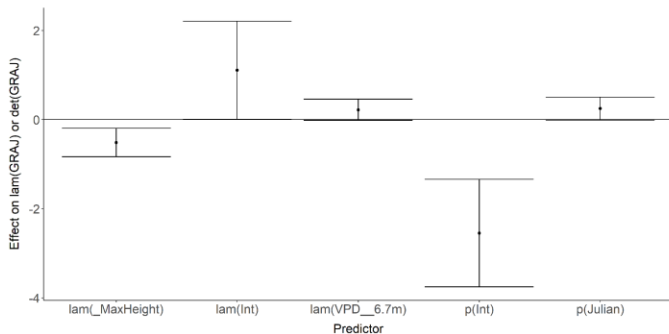


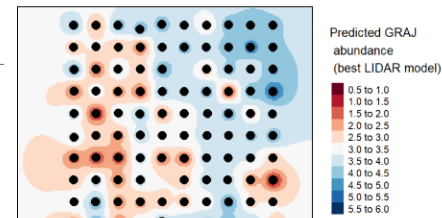
Figure 32. Model coefficients for the best N -mixture model predicting abundance of Gray Jay *Perisoreus canadensis* from LIDAR-based data at the 150-m scale (AIC= 465.27) (A), and 500-m

scale (AIC= 461.19) (C), along with predicted abundances of this species in the Kirby grid from these respective models (B,D).

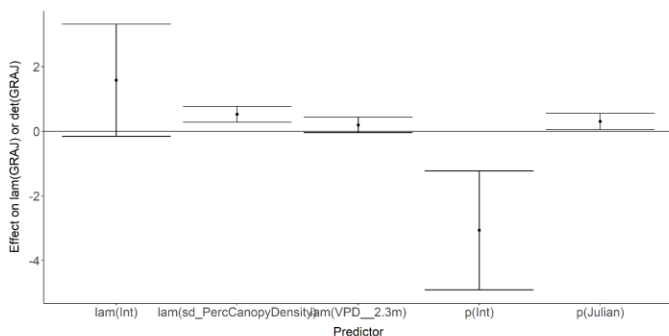
A



B



C



D

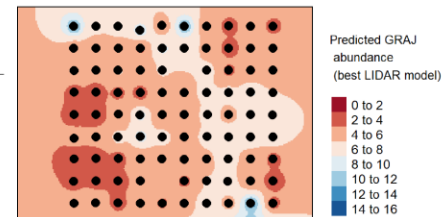


Figure 33. Model coefficients for the A) AVI-based (AIC= 459.33), C) satellite-based (AIC= 460.21), E) lidar-based (AIC= 461.19), and G) composite (AIC= 449.73) N-mixture models

predicting abundance of Gray Jay *Perisoreus canadensis*, along with predicted abundances of this species in the Kirby grid from these respective models (B,D,F,H).

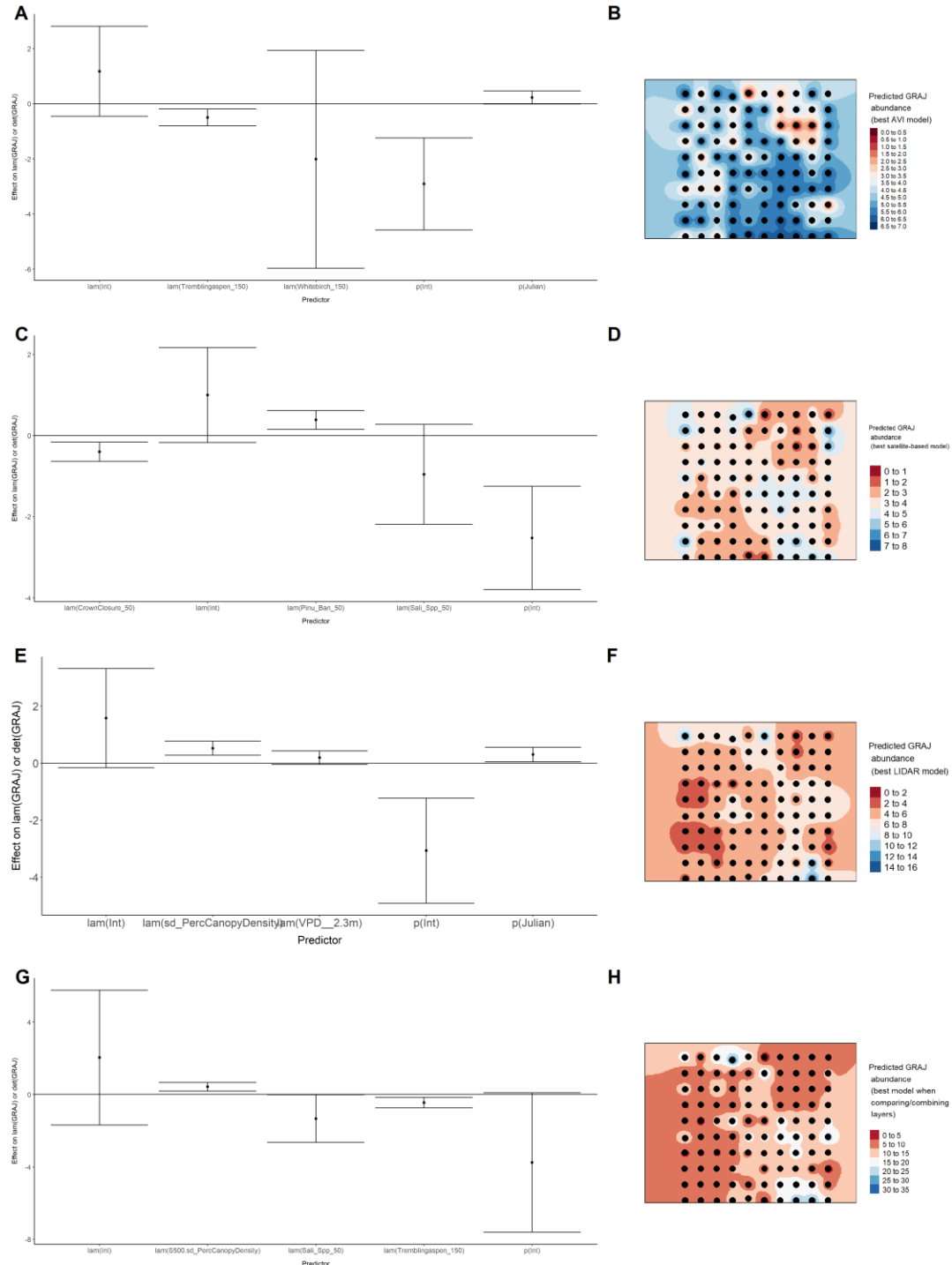


Figure 34. Model coefficients for the best *N*-mixture model predicting abundance of Hermit Thrush *Catharus guttatus* from Alberta Vegetation Inventory (AVI) shapefile-based data at the 50-m scale (AIC= 692.28) (A), 150-m scale (AIC= 688.17) (C), and 500-m scale (AIC= 693.53) (E),

along with predicted abundances of this species in the Kirby grid from these respective models (B,D,F).

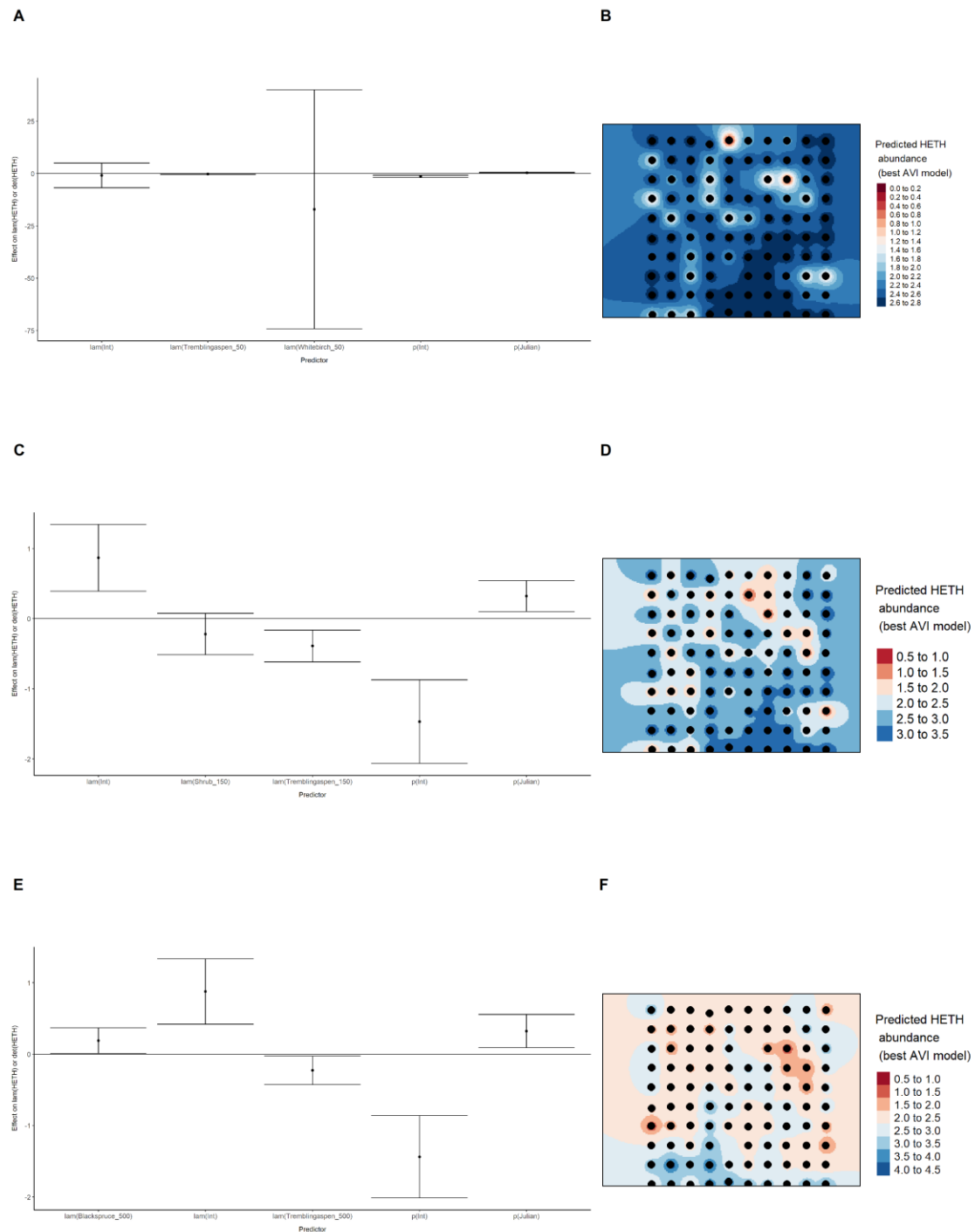


Figure 35. Model coefficients for the best *N*-mixture model predicting abundance of Hermit Thrush *Catharus guttatus* from satellite-based data at the 50-m scale (AIC= 694.13) (A), 150-m

scale ($AIC = 696.2$) (C), and 500-m scale ($AIC = 688.84$) (E), along with predicted abundances of this species in the Kirby grid from these respective models (B,D,F).

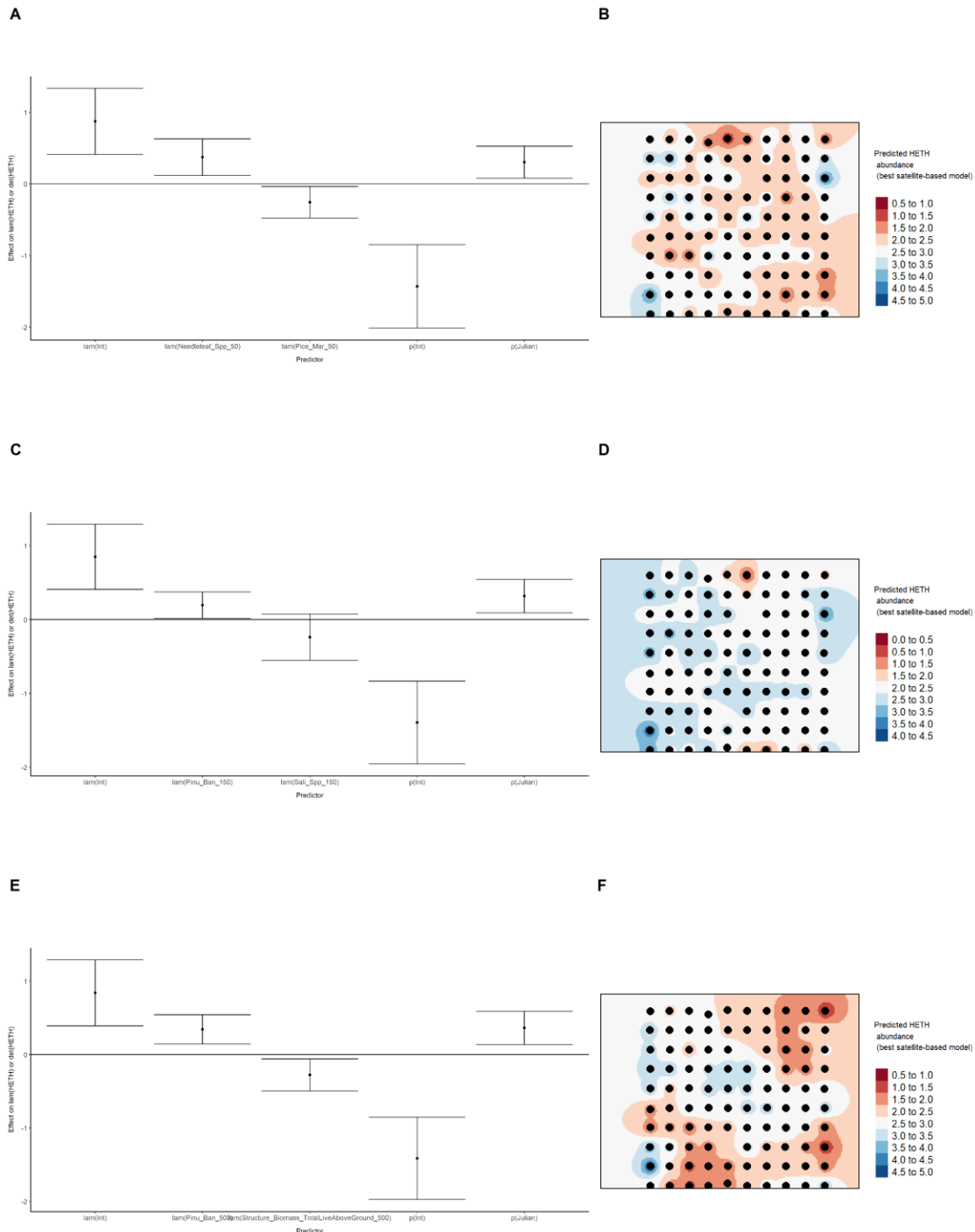
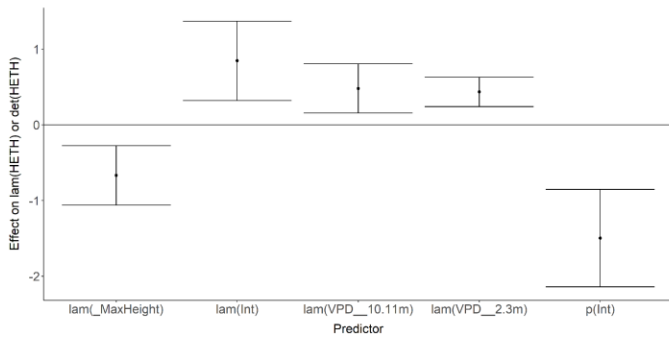


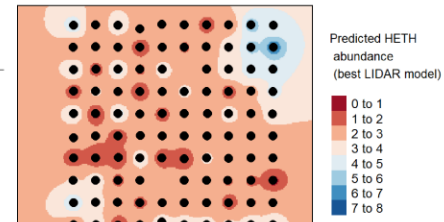
Figure 36. Model coefficients for the best N -mixture model predicting abundance of Hermit Thrush (*Catharus guttatus*) from LIDAR-based data at the 150-m scale ($AIC = 679.97$) (A), and 500-

m scale (AIC= 676.18) (C), along with predicted abundances of this species in the Kirby grid from these respective models (B,D).

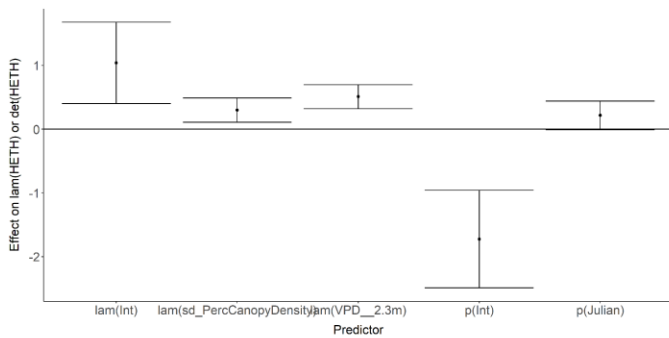
A



B



C



D

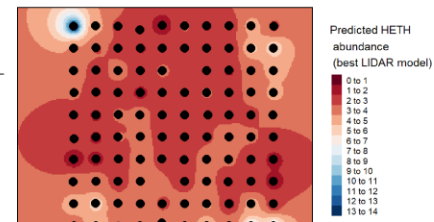


Figure 37. Model coefficients for the A) AVI-based (AIC= 688.17), C) satellite-based (AIC= 688.84), E) lidar-based (AIC= 676.18), and G) composite (AIC= 673.9) N-mixture models

predicting abundance of Hermit Thrush *Catharus guttatus*, along with predicted abundances of this species in the Kirby grid from these respective models (B,D,F,H).

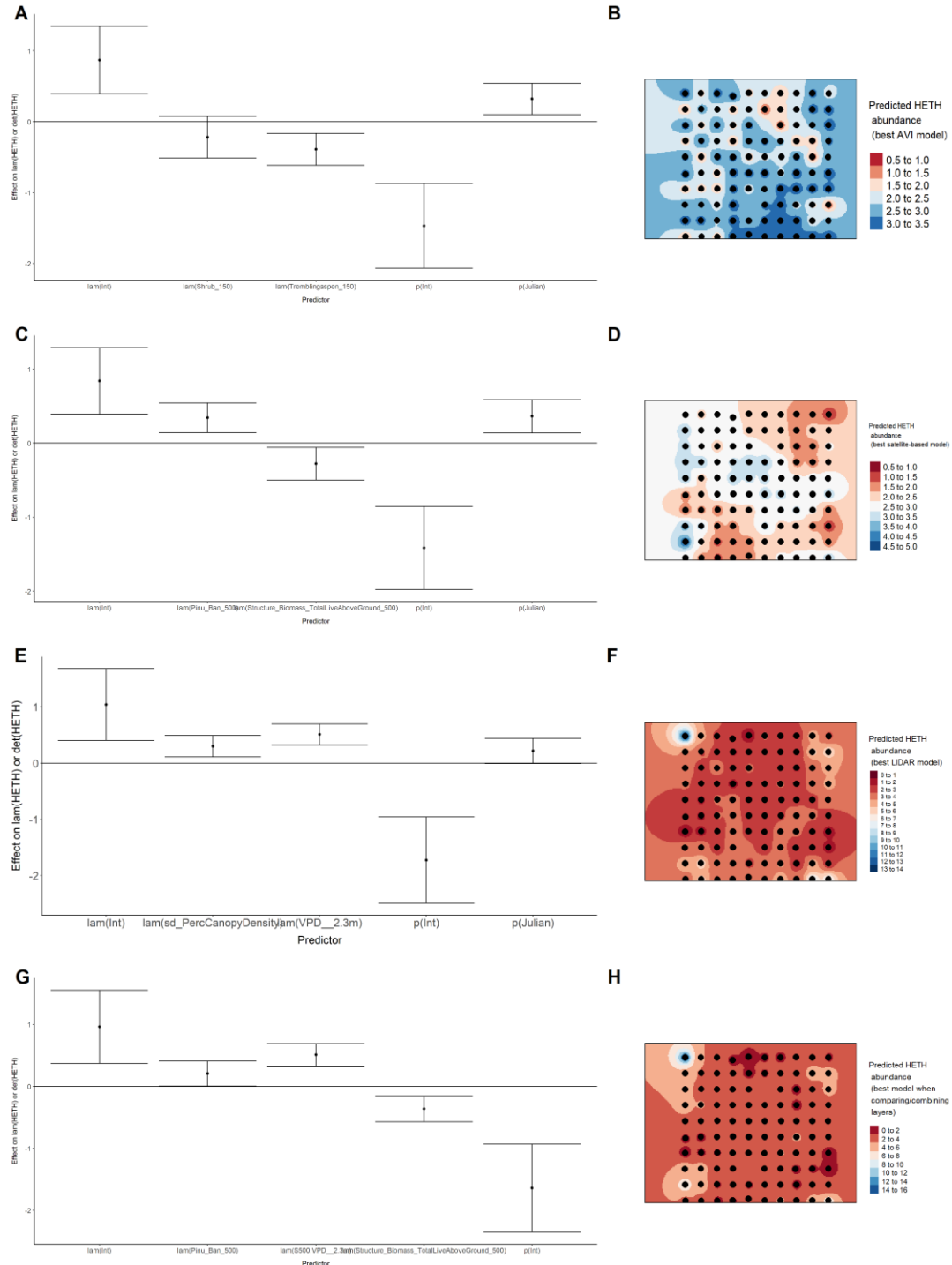


Figure 38. Model coefficients for the best N -mixture model predicting abundance of Le Conte's Sparrow *Ammodramus lecontei* from Alberta Vegetation Inventory (AVI) shapefile-based data at the 50-m scale ($\text{AIC}= 251.72$) (A), 150-m scale ($\text{AIC}= 242.8$) (C), and 500-m scale ($\text{AIC}= 243.47$)

(E), along with predicted abundances of this species in the Kirby grid from these respective models (B,D,F).

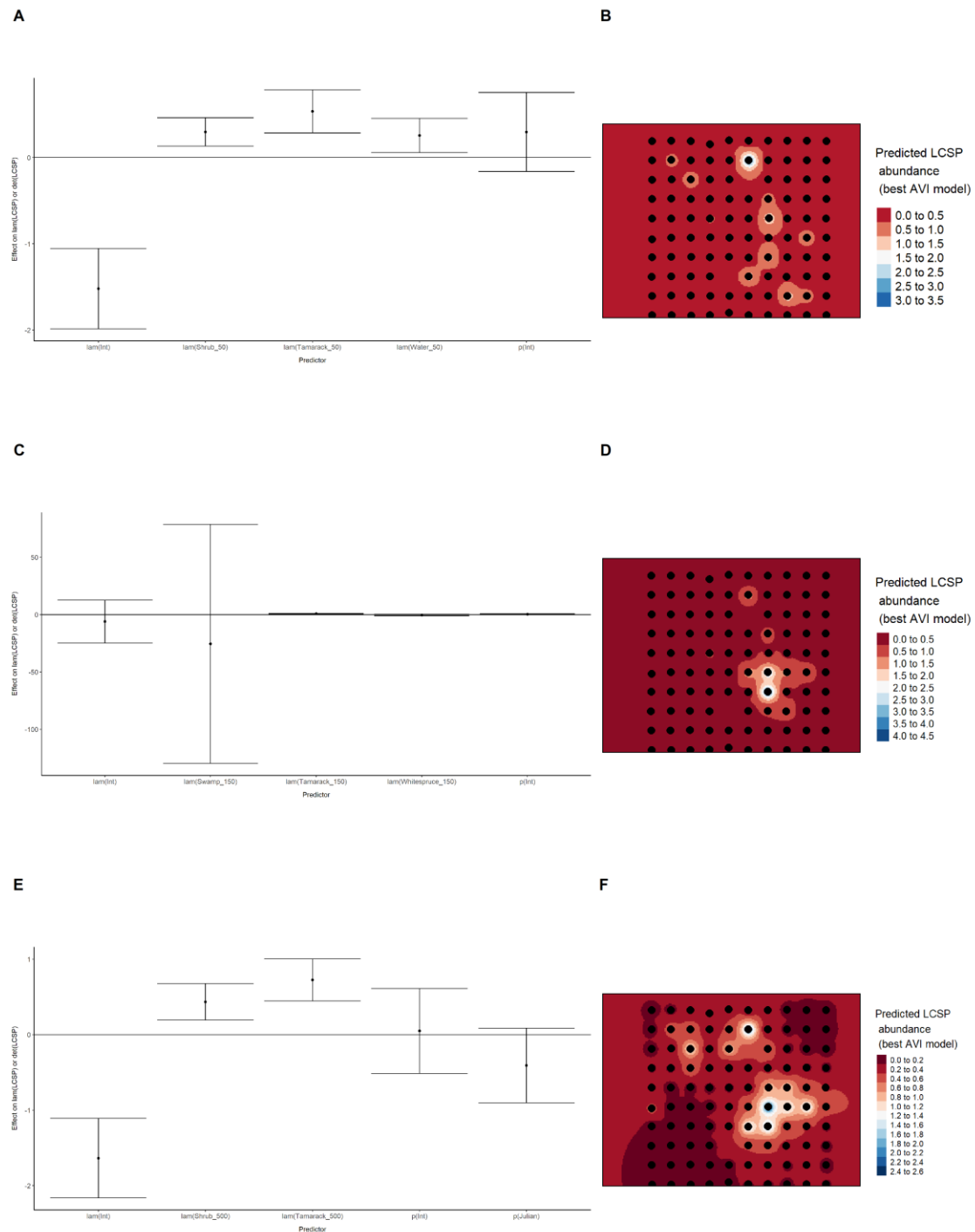


Figure 39. Model coefficients for the best N -mixture model predicting abundance of Le Conte's Sparrow *Ammodramus lecontei* from satellite-based data at the 50-m scale (AIC= 238.75) (A),

150-m scale (AIC= 240.94) (C), and 500-m scale (AIC= 241.94) (E), along with predicted abundances of this species in the Kirby grid from these respective models (B,D,F).

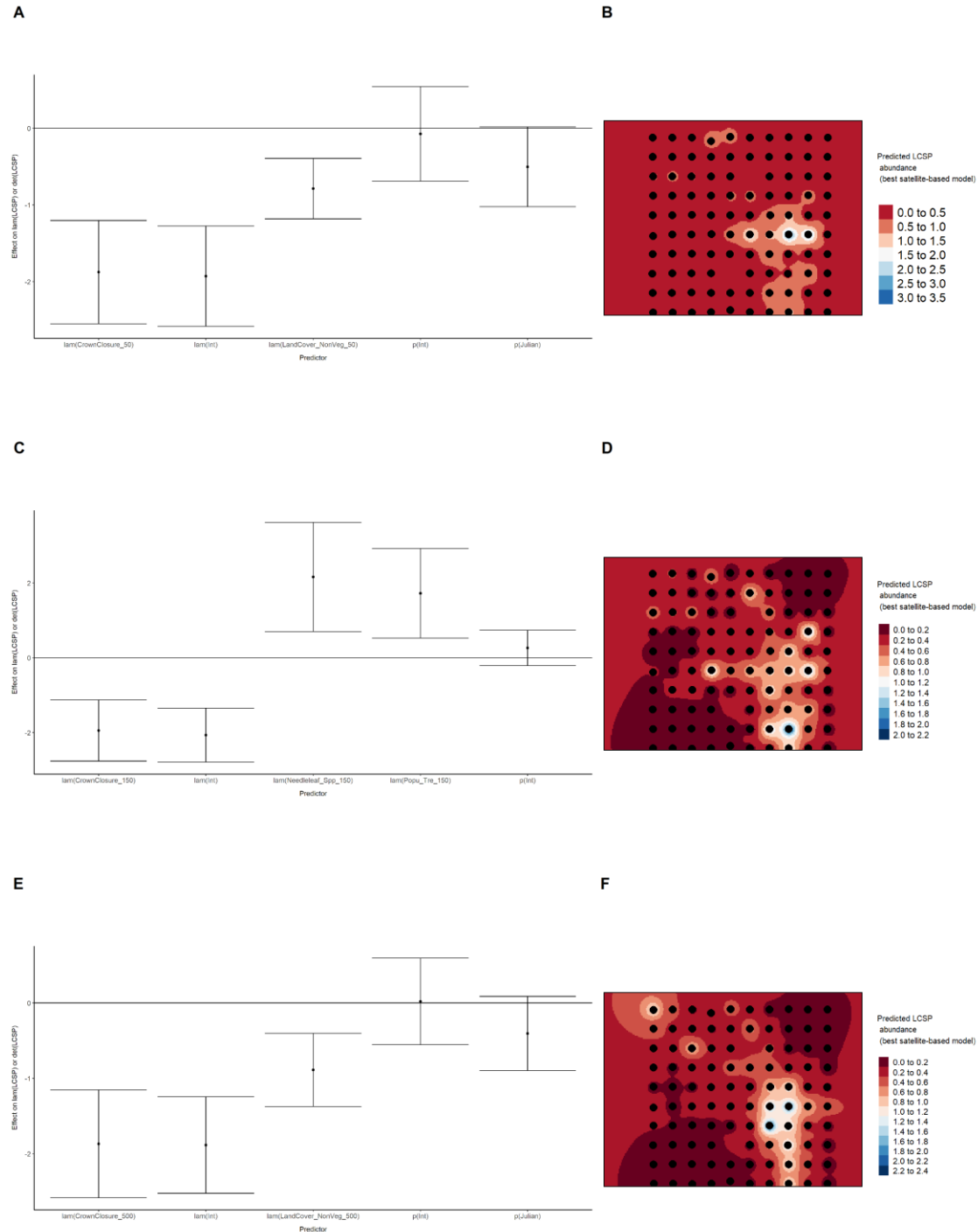


Figure 40. Model coefficients for the best N -mixture model predicting abundance of Le Conte's Sparrow *Ammodramus lecontei* from LIDAR-based data at the 150-m scale (AIC= 227.99) (A), and

500-m scale (AIC= 245.87) (C), along with predicted abundances of this species in the Kirby grid from these respective models (B,D).

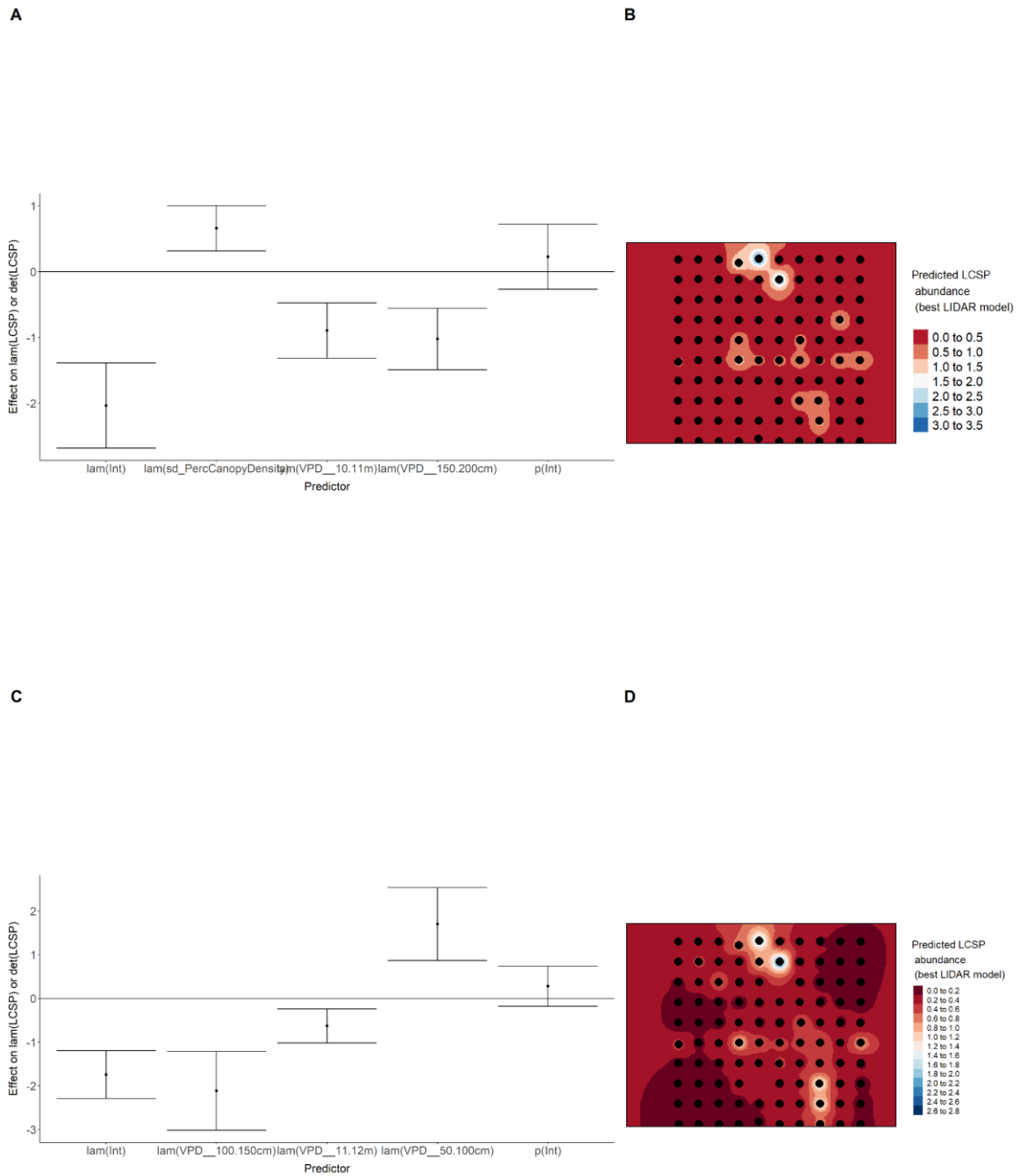


Figure 41. Model coefficients for the A) AVI-based (AIC= 243.47), C) satellite-based (AIC= 238.75), E) lidar-based (AIC= 227.99), and G) composite (AIC= 221.14) N-mixture models

predicting abundance of Le Conte's Sparrow *Ammodramus lecontei*, along with predicted abundances of this species in the Kirby grid from these respective models (B,D,F,H).

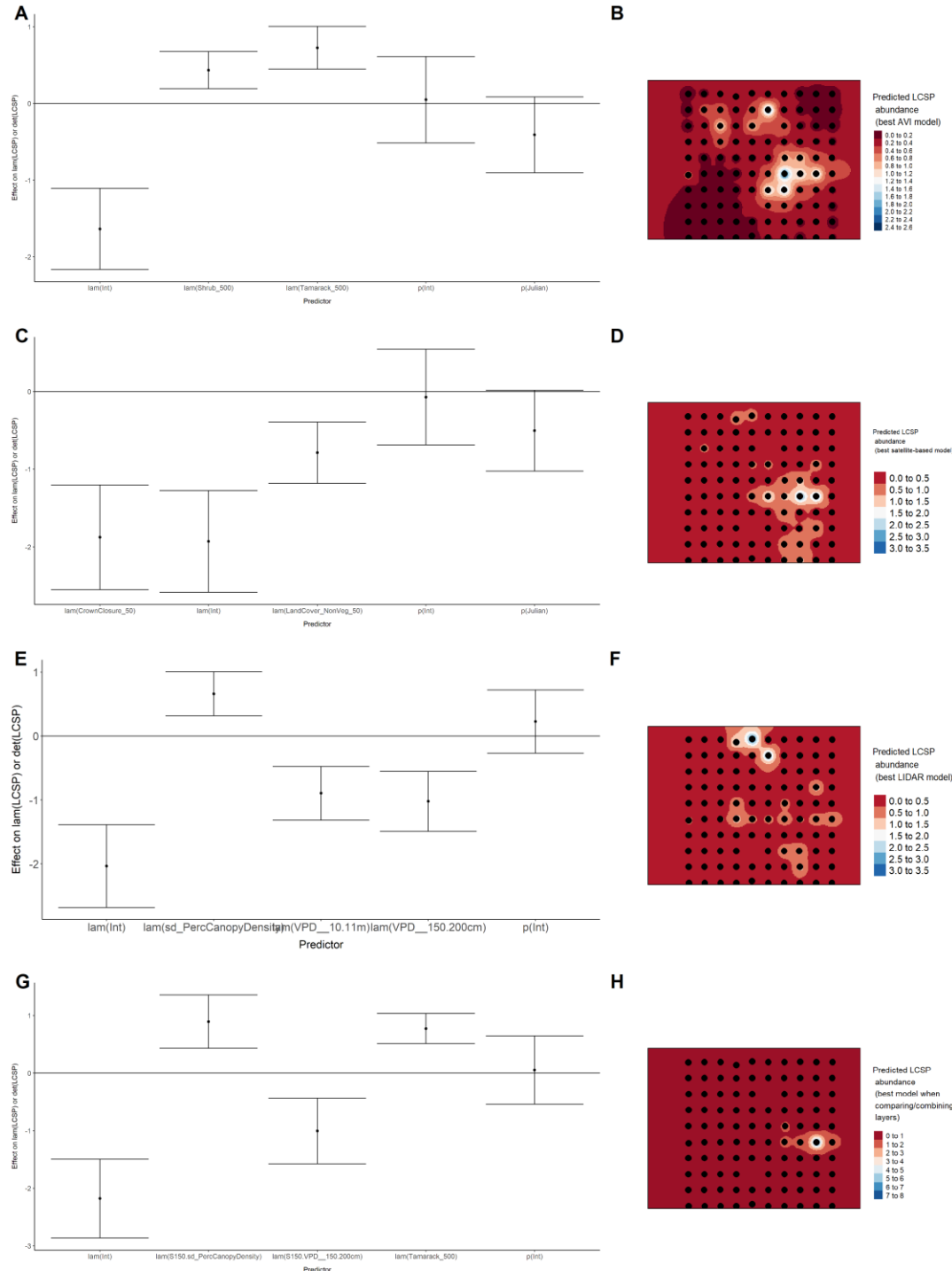


Figure 42. Model coefficients for the best *N*-mixture model predicting abundance of Lincoln's Sparrow *Melospiza lincolni* from Alberta Vegetation Inventory (AVI) shapefile-based data at the 50-m scale (AIC= 473.99) (A), 150-m scale (AIC= 464.25) (C), and 500-m scale (AIC= 471.37) (E),

along with predicted abundances of this species in the Kirby grid from these respective models (B,D,F).

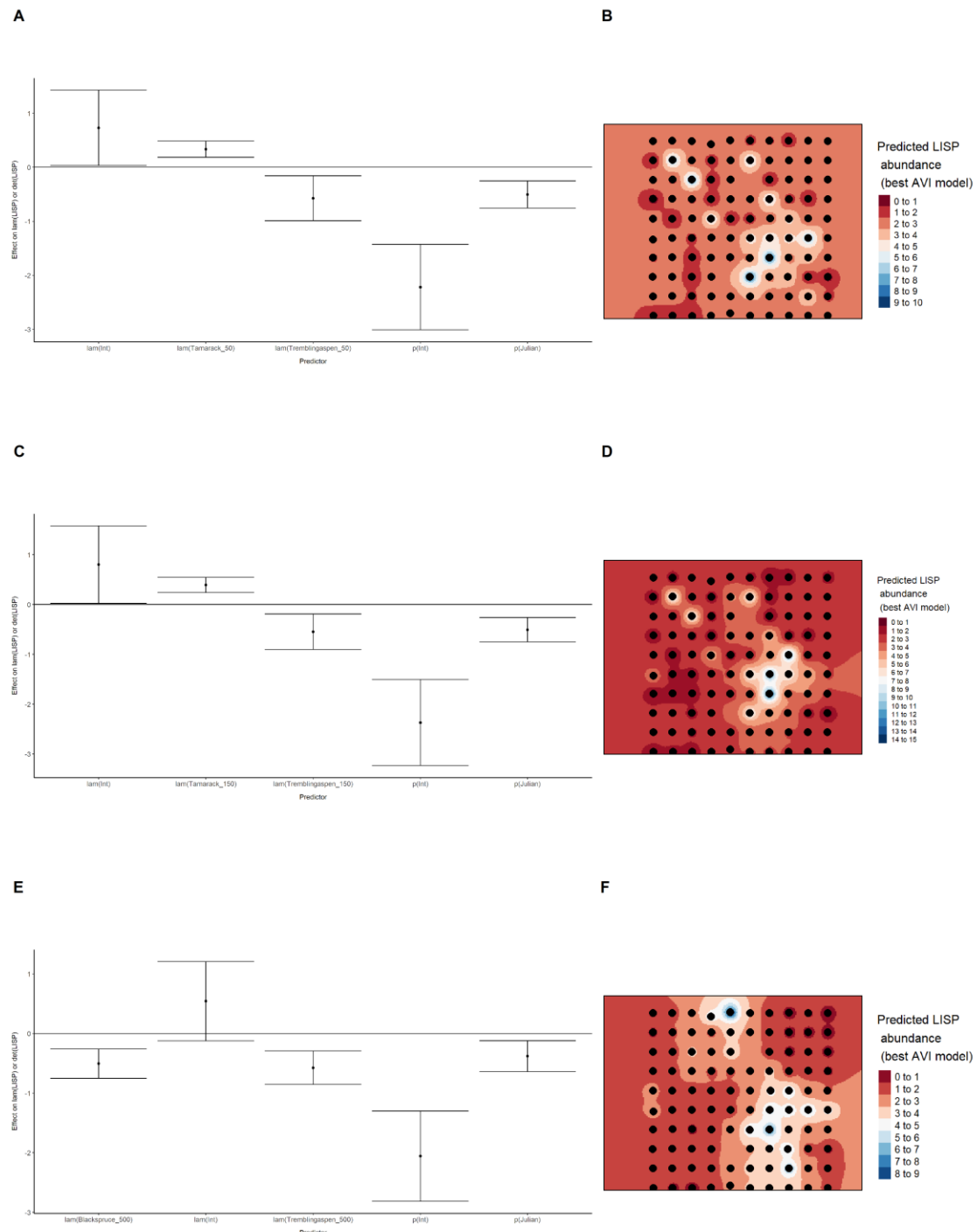


Figure 43. Model coefficients for the best N -mixture model predicting abundance of Lincoln's Sparrow *Melospiza lincolnii* from satellite-based data at the 50-m scale (AIC= 469.21) (A), 150-m

scale (AIC= 465.2) (C), and 500-m scale (AIC= 465.87) (E), along with predicted abundances of this species in the Kirby grid from these respective models (B,D,F).

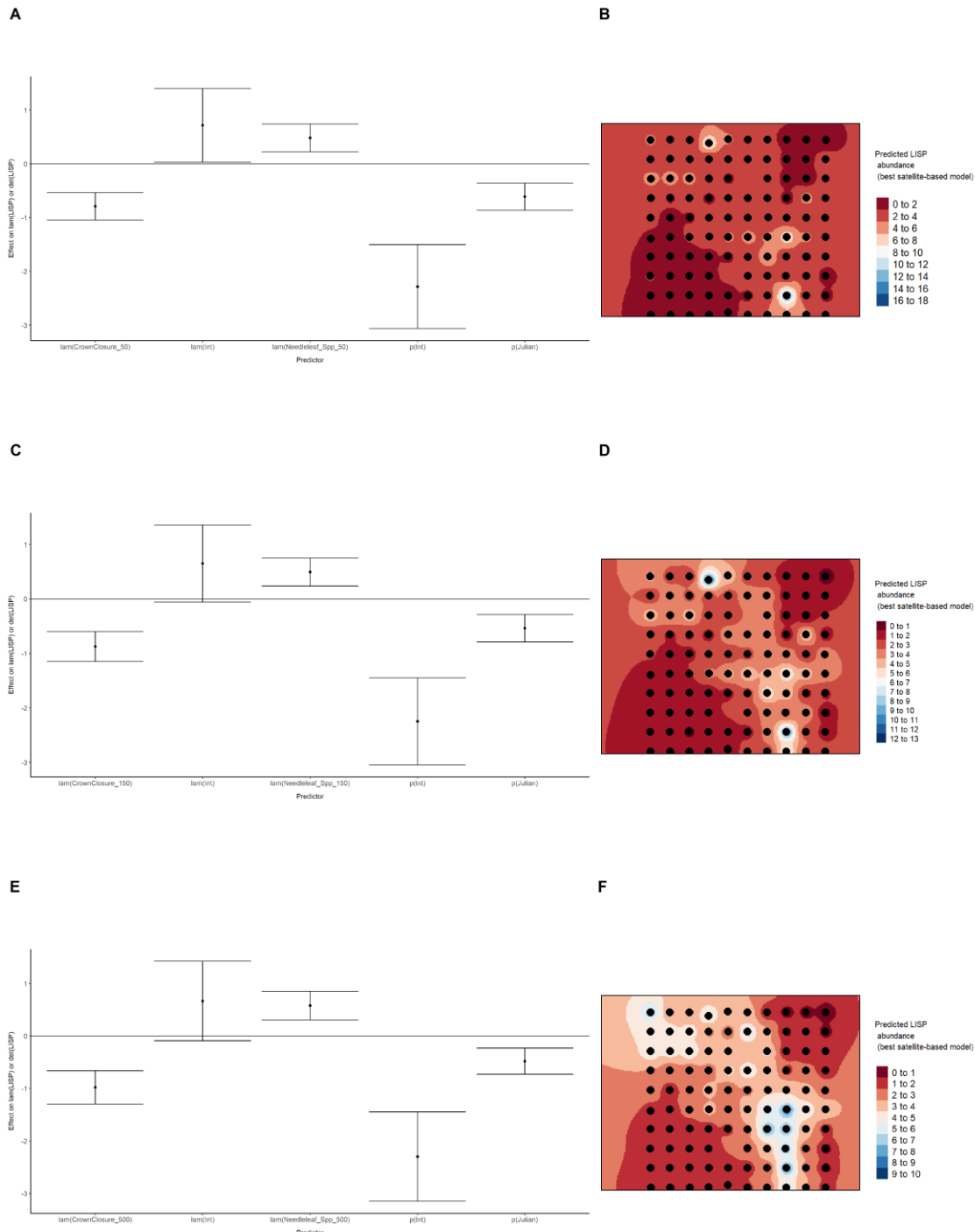
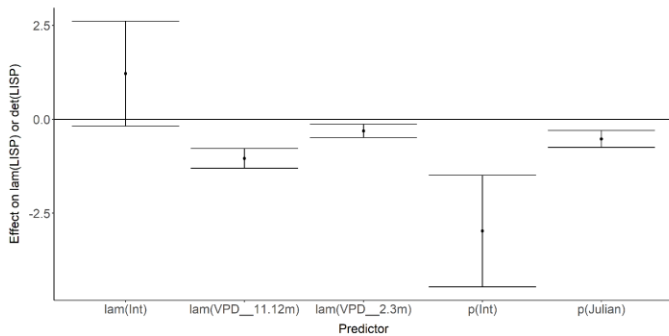


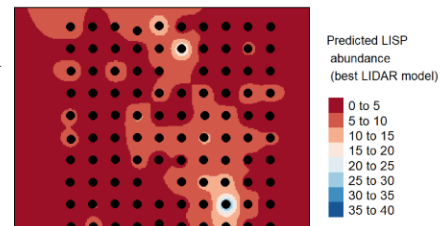
Figure 44. Model coefficients for the best N -mixture model predicting abundance of Lincoln's Sparrow *Melospiza lincolnii* from LIDAR-based data at the 150-m scale (AIC= 439.74) (A), and

500-m scale (AIC= 470.87) (C), along with predicted abundances of this species in the Kirby grid from these respective models (B,D).

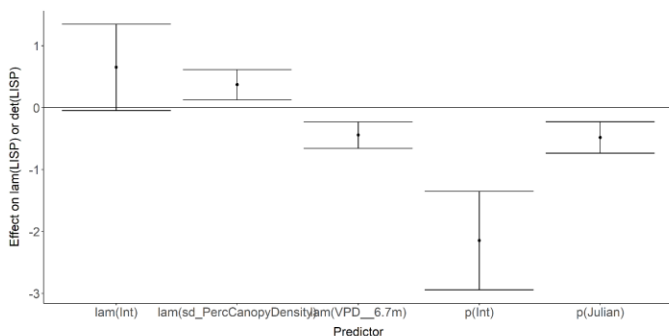
A



B



C



D

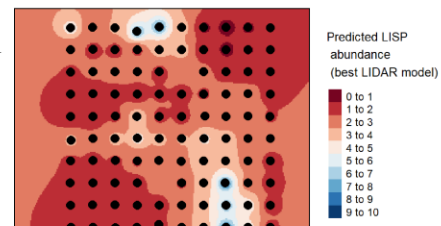


Figure 45. Model coefficients for the A) AVI-based (AIC= 464.25), C) satellite-based (AIC= 465.2), E) lidar-based (AIC= 439.74), and G) composite (AIC= 439.74) N-mixture models predicting

abundance of Lincoln's Sparrow *Melospiza lincolnii*, along with predicted abundances of this species in the Kirby grid from these respective models (B,D,F,H).

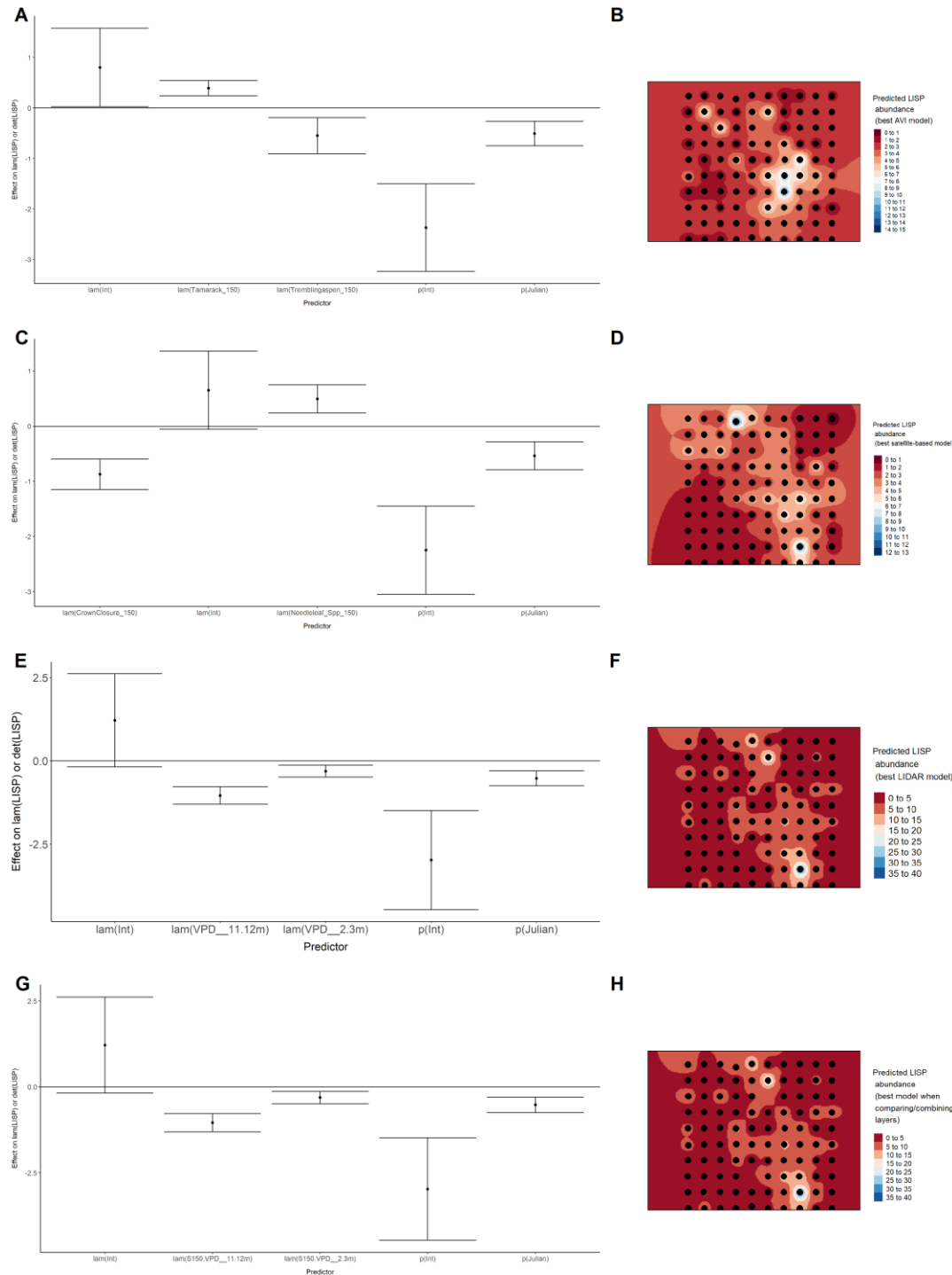


Figure 46. Model coefficients for the best *N*-mixture model predicting abundance of Olive-sided Flycatcher *Contopus cooperi* from Alberta Vegetation Inventory (AVI) shapefile-based data at the 50-m scale (AIC= 152.68) (A), 150-m scale (AIC= 151.83) (C), and 500-m scale (AIC= 133.74) (E),

along with predicted abundances of this species in the Kirby grid from these respective models (B,D,F).

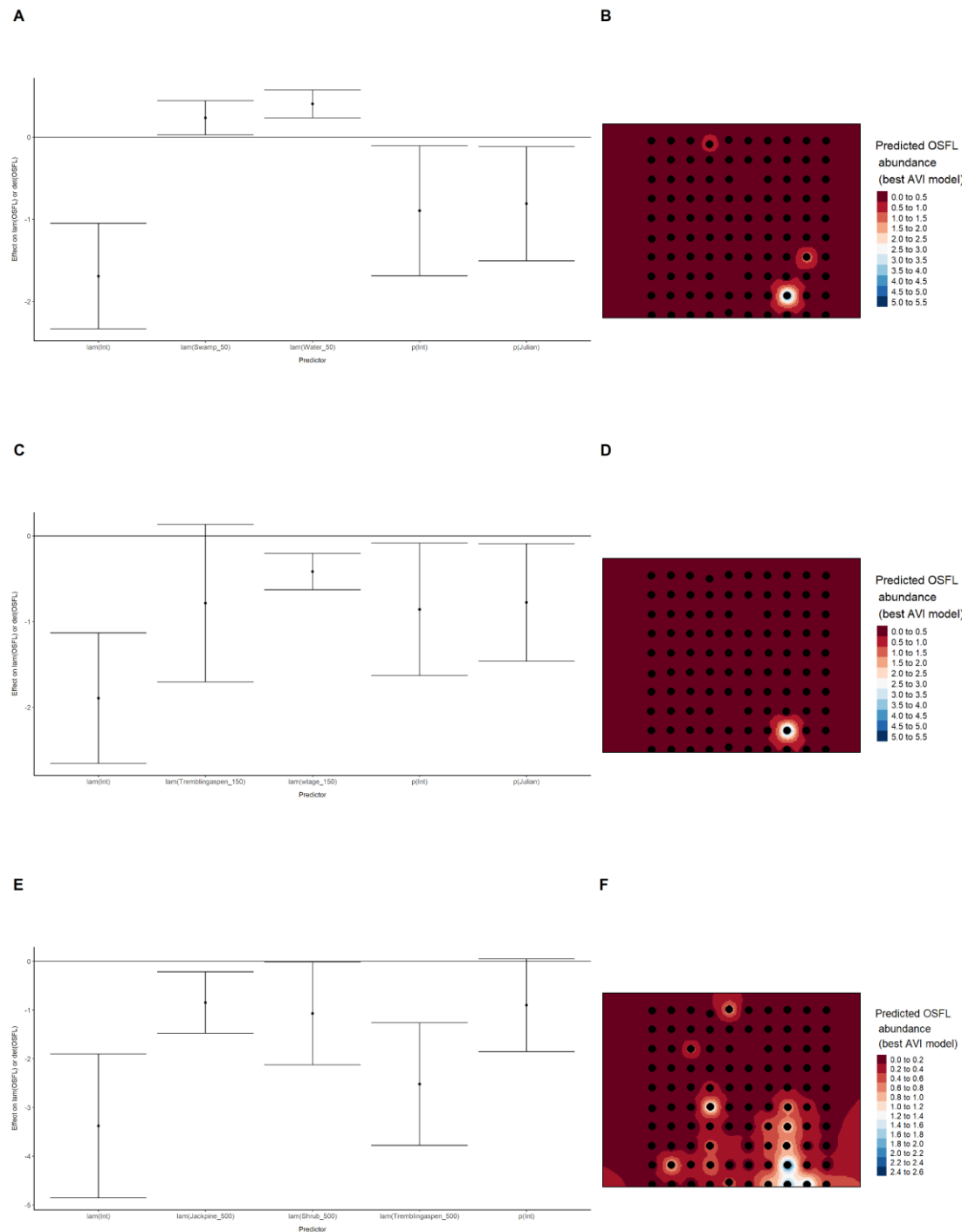


Figure 47. Model coefficients for the best N -mixture model predicting abundance of Olive-sided Flycatcher *Contopus cooperi* from satellite-based data at the 50-m scale (AIC= 153.33) (A), 150-

m scale (AIC= 148.27) (C), and 500-m scale (AIC= 130.55) (E), along with predicted abundances of this species in the Kirby grid from these respective models (B,D,F).

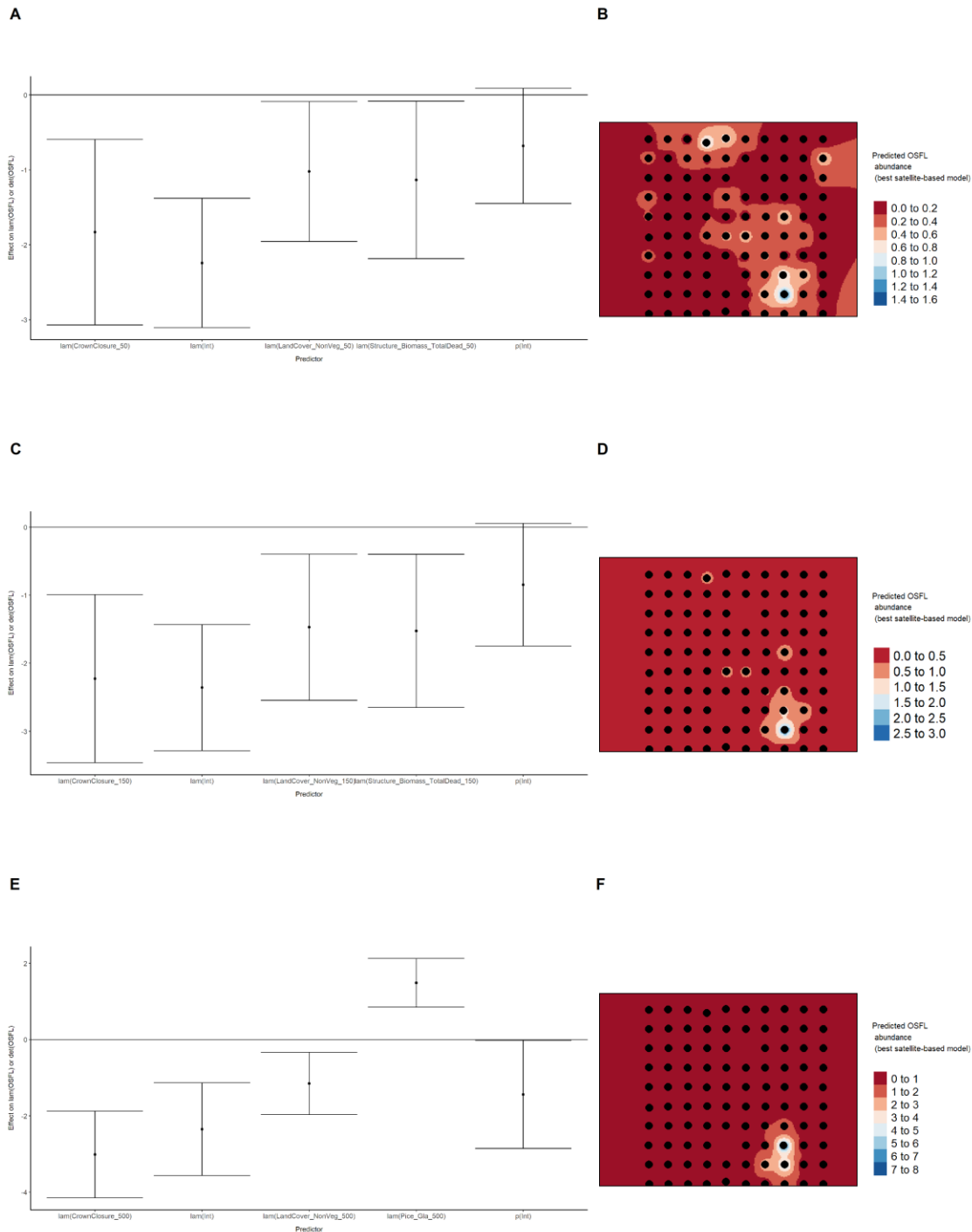


Figure 48. Model coefficients for the best *N*-mixture model predicting abundance of Olive-sided Flycatcher *Contopus cooperi* from LIDAR-based data at the 150-m scale (AIC= 141.84) (A), and

500-m scale (AIC= 126.82) (C), along with predicted abundances of this species in the Kirby grid from these respective models (B,D).

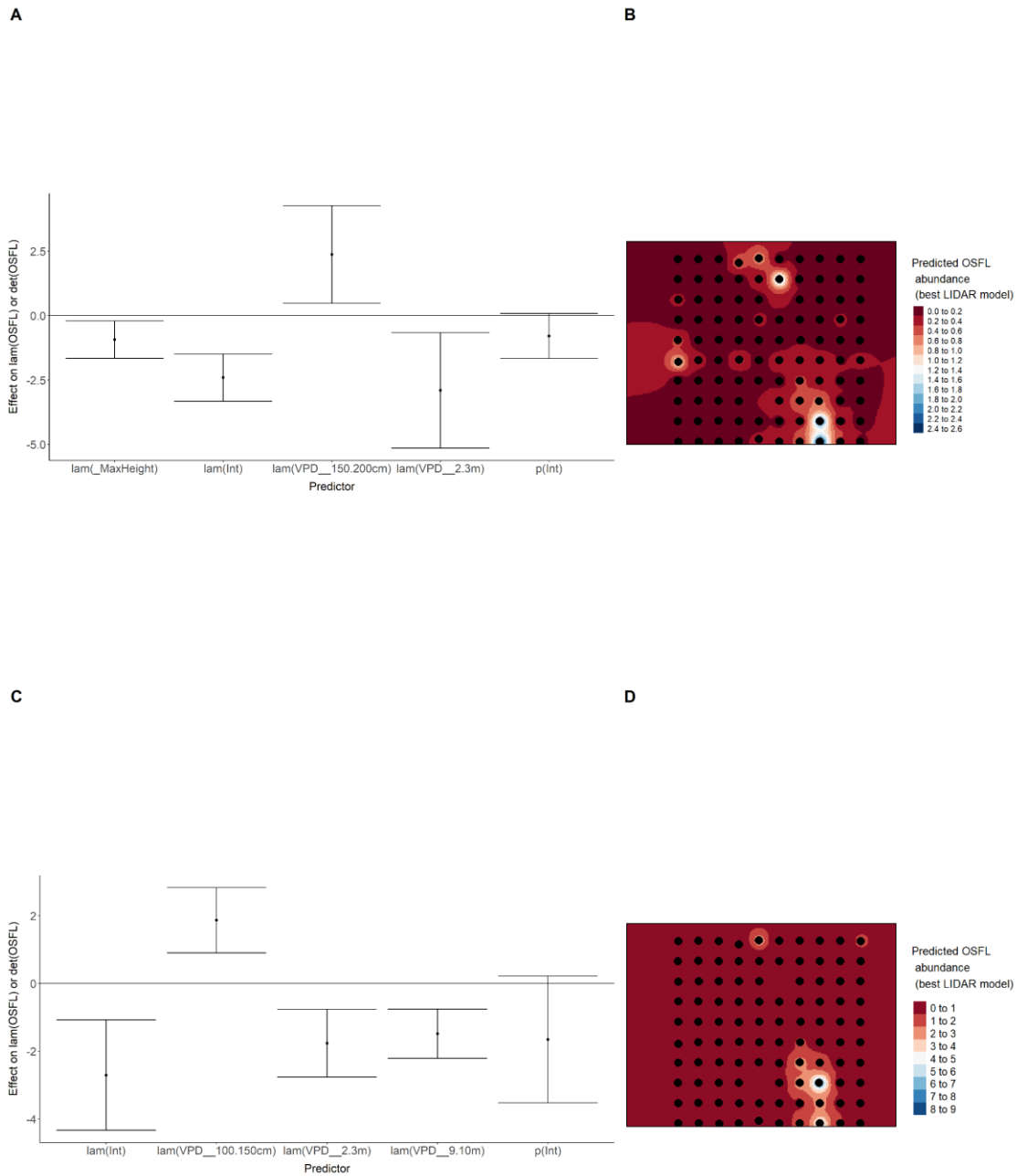


Figure 49. Model coefficients for the A) AVI-based (AIC= 133.74), C) satellite-based (AIC= 130.55), E) lidar-based (AIC= 126.82), and G) composite (AIC= 126.82) *N*-mixture models

predicting abundance of Olive-sided Flycatcher *Contopus cooperi*, along with predicted abundances of this species in the Kirby grid from these respective models (B,D,F,H).

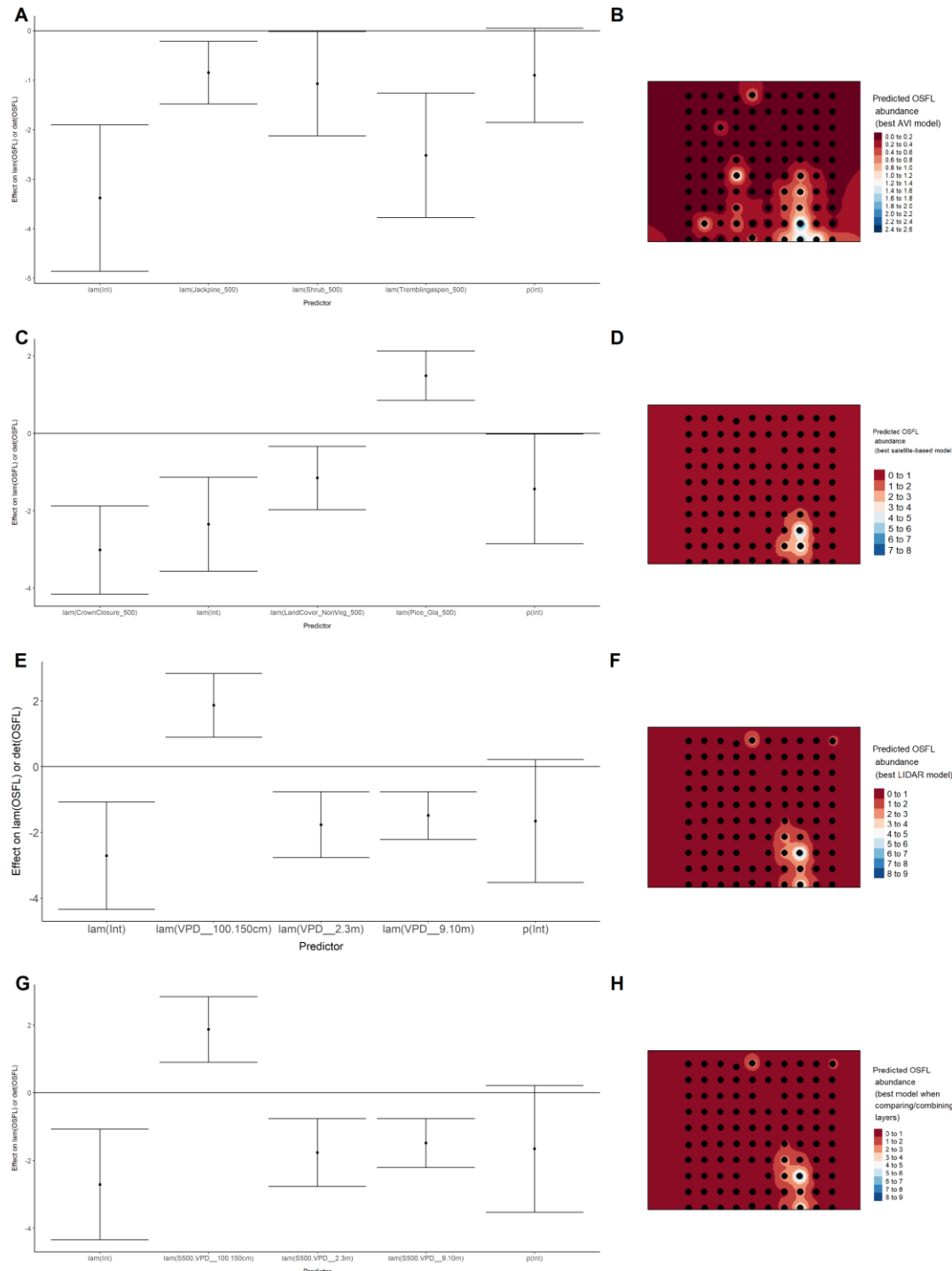


Figure 50. Model coefficients for the best *N*-mixture model predicting abundance of Ovenbird *Seiurus aurocapillus* from Alberta Vegetation Inventory (AVI) shapefile-based data at the 50-m

scale (AIC= 332.04) (A), 150-m scale (AIC= 323.67) (C), and 500-m scale (AIC= 321.36) (E), along with predicted abundances of this species in the Kirby grid from these respective models (B,D,F).

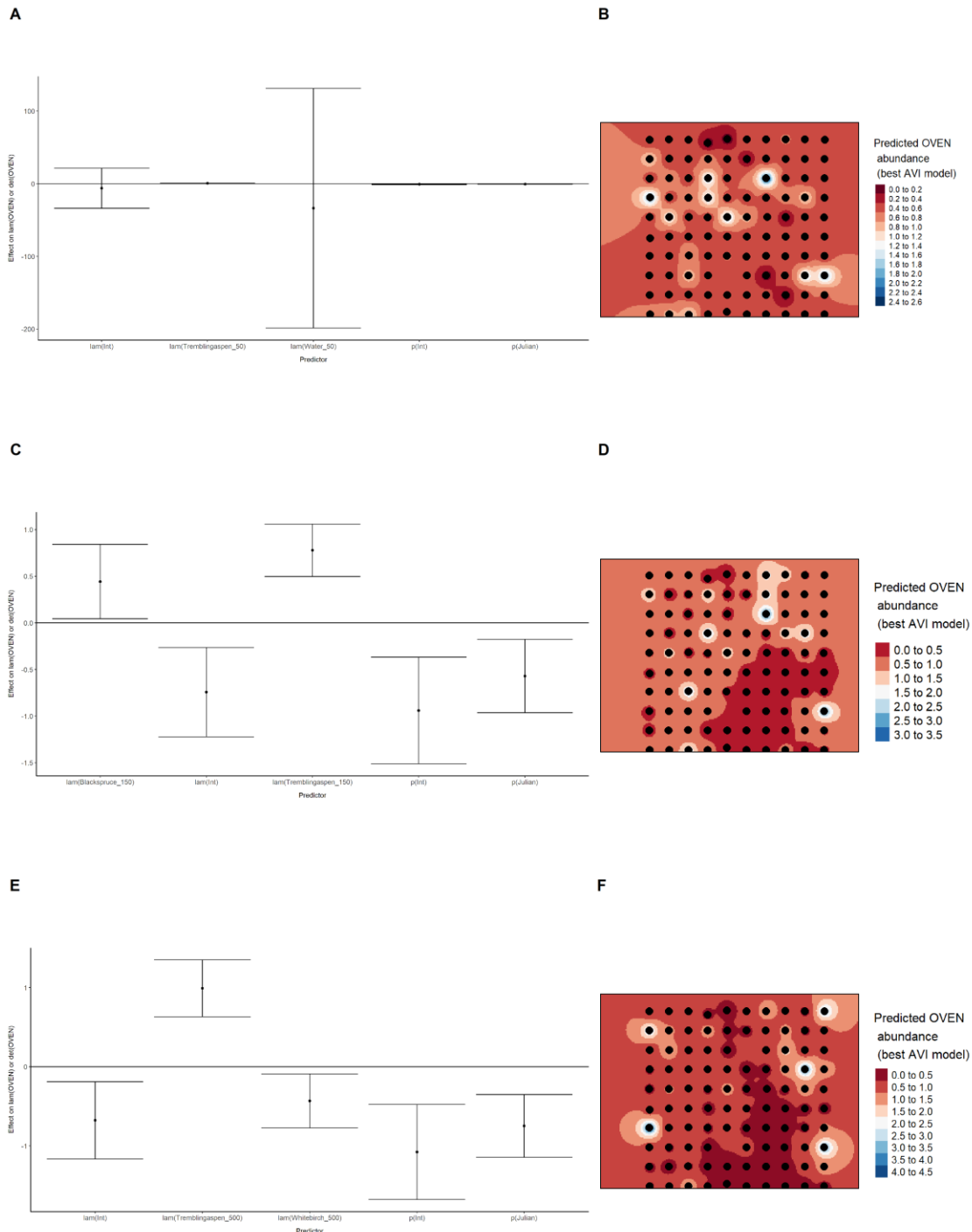


Figure 51. Model coefficients for the best *N*-mixture model predicting abundance of Ovenbird *Seiurus aurocapillus* from satellite-based data at the 50-m scale (AIC= 337.23) (A), 150-m scale

(AIC= 338.74) (C), and 500-m scale (AIC= 334.09) (E), along with predicted abundances of this species in the Kirby grid from these respective models (B,D,F).

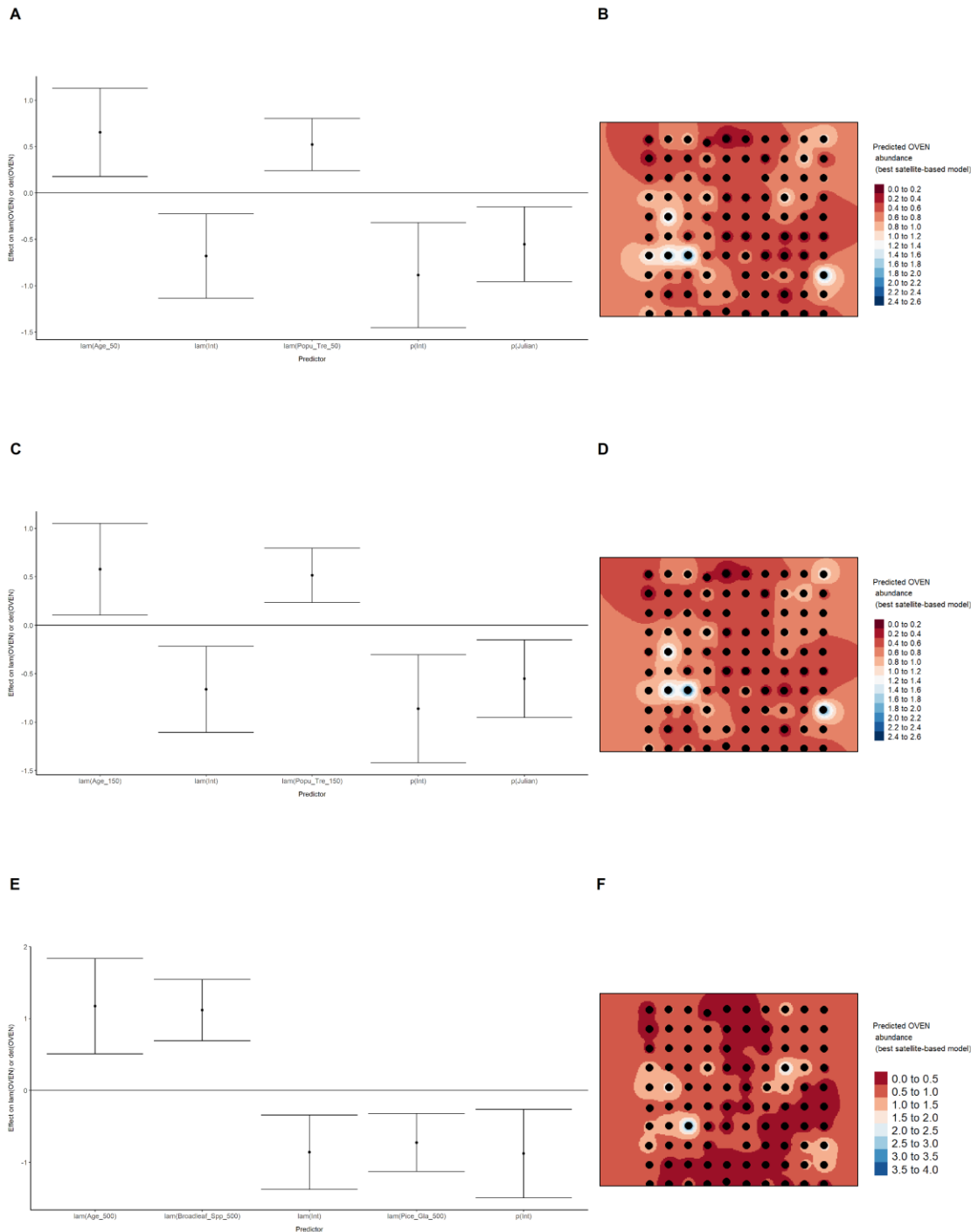
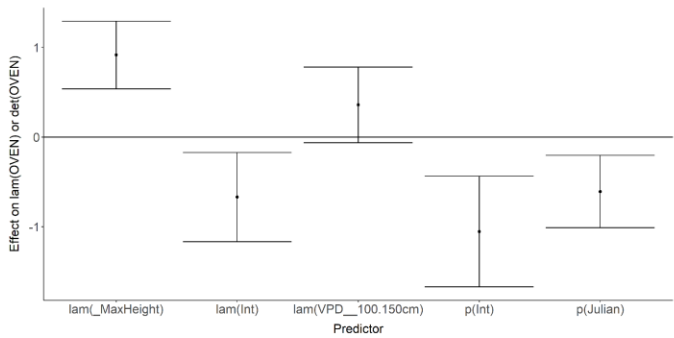


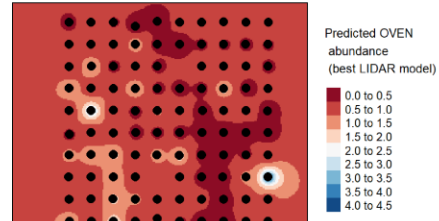
Figure 52. Model coefficients for the best N -mixture model predicting abundance of Ovenbird *Seiurus aurocapillus* from LIDAR-based data at the 150-m scale (AIC= 325.68) (A), and 500-m

scale ($AIC = 326.91$) (C), along with predicted abundances of this species in the Kirby grid from these respective models (B,D).

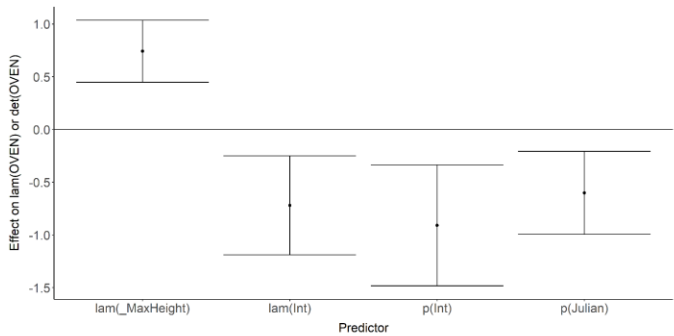
A



B



C



D

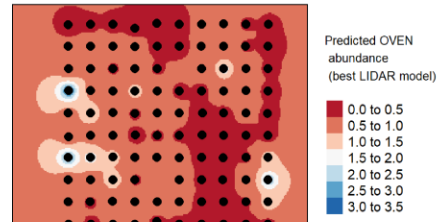


Figure 53. Model coefficients for the A) AVI-based ($AIC = 321.36$), C) satellite-based ($AIC = 334.09$), E) lidar-based ($AIC = 326.91$), and G) composite ($AIC = 321.36$) N -mixture models

predicting abundance of Ovenbird *Seiurus aurocapillus*, along with predicted abundances of this species in the Kirby grid from these respective models (B,D,F,H).

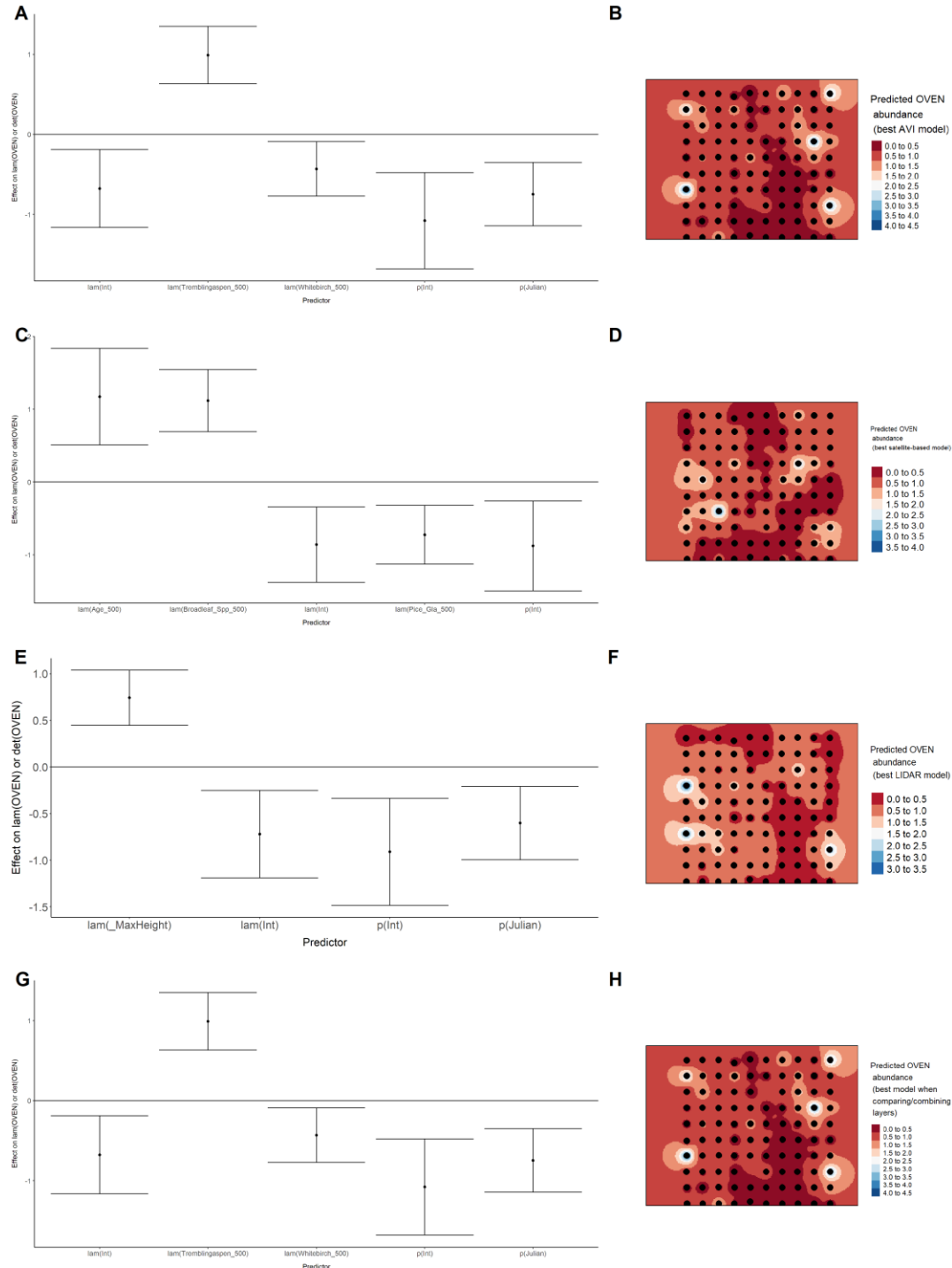


Figure 54. Model coefficients for the best *N*-mixture model predicting abundance of Palm Warbler *Setophaga palmarum* from Alberta Vegetation Inventory (AVI) shapefile-based data at the 50-m scale (AIC= 168.49) (A), 150-m scale (AIC= 153.98) (C), and 500-m scale (AIC= 164.2)

(E), along with predicted abundances of this species in the Kirby grid from these respective models (B,D,F).

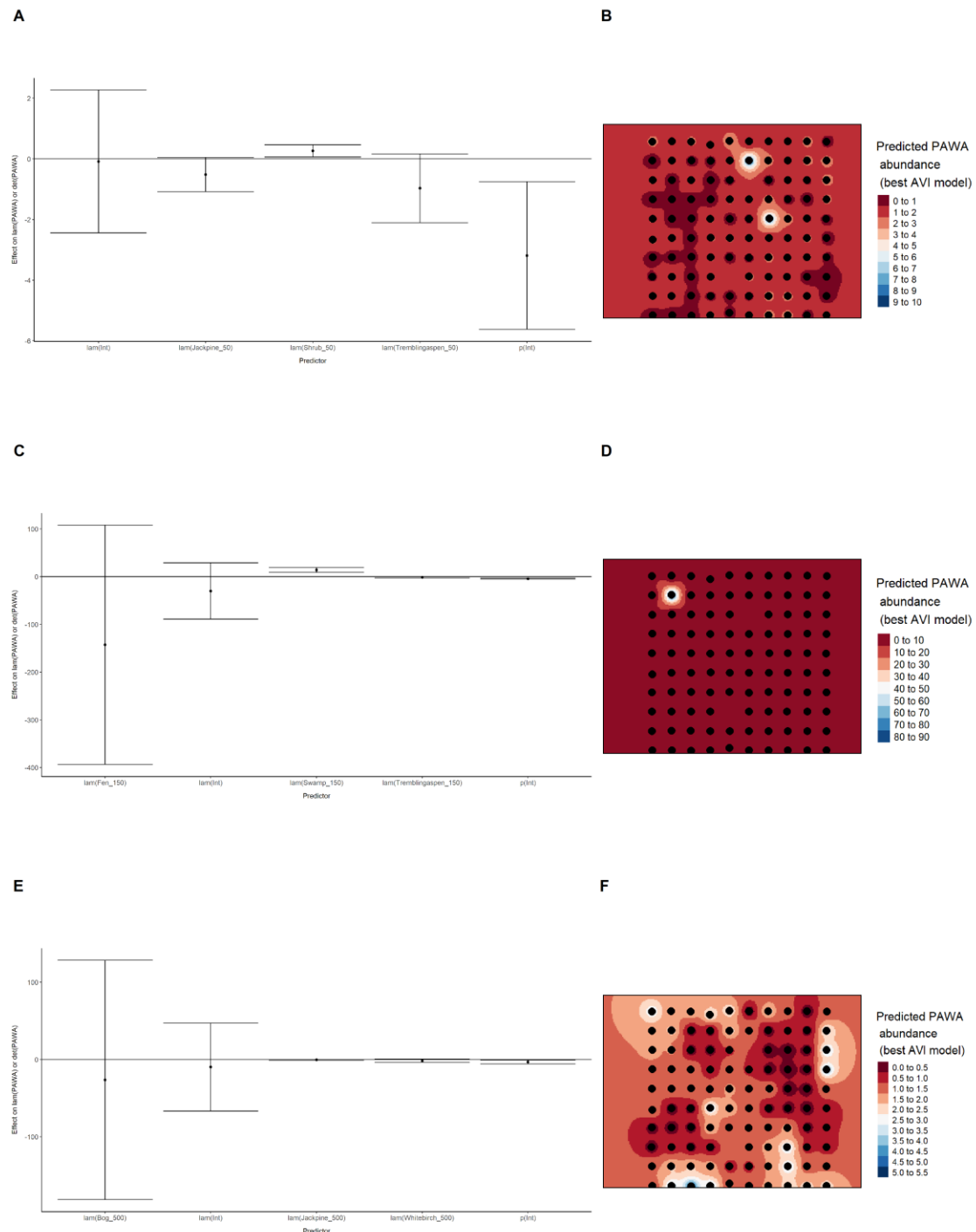


Figure 55. Model coefficients for the best N -mixture model predicting abundance of Palm Warbler *Setophaga palmarum* from satellite-based data at the 50-m scale (AIC= 166.13) (A),

150-m scale (AIC= 165.04) (C), and 500-m scale (AIC= 164.33) (E), along with predicted abundances of this species in the Kirby grid from these respective models (B,D,F).

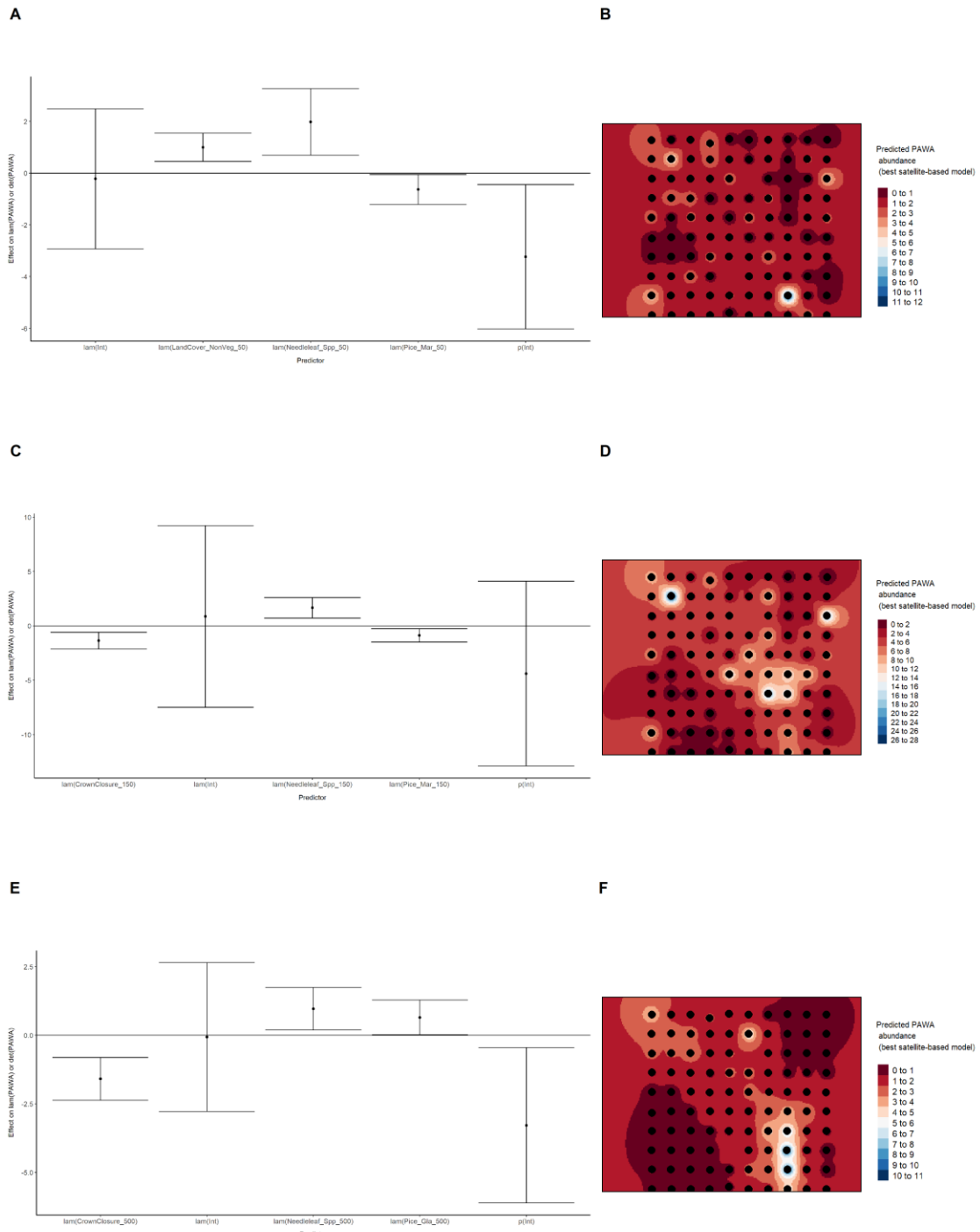
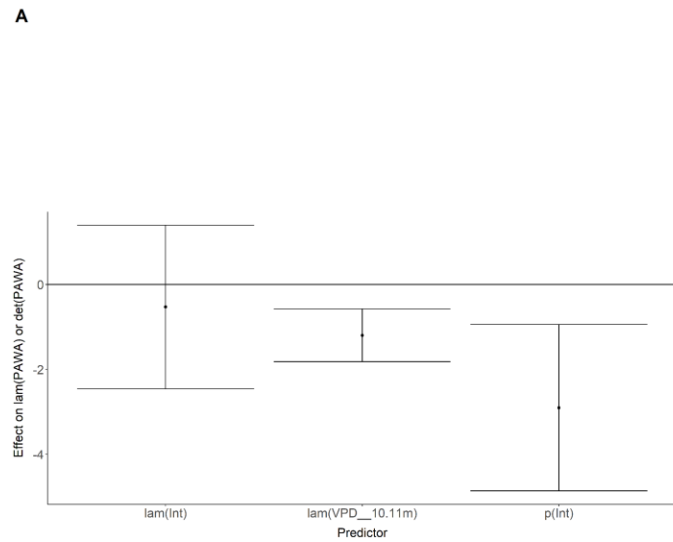


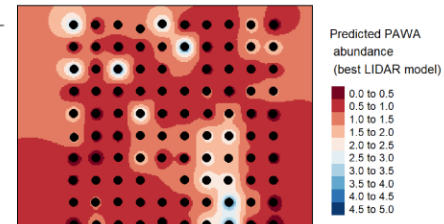
Figure 56. Model coefficients for the best N -mixture model predicting abundance of Palm Warbler *Setophaga palmarum* from LIDAR-based data at the 150-m scale (AIC= 159.23) (A), and

500-m scale (AIC= 156.91) (C), along with predicted abundances of this species in the Kirby grid from these respective models (B,D).

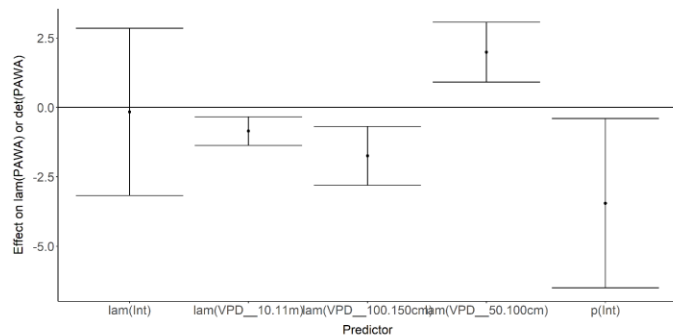
A



B



C



D

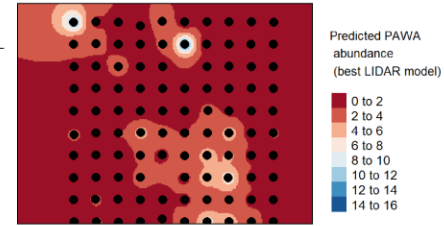


Figure 57. Model coefficients for the A) AVI-based (AIC= 153.98), C) satellite-based (AIC= 164.33), E) lidar-based (AIC= 156.91), and G) composite (AIC= 151.97) N-mixture models

predicting abundance of Palm Warbler *Setophaga palmarum*, along with predicted abundances of this species in the Kirby grid from these respective models (B,D,F,H).

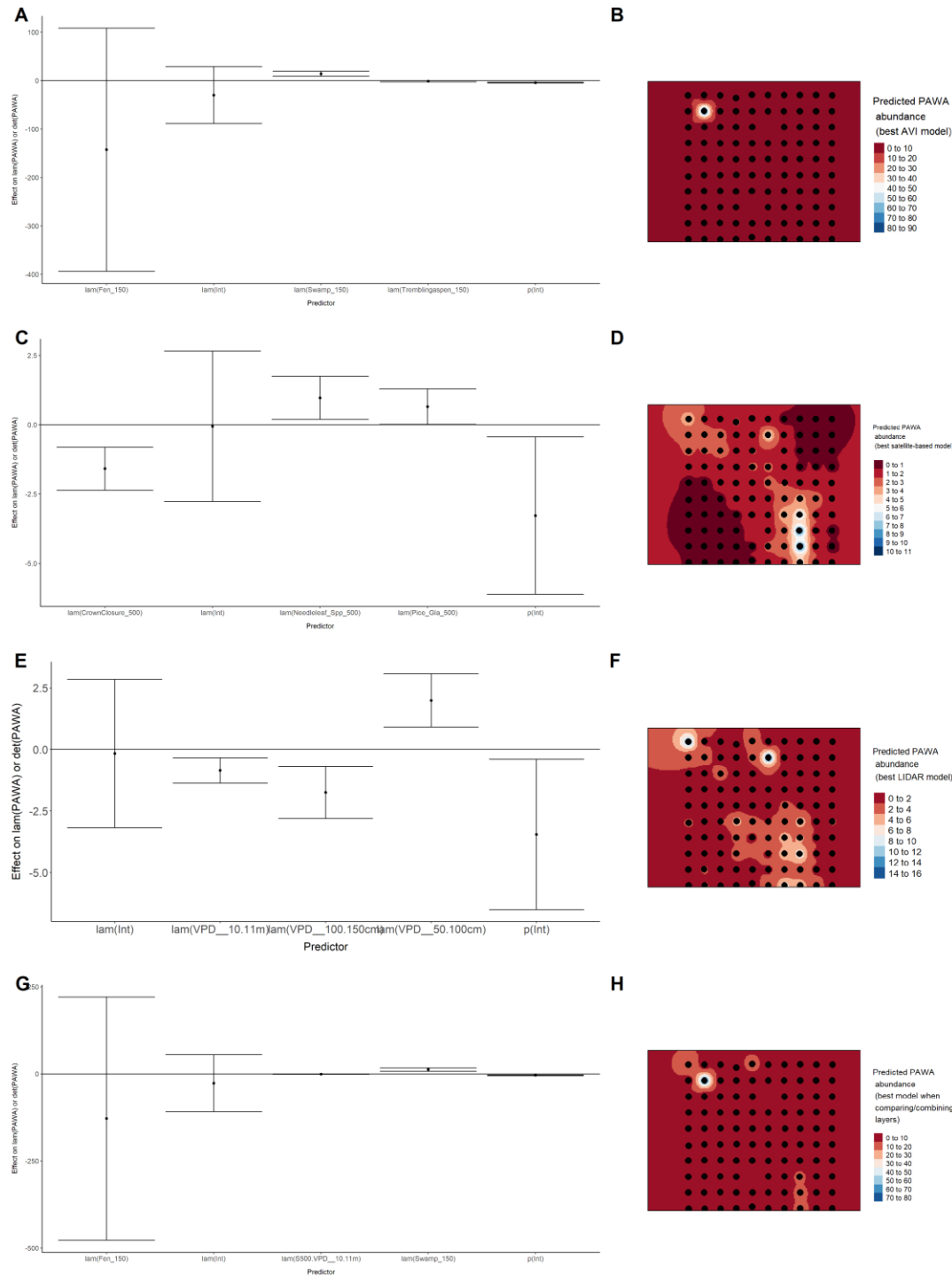


Figure 58. Model coefficients for the best *N*-mixture model predicting abundance of Red-eyed Vireo *Vireo olivaceus* from Alberta Vegetation Inventory (AVI) shapefile-based data at the 50-m

scale (AIC= 289.88) (A), 150-m scale (AIC= 282.5) (C), and 500-m scale (AIC= 265.41) (E), along with predicted abundances of this species in the Kirby grid from these respective models (B,D,F).

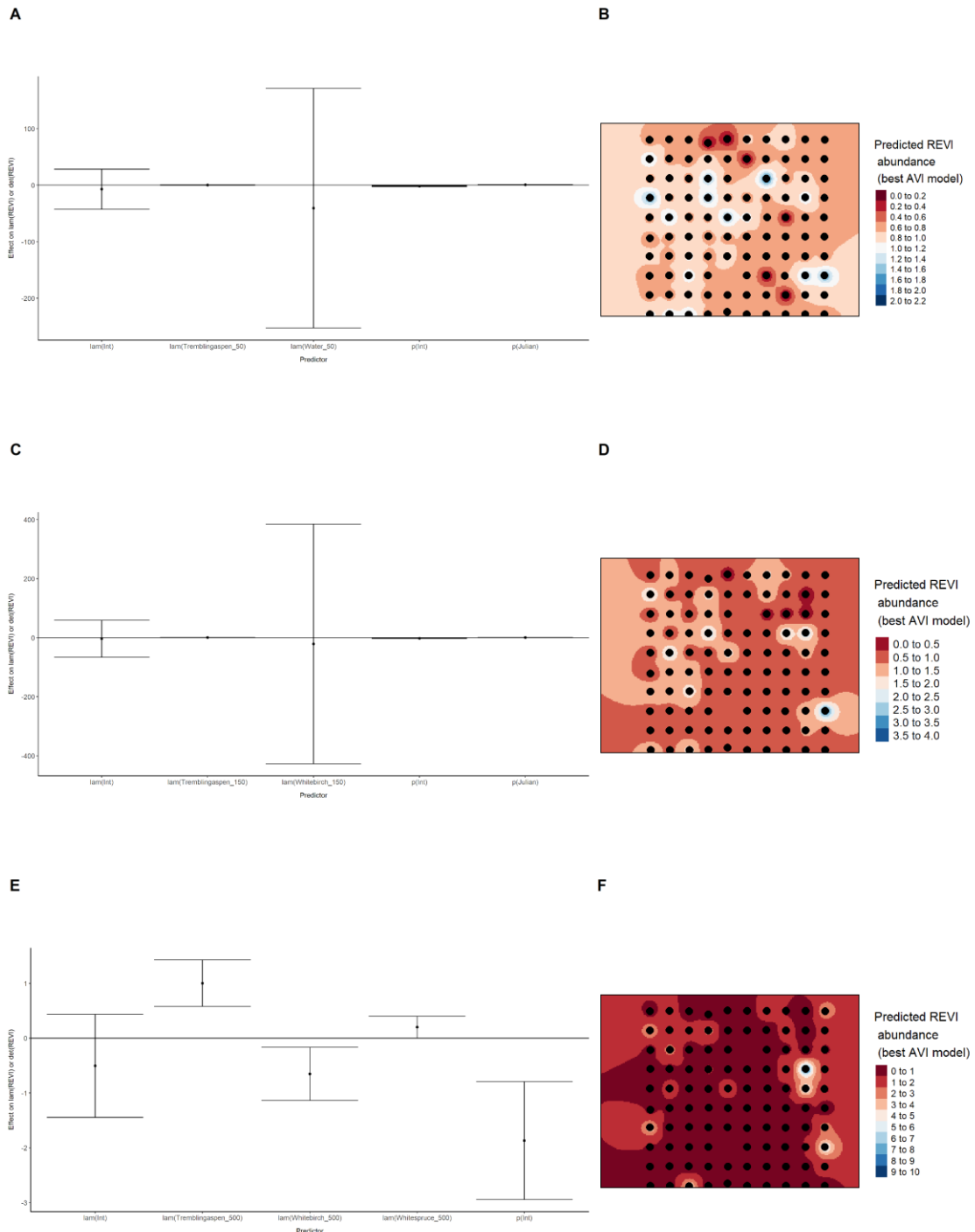


Figure 59. Model coefficients for the best N -mixture model predicting abundance of Red-eyed Vireo *Vireo olivaceus* from satellite-based data at the 50-m scale (AIC= 286.47) (A), 150-m scale

(AIC= 286.96) (C), and 500-m scale (AIC= 280.83) (E), along with predicted abundances of this species in the Kirby grid from these respective models (B,D,F).

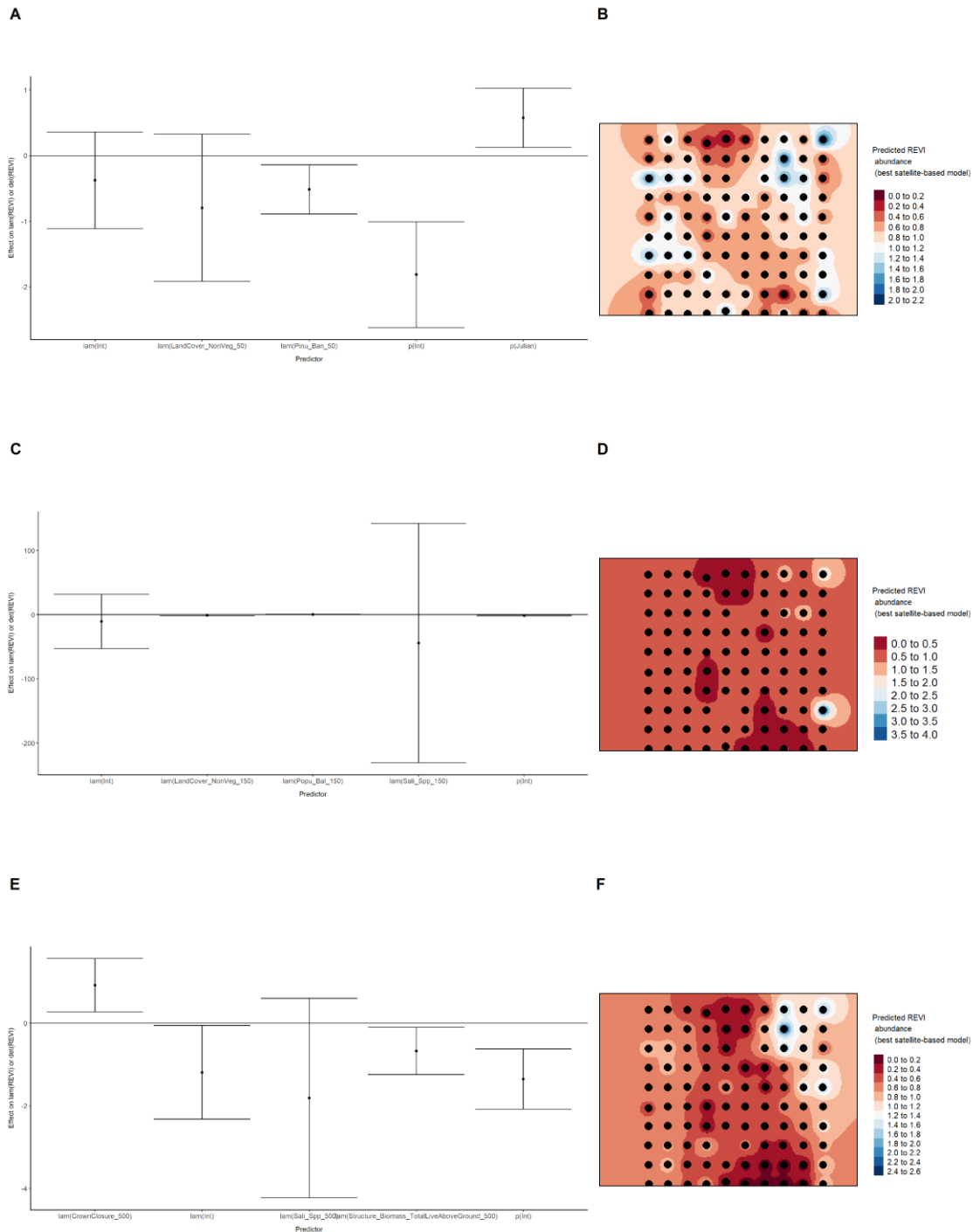


Figure 60. Model coefficients for the best N -mixture model predicting abundance of Red-eyed Vireo *Vireo olivaceus* from LIDAR-based data at the 150-m scale (AIC= 293.08) (A), and 500-m

scale (AIC= 286.33) (C), along with predicted abundances of this species in the Kirby grid from these respective models (B,D).

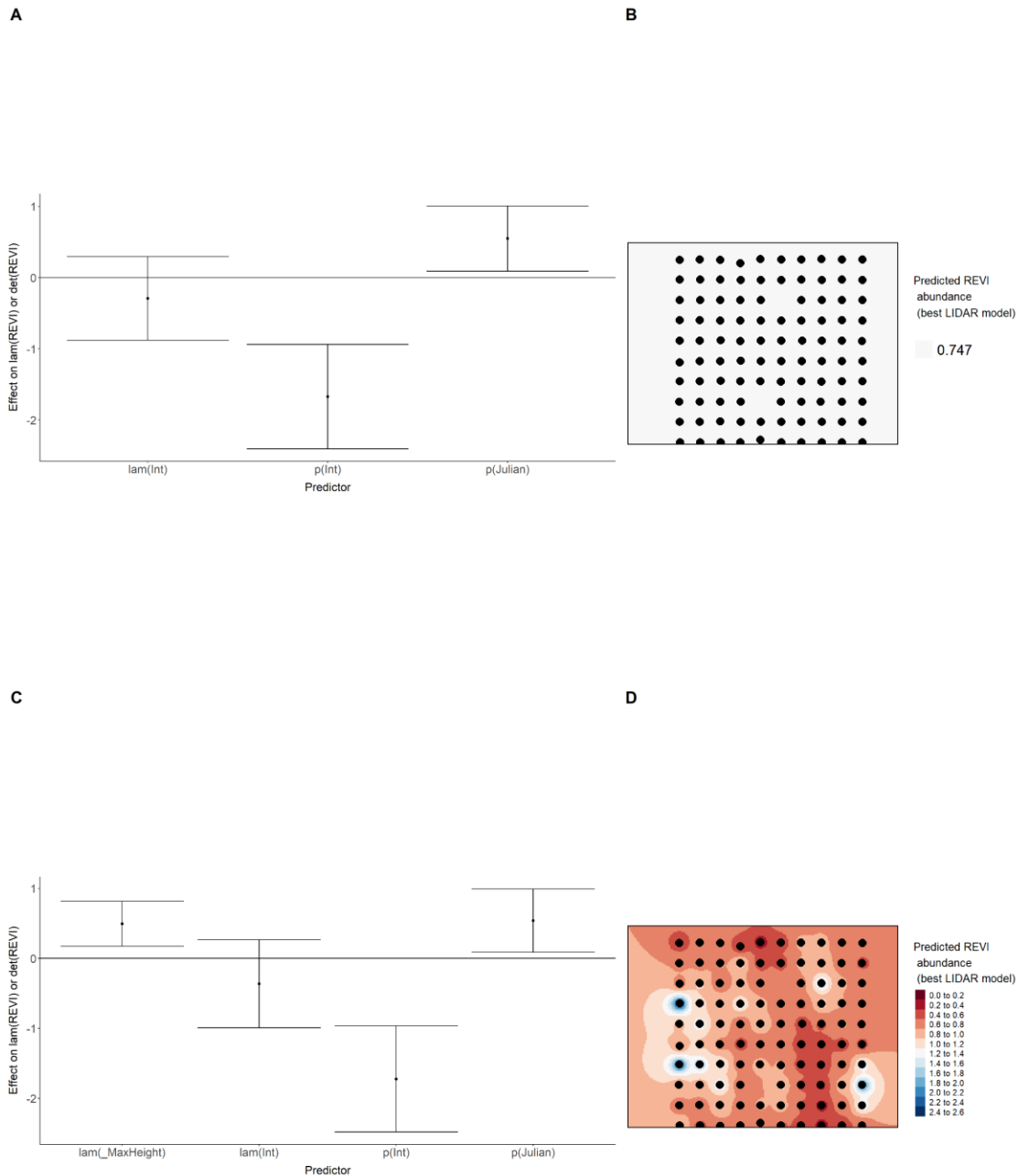


Figure 61. Model coefficients for the A) AVI-based (AIC= 265.41), C) satellite-based (AIC= 280.83), E) lidar-based (AIC= 286.33), and G) composite (AIC= 263.87) N-mixture models

predicting abundance of Red-eyed Vireo *Vireo olivaceus*, along with predicted abundances of this species in the Kirby grid from these respective models (B,D,F,H).

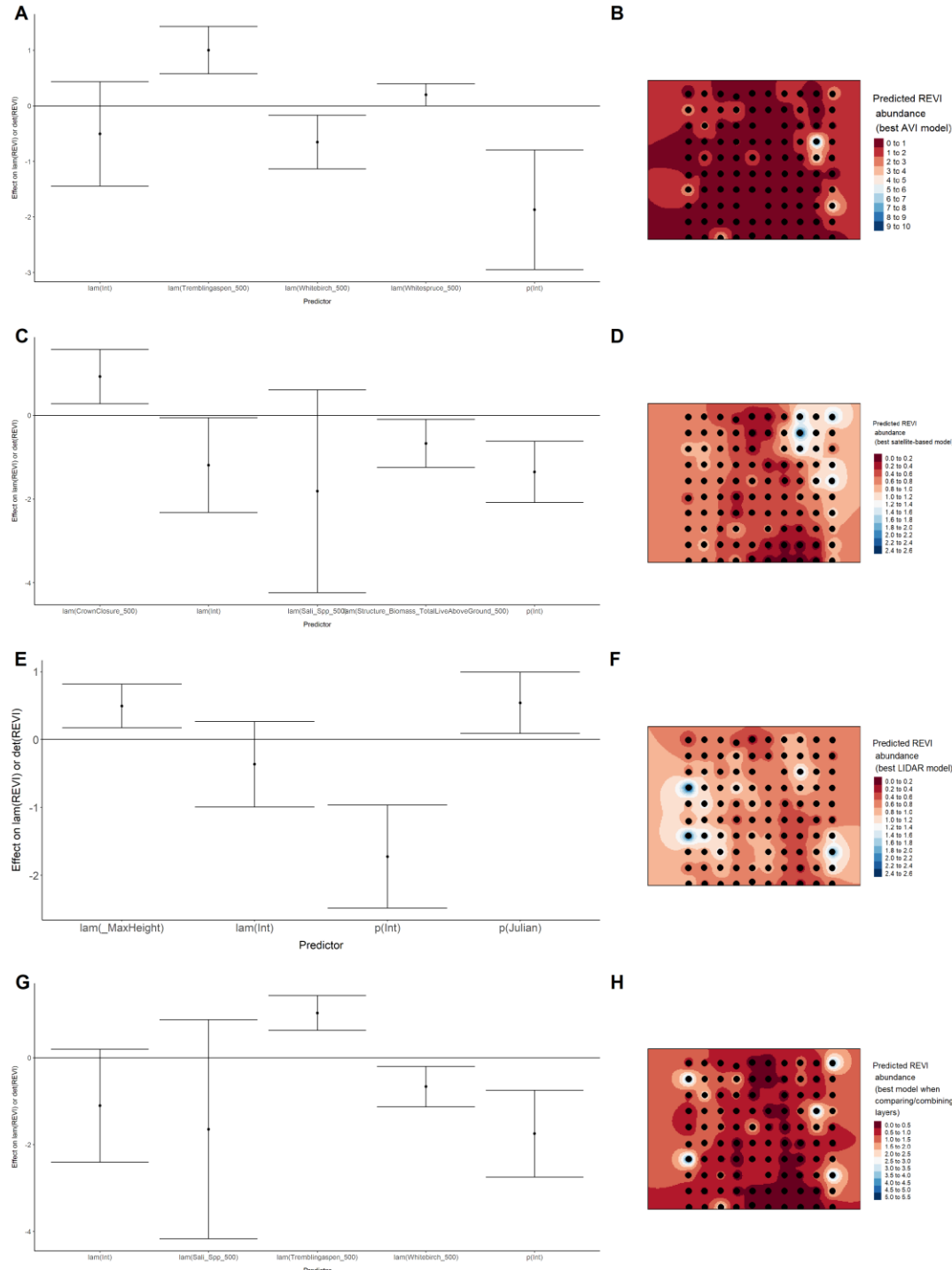


Figure 62. Model coefficients for the best *N*-mixture model predicting abundance of Ruby-crowned Kinglet *Regulus calendula* from Alberta Vegetation Inventory (AVI) shapefile-based data at the 50-m scale (AIC= 361.96) (A), 150-m scale (AIC= 361.85) (C), and 500-m scale (AIC=

364.5) (E), along with predicted abundances of this species in the Kirby grid from these respective models (B,D,F).

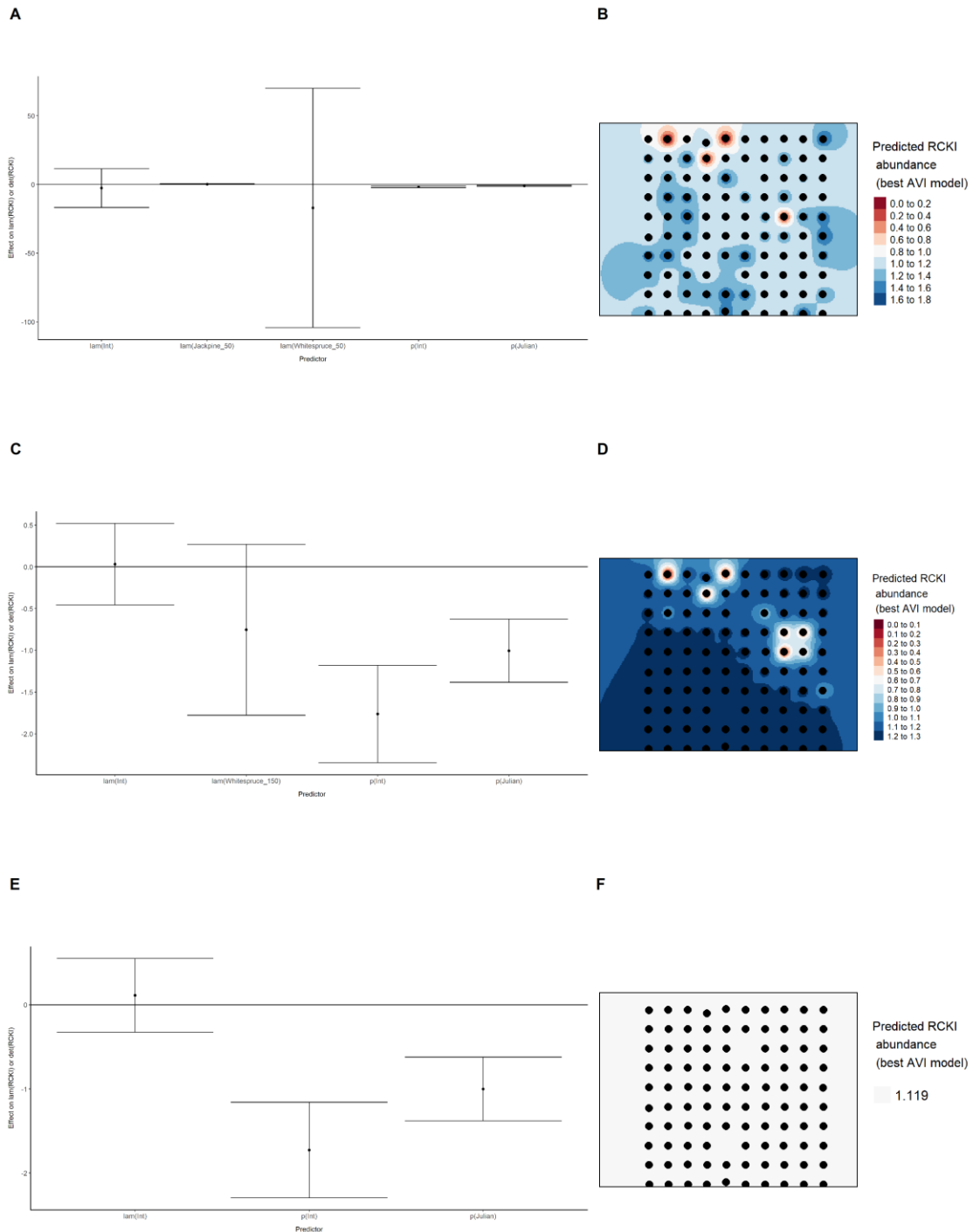


Figure 63. Model coefficients for the best N -mixture model predicting abundance of Ruby-crowned Kinglet *Regulus calendula* from satellite-based data at the 50-m scale (AIC= 362.17) (A),

150-m scale (AIC= 362.83) (C), and 500-m scale (AIC= 357.62) (E), along with predicted abundances of this species in the Kirby grid from these respective models (B,D,F).

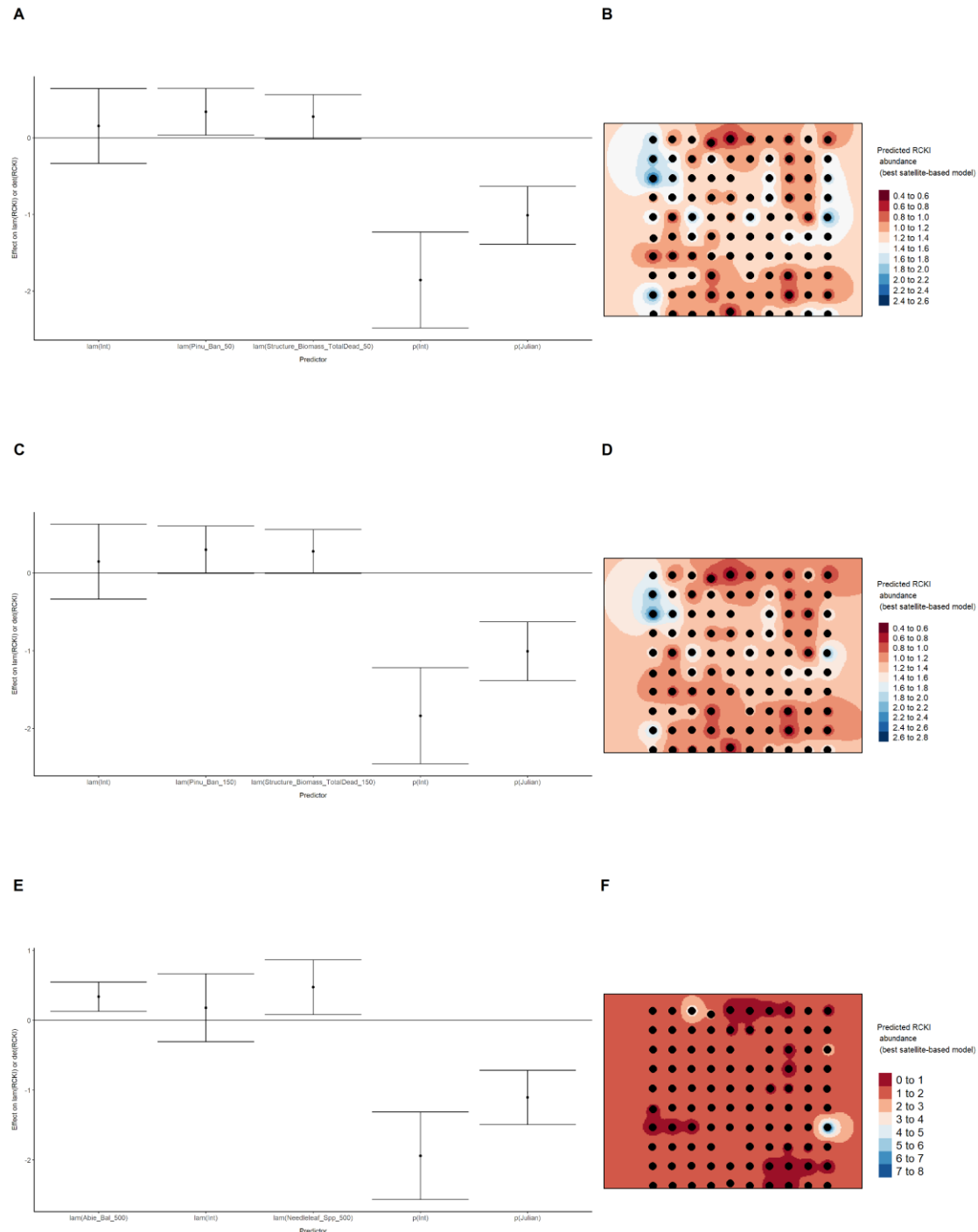
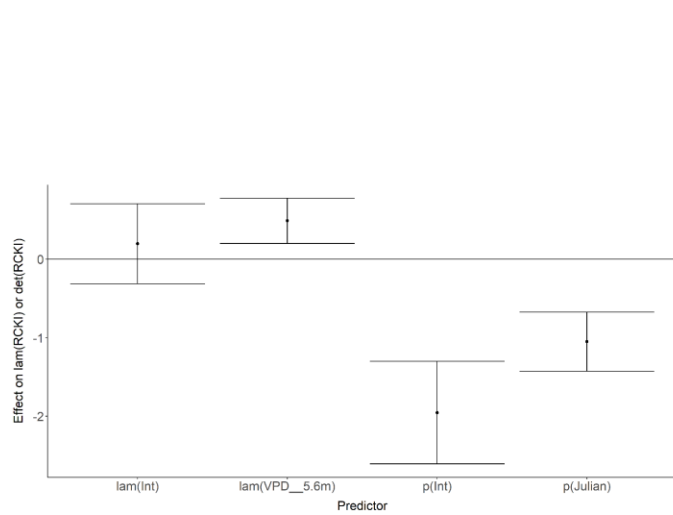


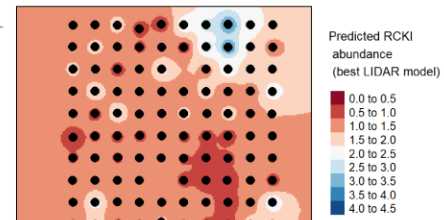
Figure 64. Model coefficients for the best N -mixture model predicting abundance of Ruby-crowned Kinglet *Regulus calendula* from LIDAR-based data at the 150-m scale (AIC= 355.53) (A),

and 500-m scale ($AIC = 357.95$) (C), along with predicted abundances of this species in the Kirby grid from these respective models (B,D).

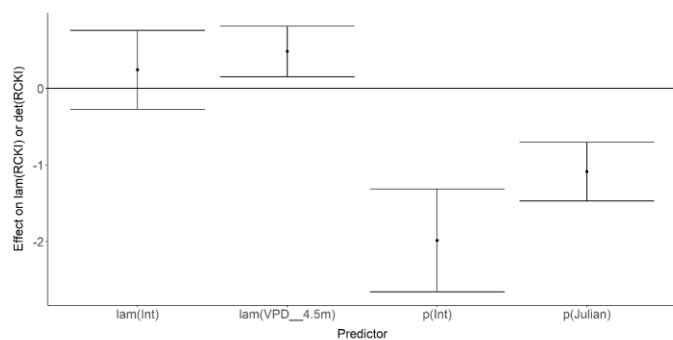
A



B



C



D

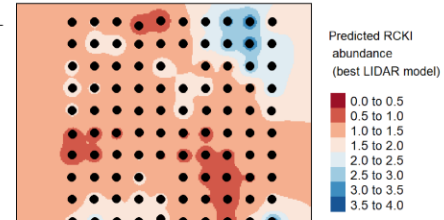


Figure 65. Model coefficients for the A) AVI-based ($AIC = 361.85$), C) satellite-based ($AIC = 357.62$), E) lidar-based ($AIC = 355.53$), and G) composite ($AIC = 353.02$) N -mixture models

predicting abundance of Ruby-crowned Kinglet *Regulus calendula*, along with predicted abundances of this species in the Kirby grid from these respective models (B,D,F,H).

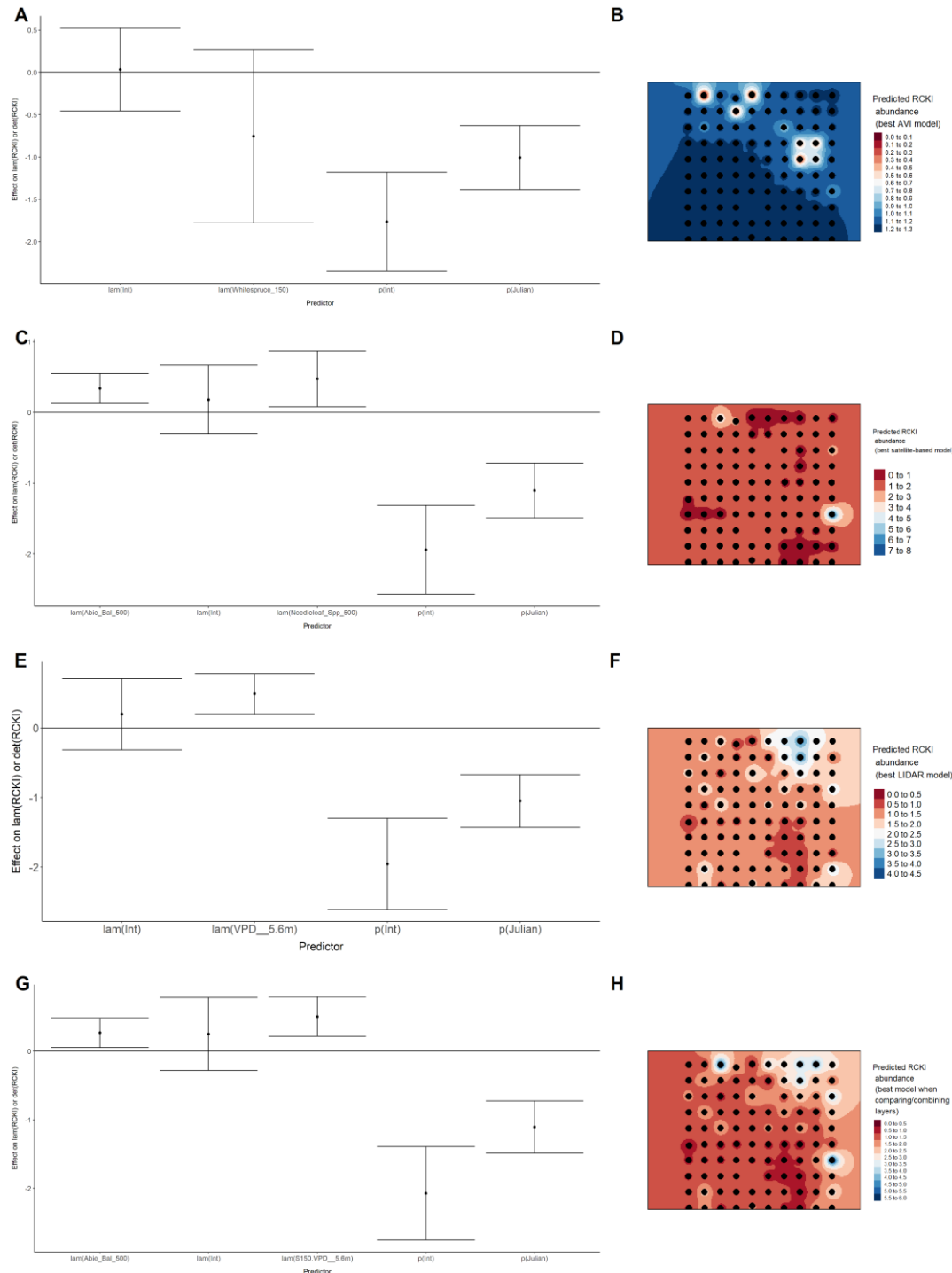


Figure 66. Model coefficients for the best *N*-mixture model predicting abundance of Swainson's Thrush *Catharus ustulatus* from Alberta Vegetation Inventory (AVI) shapefile-based data at the 50-m scale (AIC= 665.01) (A), 150-m scale (AIC= 665.64) (C), and 500-m scale (AIC= 664.61) (E),

along with predicted abundances of this species in the Kirby grid from these respective models (B,D,F).

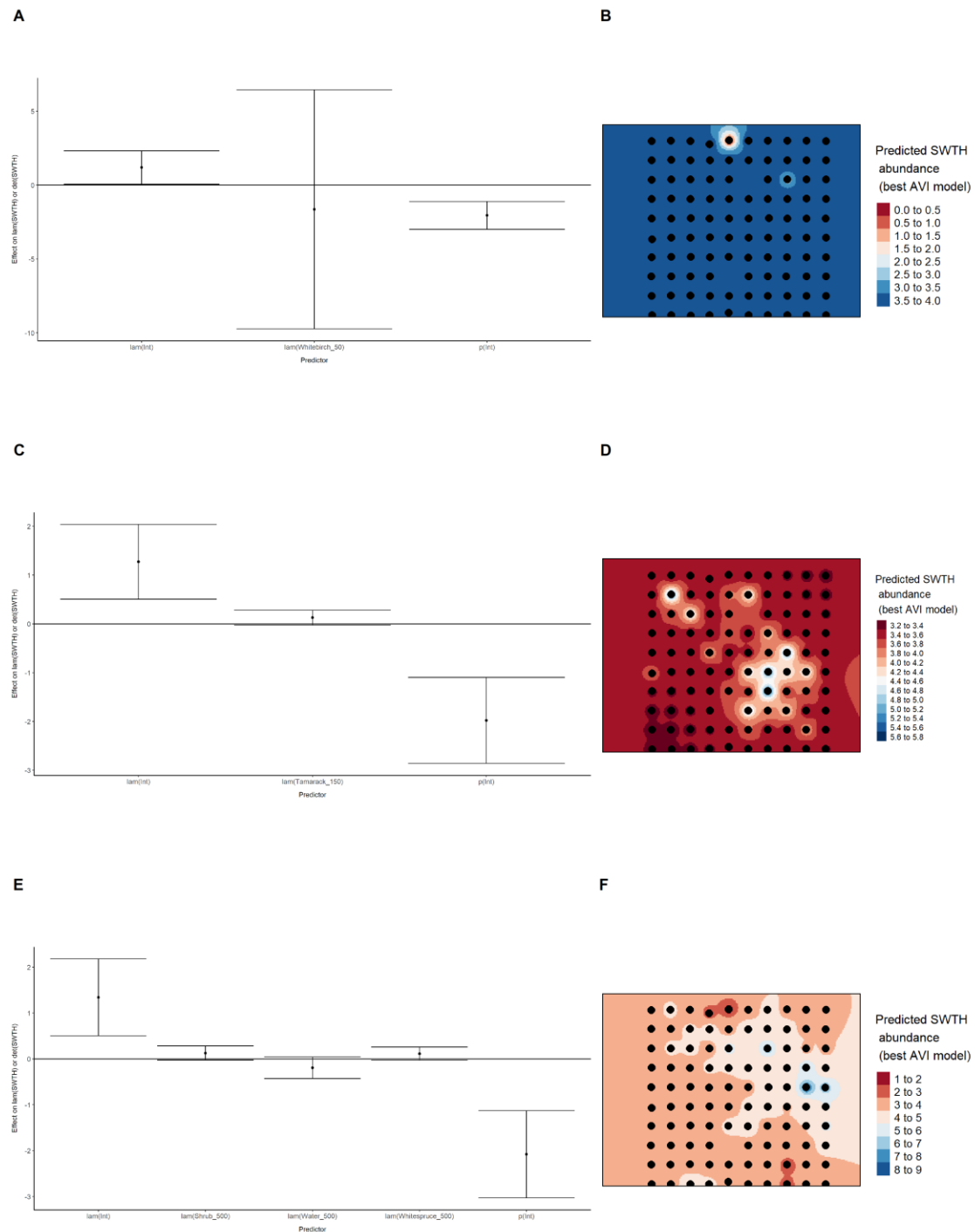


Figure 67. Model coefficients for the best *N*-mixture model predicting abundance of Swainson's Thrush *Catharus ustulatus* from satellite-based data at the 50-m scale (AIC= 656.31) (A), 150-m

scale (AIC= 654.1) (C), and 500-m scale (AIC= 657.54) (E), along with predicted abundances of this species in the Kirby grid from these respective models (B,D,F).

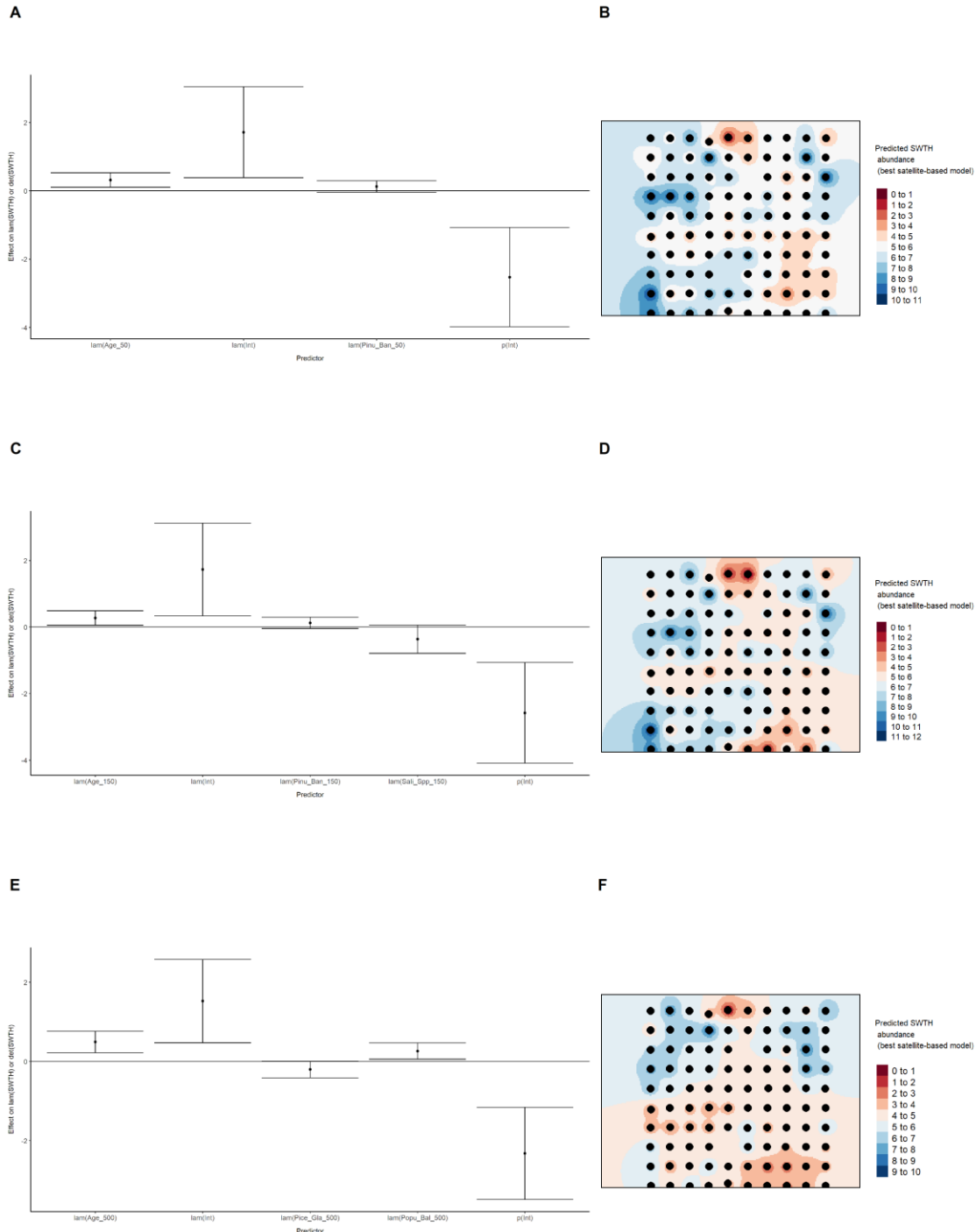


Figure 68. Model coefficients for the best N -mixture model predicting abundance of Swainson's Thrush *Catharus ustulatus* from LIDAR-based data at the 150-m scale (AIC= 665.47) (A), and 500-

m scale (AIC= 660.96) (C), along with predicted abundances of this species in the Kirby grid from these respective models (B,D).

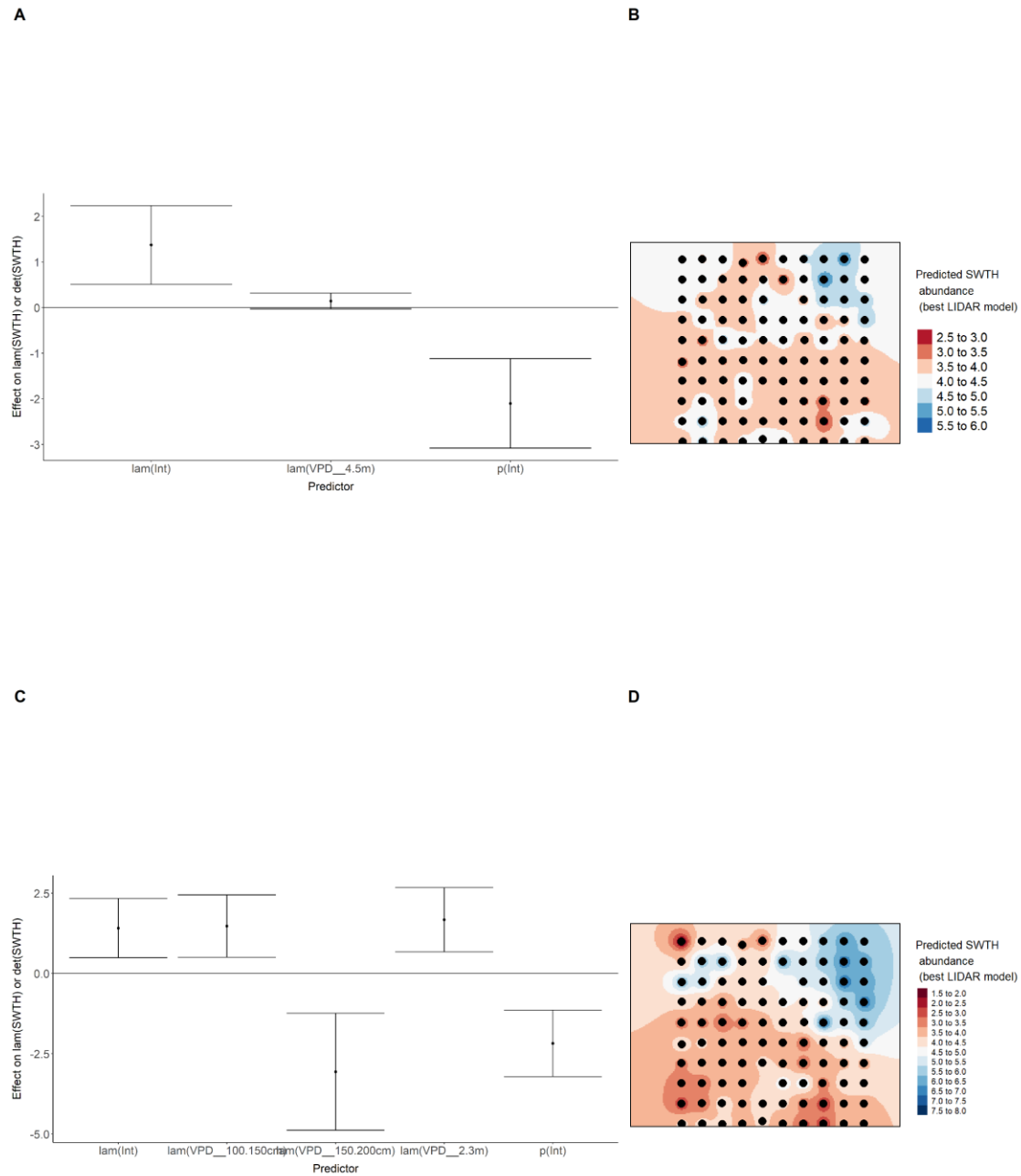


Figure 69. Model coefficients for the A) AVI-based (AIC= 664.61), C) satellite-based (AIC= 657.54), E) lidar-based (AIC= 660.96), and G) composite (AIC= 660.45) N -mixture models

predicting abundance of Swainson's Thrush *Catharus ustulatus*, along with predicted abundances of this species in the Kirby grid from these respective models (B,D,F,H).

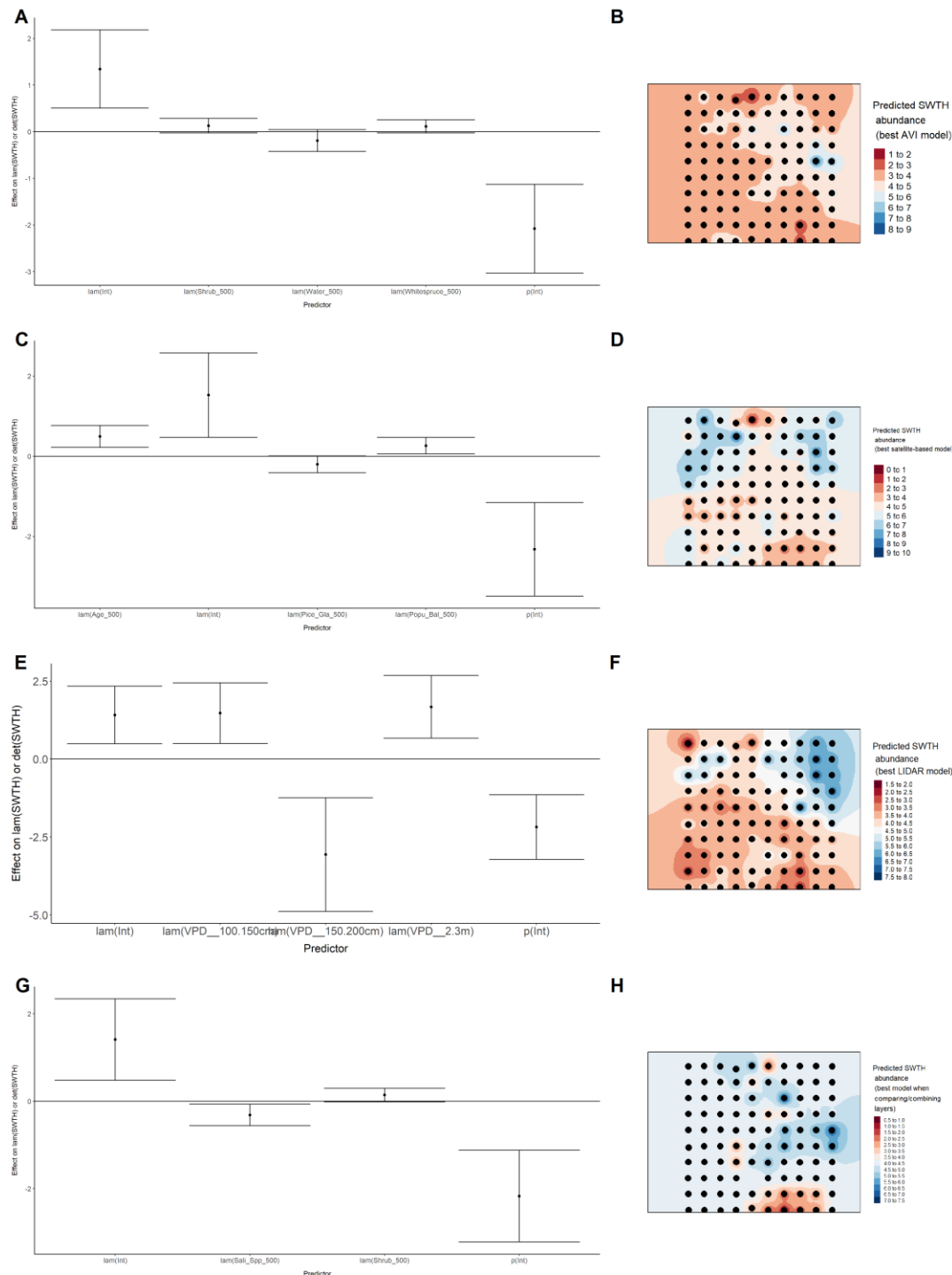


Figure 70. Model coefficients for the best *N*-mixture model predicting abundance of Swamp Sparrow *Melospiza georgiana* from Alberta Vegetation Inventory (AVI) shapefile-based data at the 50-m scale (AIC= 134.8) (A), 150-m scale (AIC= 127.82) (C), and 500-m scale (AIC= 130.72)

(E), along with predicted abundances of this species in the Kirby grid from these respective models (B,D,F).

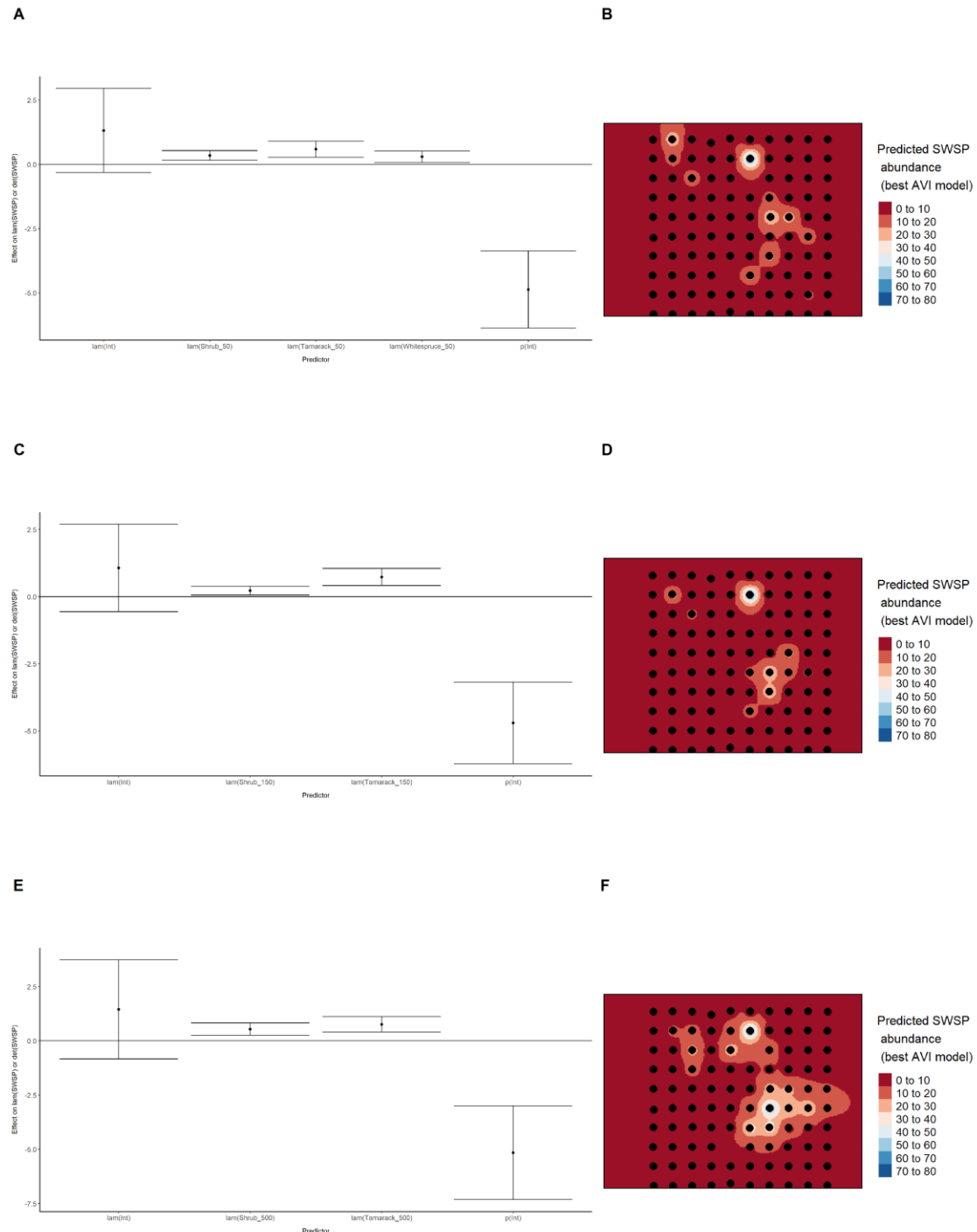


Figure 71. Model coefficients for the best N -mixture model predicting abundance of Swamp Sparrow *Melospiza georgiana* from satellite-based data at the 50-m scale ($\text{AIC}=143.31$) (A), 150-m scale ($\text{AIC}=139.33$) (C), and 500-m scale ($\text{AIC}=139.77$) (E), along

with predicted abundances of this species in the Kirby grid from these respective models (B,D,F).

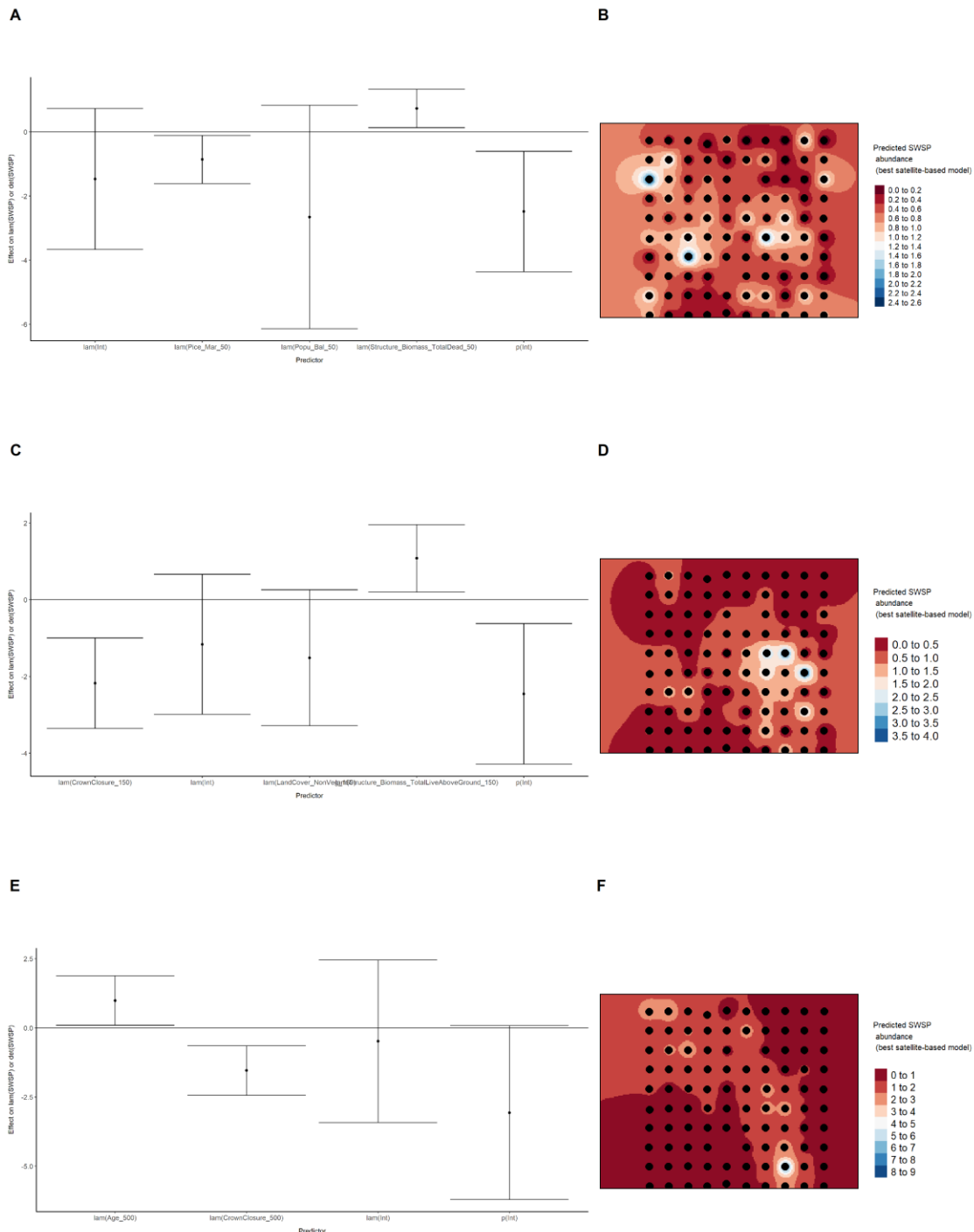
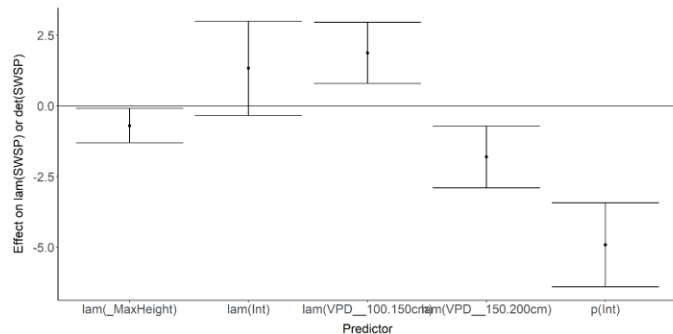


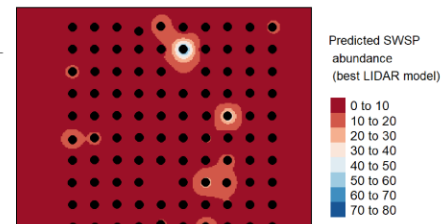
Figure 72. Model coefficients for the best *N*-mixture model predicting abundance of Swamp Sparrow *Melospiza georgiana* from LIDAR-based data at the 150-m scale (AIC= 138.15) (A), 500-

m scale (AIC= 143.69) (C), along with predicted abundances of this species in the Kirby grid from these respective models (B,D).

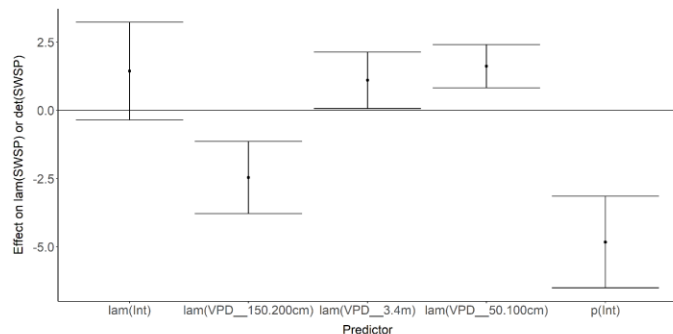
A



B



C



D

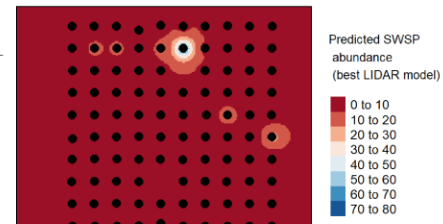


Figure 73. Model coefficients for the A) AVI-based (AIC= 127.82), C) satellite-based (AIC= 139.33), E) lidar-based (AIC= 138.15), and G) composite (AIC= 127.2) N-mixture models

predicting abundance of Swamp Sparrow *Melospiza georgiana*, along with predicted abundances of this species in the Kirby grid from these respective models (B,D,F,H).

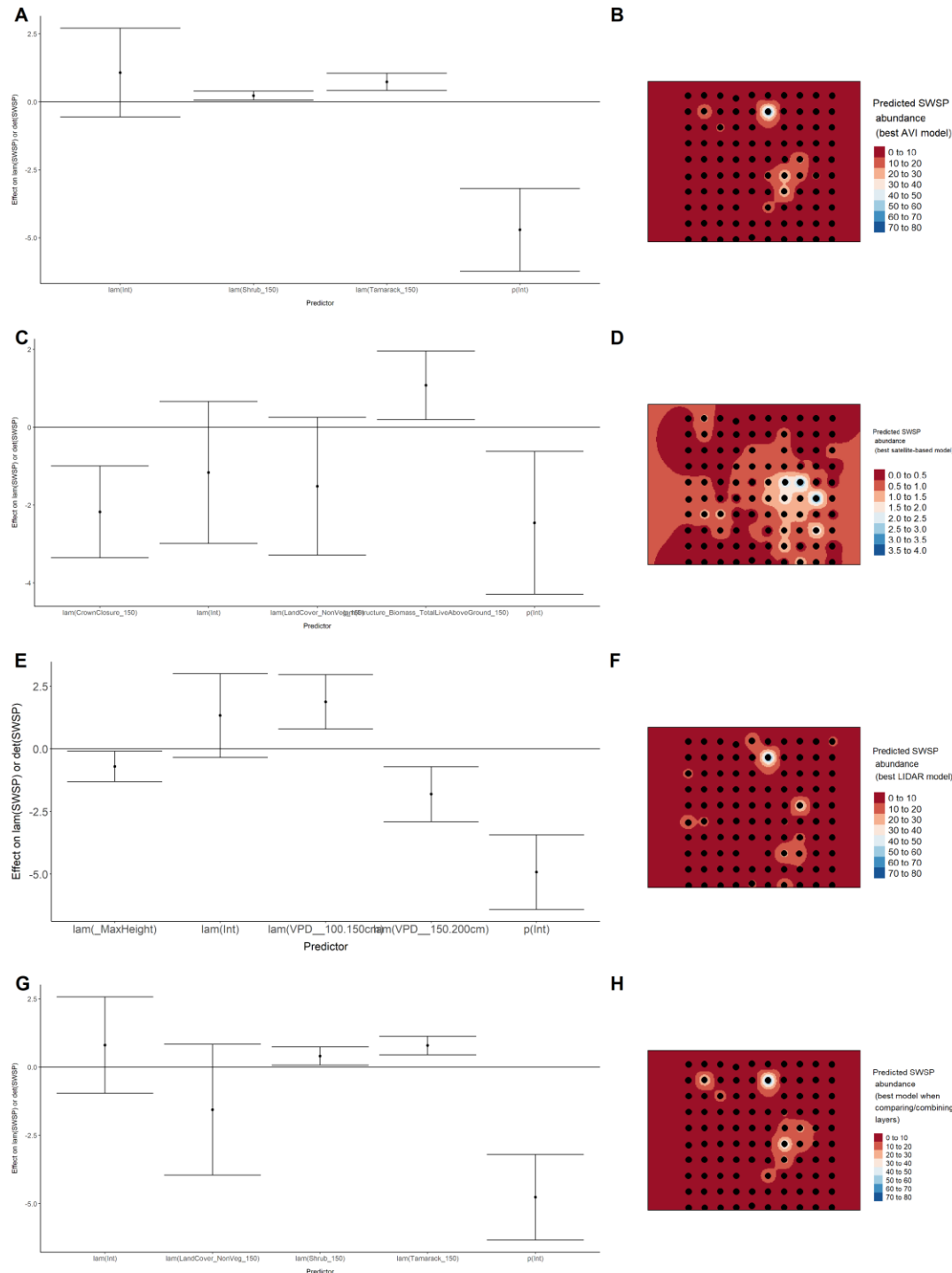


Figure 74. Model coefficients for the best *N*-mixture model predicting abundance of Tennessee Warbler *Leiothlypis peregrina* from Alberta Vegetation Inventory (AVI) shapefile-based data at the 50-m scale (AIC= 326.99) (A), 150-m scale (AIC= 326.27) (C), and 500-m scale (AIC= 317.57)

(E), along with predicted abundances of this species in the Kirby grid from these respective models (B,D,F).

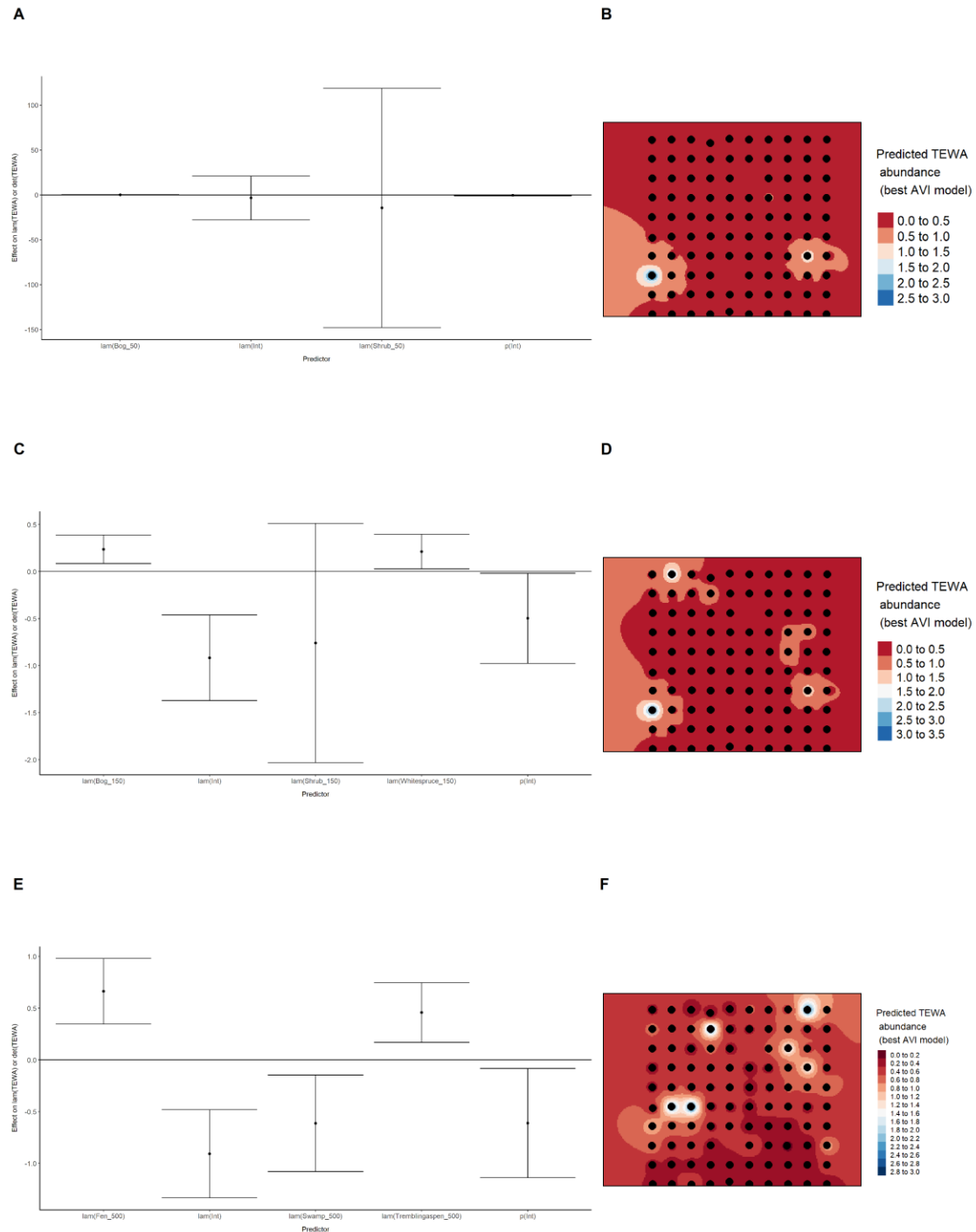
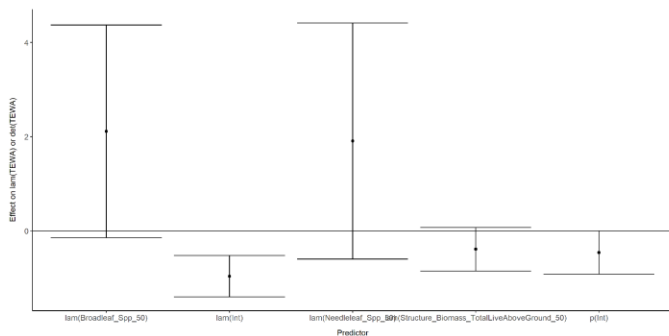


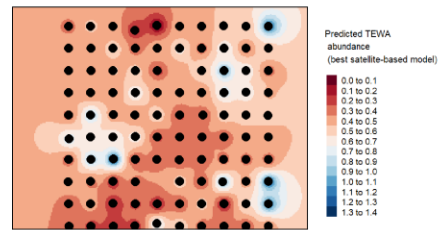
Figure 75. Model coefficients for the best N -mixture model predicting abundance of Tennessee Warbler *Leiothlypis peregrina* from satellite-based data at the 50-m scale

(AIC= 327.76) (A), 150-m scale (AIC= 326.37) (C), and 500-m scale (AIC= 322.11) (E), along with predicted abundances of this species in the Kirby grid from these respective models (B,D,F).

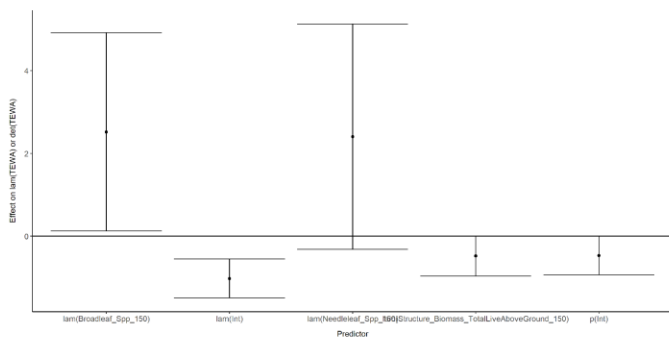
A



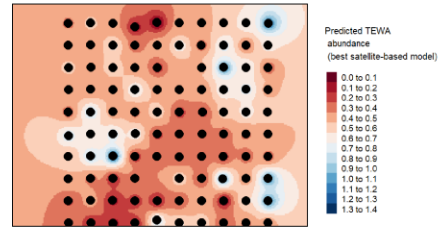
B



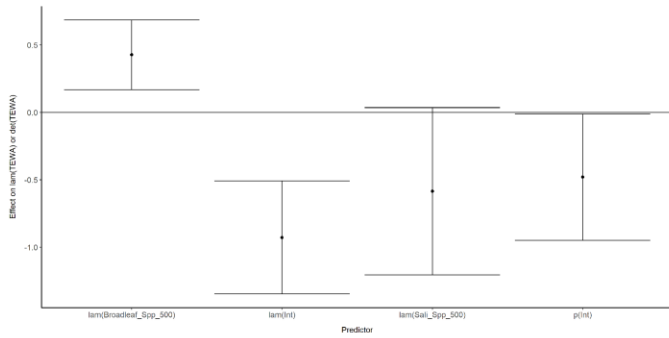
C



D



E



F

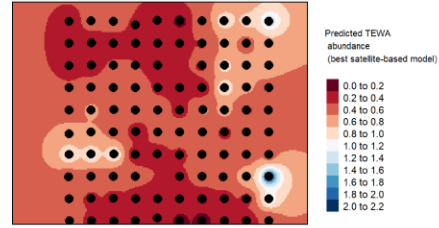
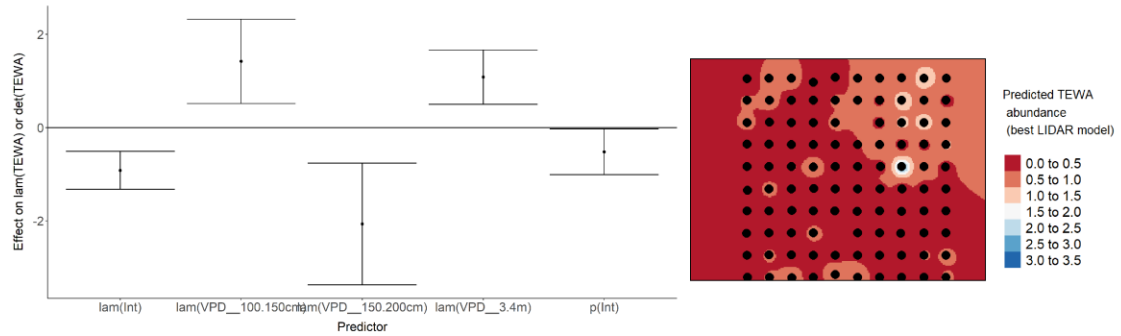
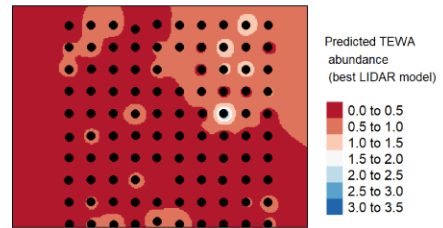


Figure 76. Model coefficients for the best N -mixture model predicting abundance of Tennessee Warbler *Leiothlypis peregrina* from LIDAR-based data at the 150-m scale (AIC= 322.38) (A), and 500-m scale (AIC= 328.8) (C), along with predicted abundances of this species in the Kirby grid from these respective models (B,D).

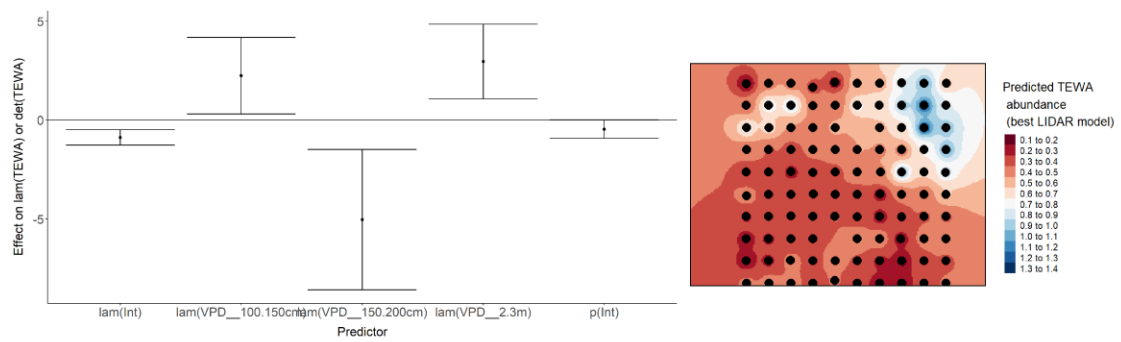
A



B



C



D

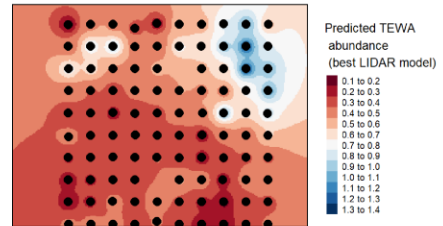


Figure 77. Model coefficients for the A) AVI-based (AIC= 317.57), C) satellite-based (AIC= 322.11), E) lidar-based (AIC= 322.38), and G) composite (AIC= 317.02) *N*-mixture models predicting abundance of Tennessee Warbler *Leiothlypis peregrina*, along with predicted abundances of this species in the Kirby grid from these respective models (B,D,F,H).

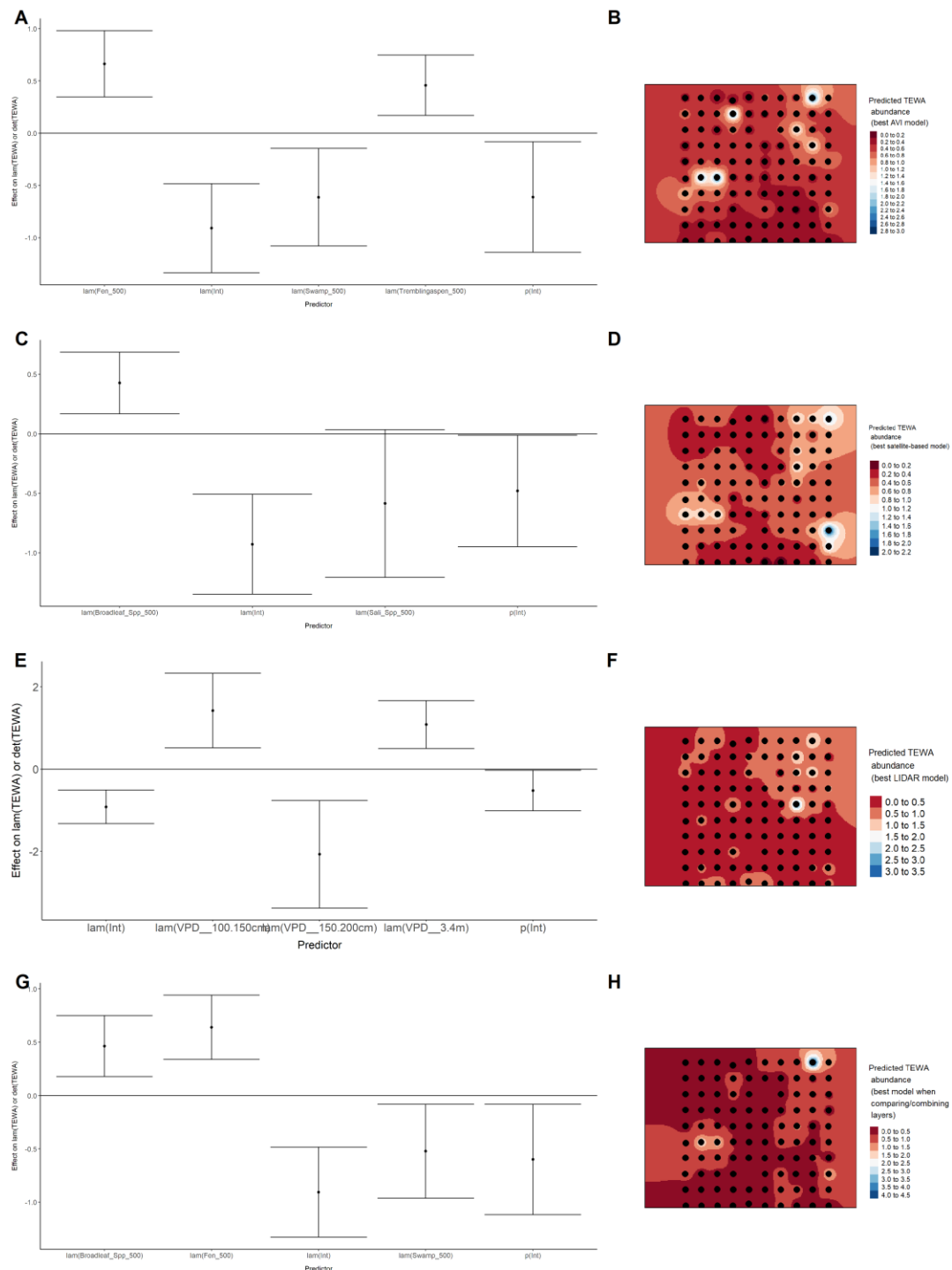
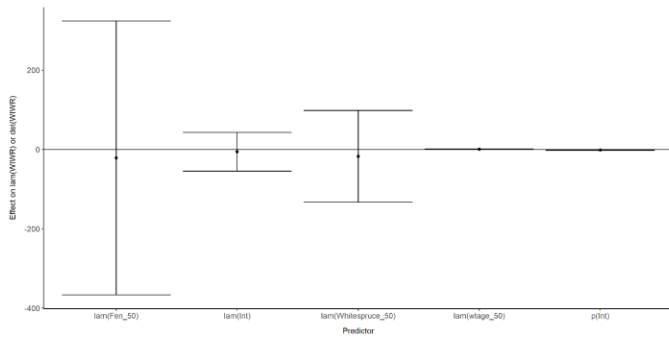


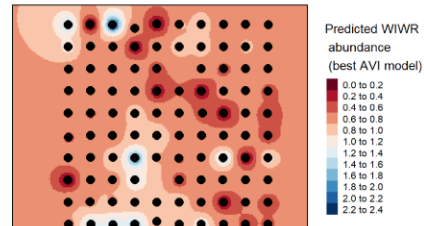
Figure 78. Model coefficients for the best *N*-mixture model predicting abundance of Winter Wren *Troglodytes hiemalis* from Alberta Vegetation Inventory (AVI) shapefile-based data at the

50-m scale (AIC= 269.22) (A), 150-m scale (AIC= 265.08) (C), and 500-m scale (AIC= 260.39) (E), and 500-m scale (AIC= 260.39) (E), along with predicted abundances of this species in the Kirby grid from these respective models (B,D,F).

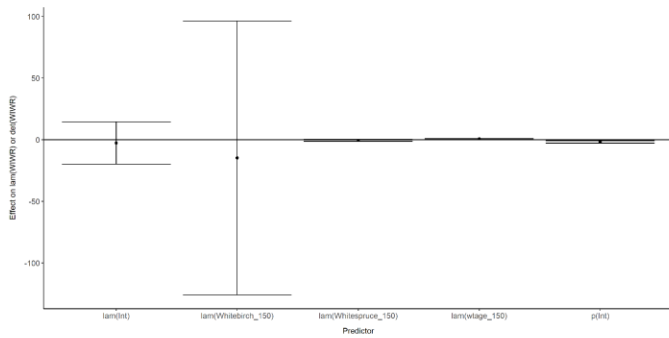
A



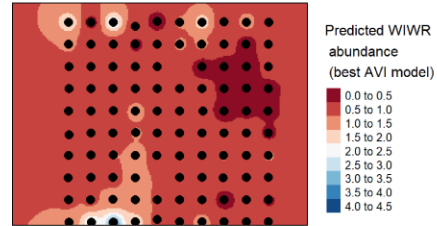
B



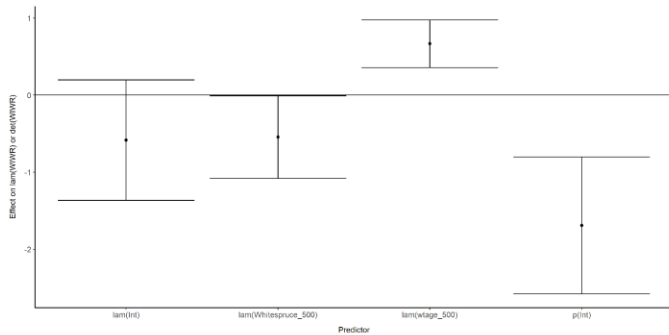
C



D



E



F



Figure 79. Model coefficients for the best N -mixture model predicting abundance of Winter Wren *Troglodytes hiemalis* from satellite-based data at the 50-m scale (AIC= 273.12) (A), 150-m scale (AIC= 272.44) (C), and 500-m scale (AIC= 269.42) (E), along with predicted abundances of this species in the Kirby grid from these respective models (B,D,F).

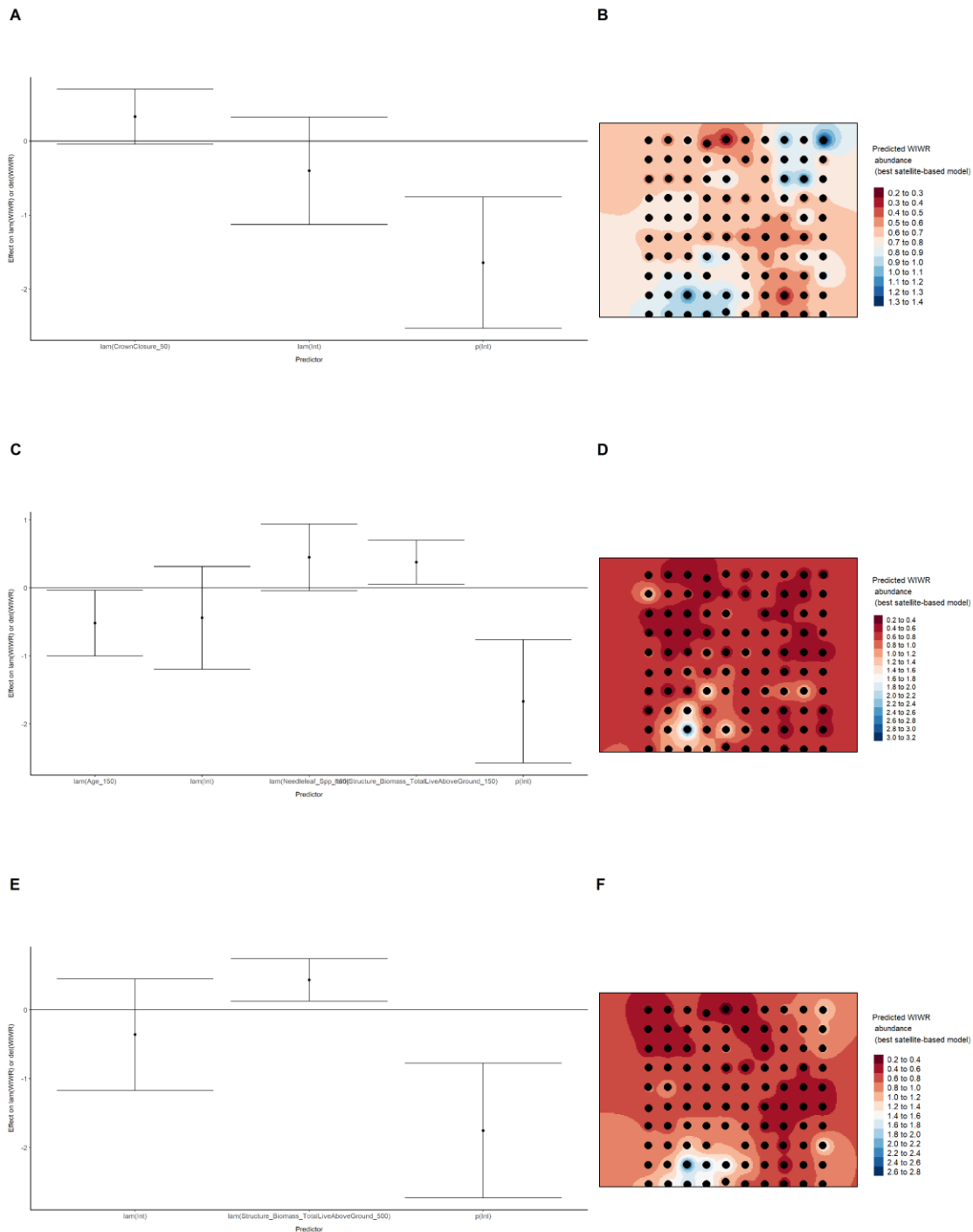


Figure 80. Model coefficients for the best N -mixture model predicting abundance of Winter Wren *Troglodytes hiemalis* from LIDAR-based data at the 150-m scale (AIC= 272.69) (A), and 500-m scale (AIC= 259.32) (C), along with predicted abundances of this species in the Kirby grid from these respective models (B,D).

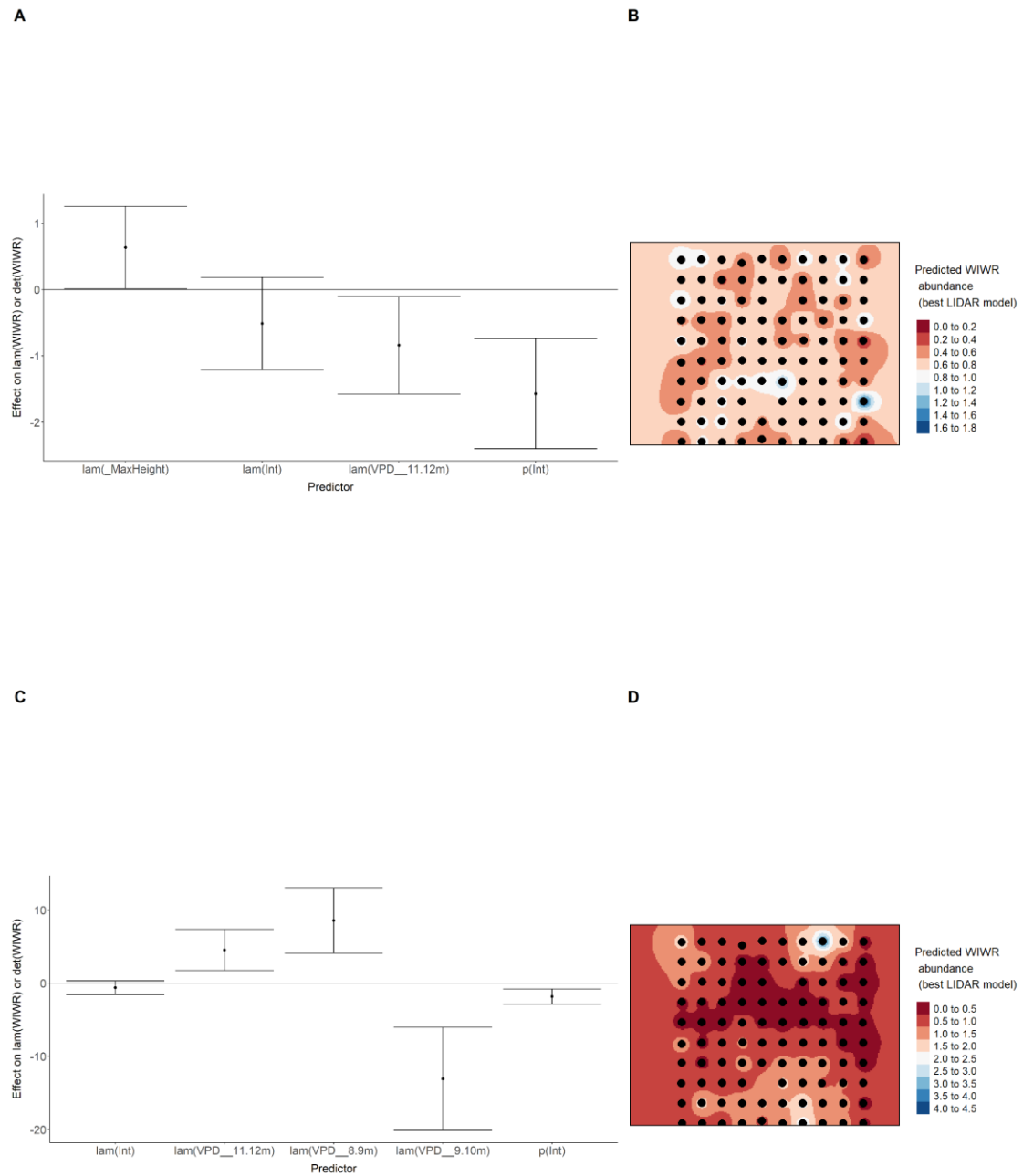


Figure 81. Model coefficients for the A) AVI-based (AIC= 260.39), C) satellite-based (AIC= 269.42), E) lidar-based (AIC= 259.32), and G) composite (AIC= 259.32) N-mixture models predicting abundance of Winter Wren *Troglodytes hiemalis*, along with predicted abundances of this species in the Kirby grid from these respective models (B,D,F,H).

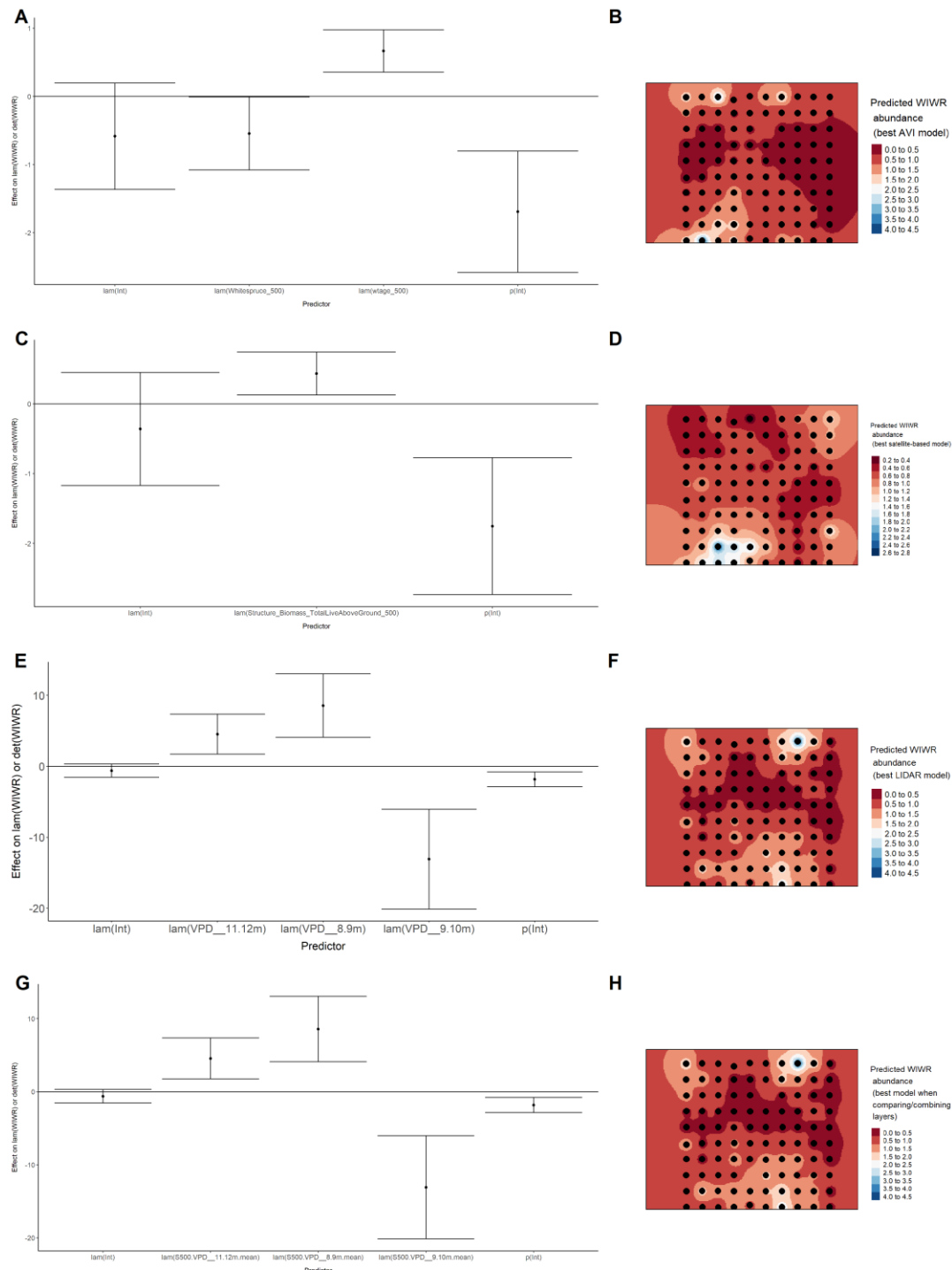
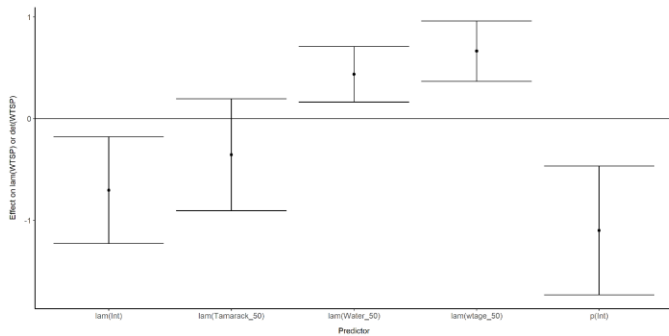


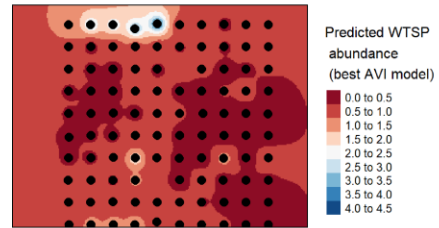
Figure 82. Model coefficients for the best N-mixture model predicting abundance of White-throated Sparrow *Zonotrichia albicollis* from Alberta Vegetation Inventory (AVI) shapefile-based

data at the 50-m scale ($AIC= 321.48$) (A), 150-m scale ($AIC= 322.54$) (C), and 500-m scale ($AIC= 318.9$) (E), along with predicted abundances of this species in the Kirby grid from these respective models (B,D,F).

A



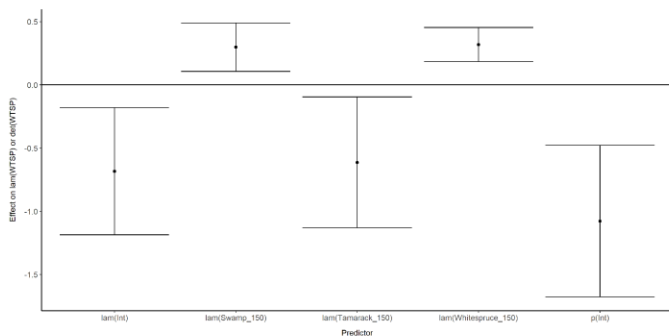
B



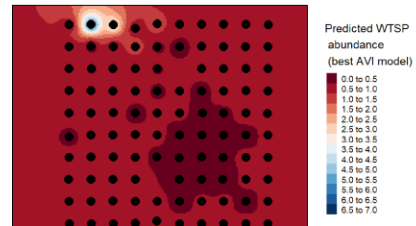
Predicted WTSP abundance
(best AVI model)

- 0.0 to 0.5
- 0.5 to 1.0
- 1.0 to 1.5
- 1.5 to 2.0
- 2.0 to 2.5
- 2.5 to 3.0
- 3.0 to 3.5
- 3.5 to 4.0
- 4.0 to 4.5

C



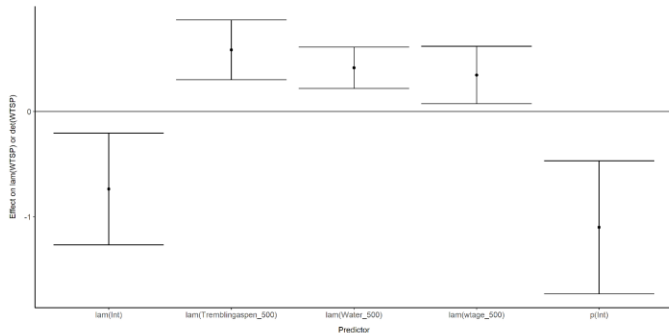
D



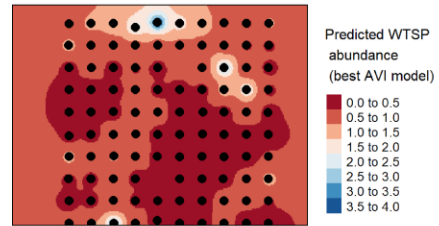
Predicted WTSP abundance
(best AVI model)

- 0.0 to 0.5
- 0.5 to 1.0
- 1.0 to 1.5
- 1.5 to 2.0
- 2.0 to 2.5
- 2.5 to 3.0
- 3.0 to 3.5
- 3.5 to 4.0
- 4.0 to 4.5
- 4.5 to 5.0
- 5.0 to 5.5
- 5.5 to 6.0
- 6.0 to 6.5
- 6.5 to 7.0

E



F



Predicted WTSP abundance
(best AVI model)

- 0.0 to 0.5
- 0.5 to 1.0
- 1.0 to 1.5
- 1.5 to 2.0
- 2.0 to 2.5
- 2.5 to 3.0
- 3.0 to 3.5
- 3.5 to 4.0

Figure 83. Model coefficients for the best N -mixture model predicting abundance of White-throated Sparrow *Zonotrichia albicollis* from satellite-based data at the 50-m scale (AIC= 327.4) (A), 150-m scale (AIC= 326.85) (C), and 500-m scale (AIC= 312.28) (E), along with predicted abundances of this species in the Kirby grid from these respective models (B,D,F).

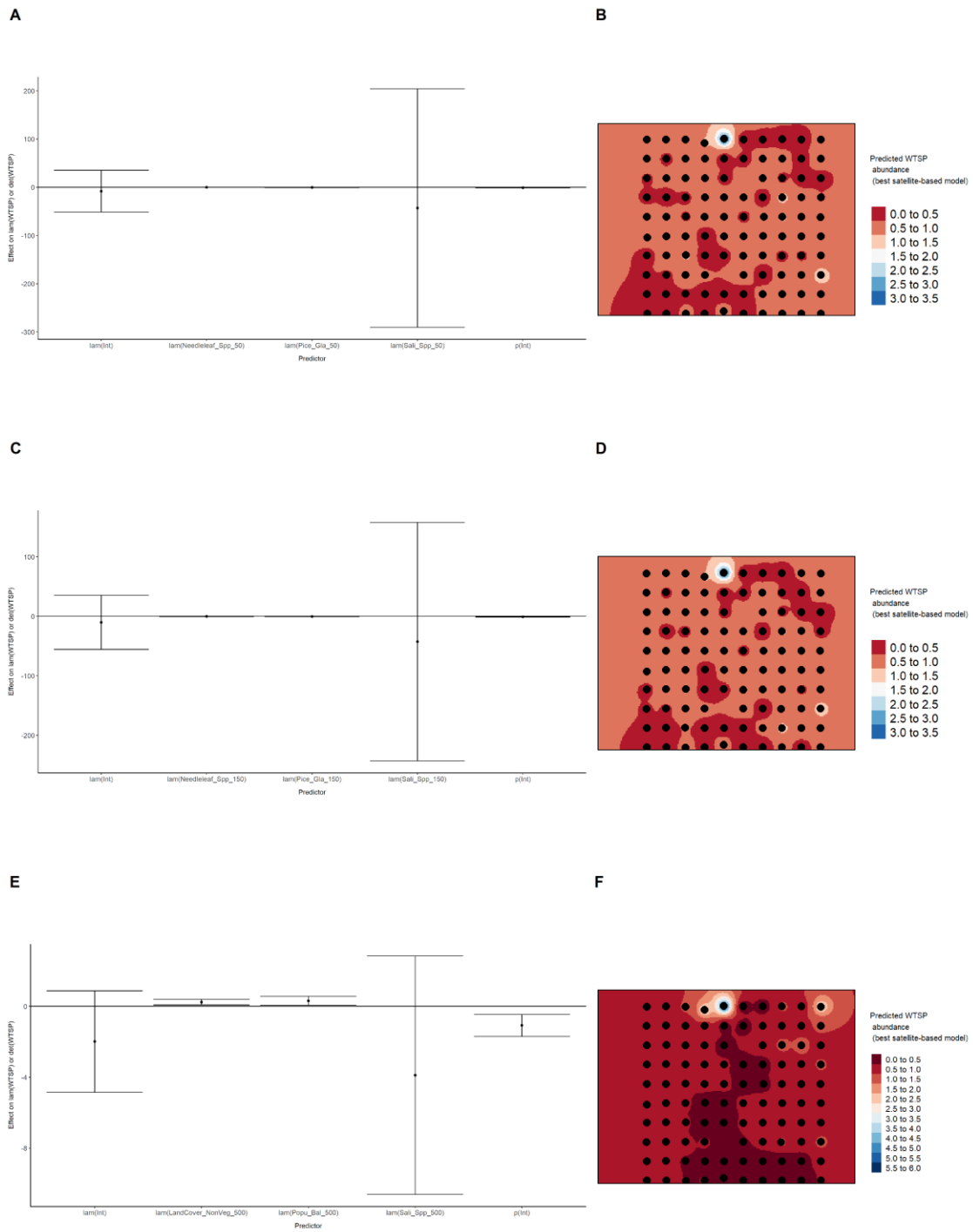


Figure 84. Model coefficients for the best N -mixture model predicting abundance of White-throated Sparrow *Zonotrichia albicollis* from LIDAR-based data at the 150-m scale ($AIC= 331.48$) (A), and 500-m scale ($AIC= 336.91$) (C), along with predicted abundances of this species in the Kirby grid from these respective models (B,D).

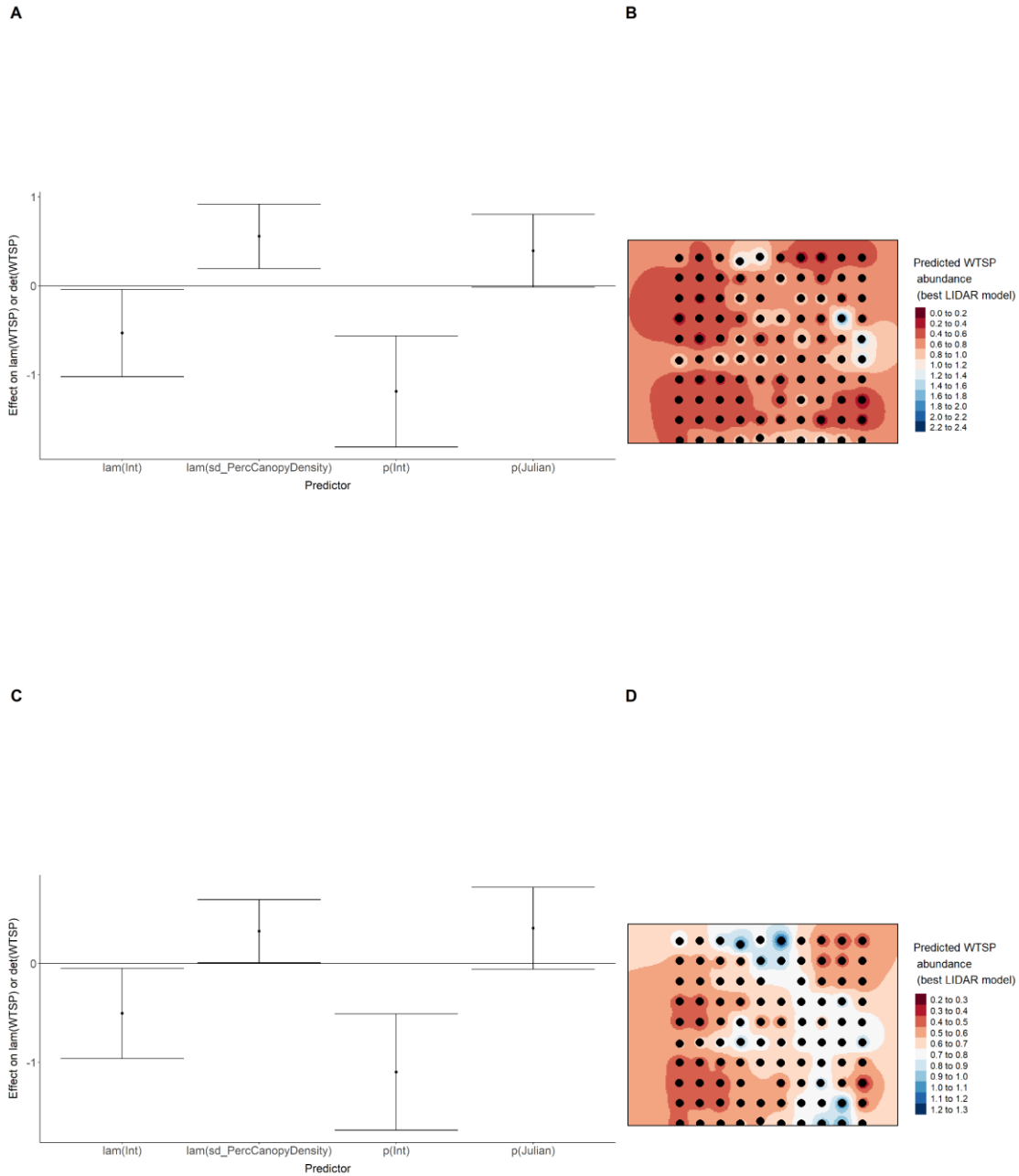


Figure 85. Model coefficients for the A) AVI-based (AIC= 318.9), C) satellite-based (AIC= 312.28), E) lidar-based (AIC= 331.48), and G) composite (AIC= 307.17) *N*-mixture models predicting abundance of White-throated Sparrow *Zonotrichia albicollis*, along with predicted abundances of this species in the Kirby grid from these respective models (B,D,F,H).

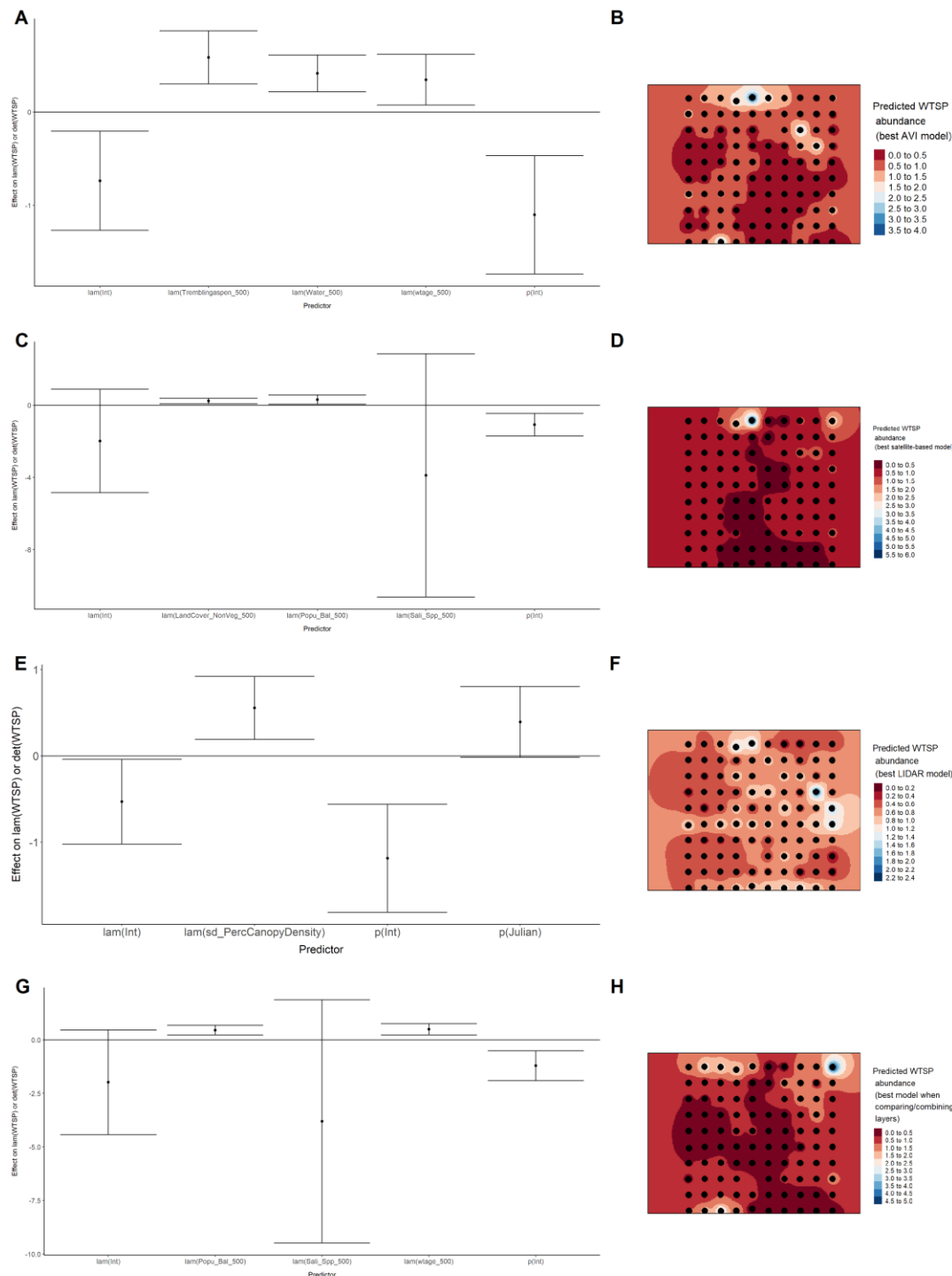
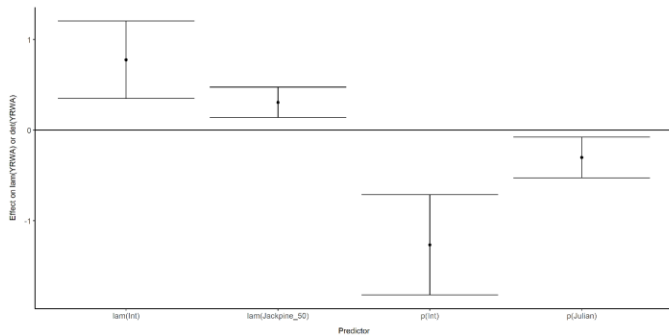


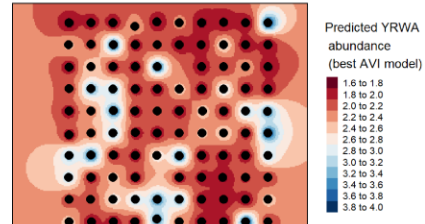
Figure 86. Model coefficients for the best *N*-mixture model predicting abundance of Yellow-rumped Warbler *Setophaga coronata* from Alberta Vegetation Inventory (AVI) shapefile-based

data at the 50-m scale ($AIC= 674.11$) (A), 150-m scale ($AIC= 676.74$) (C), and 500-m scale ($AIC= 682.45$) (E), along with predicted abundances of this species in the Kirby grid from these respective models (B,D,F).

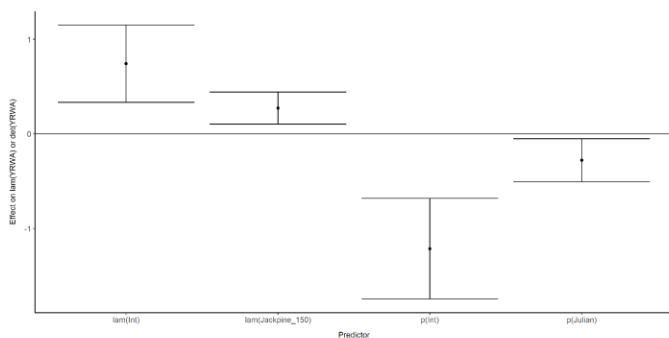
A



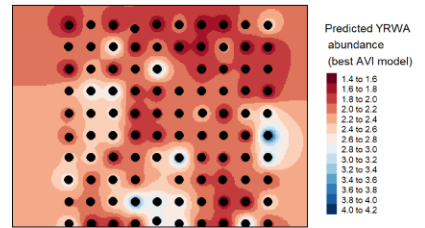
B



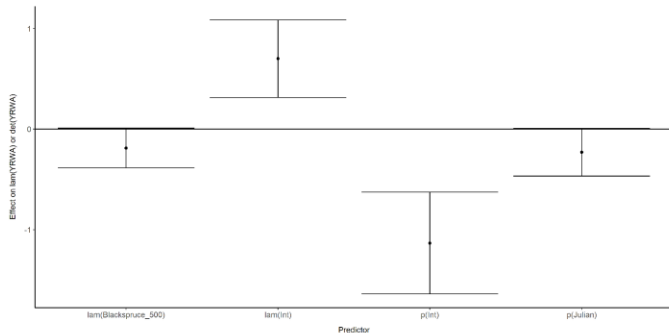
C



D



E



F

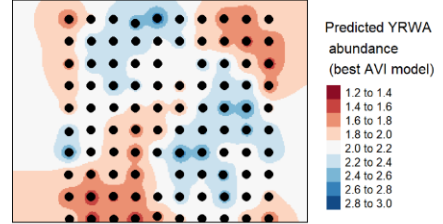


Figure 87. Model coefficients for the best N -mixture model predicting abundance of Yellow-rumped Warbler *Setophaga coronata* from satellite-based data at the 50-m scale (AIC= 679.02) (A), 150-m scale (AIC= 680.76) (C), and 500-m scale (AIC= 683.36) (E), along with predicted abundances of this species in the Kirby grid from these respective models (B,D,F).

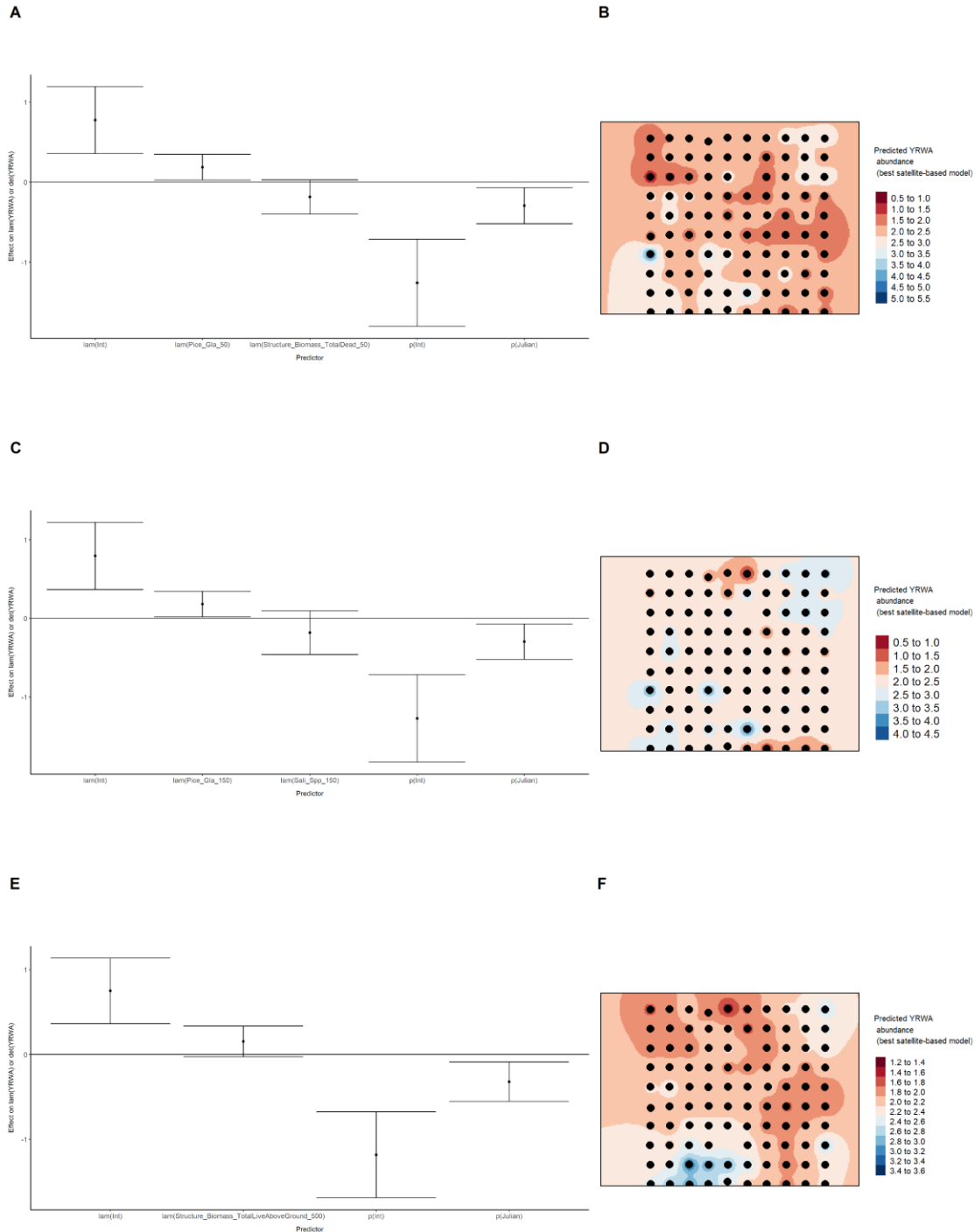
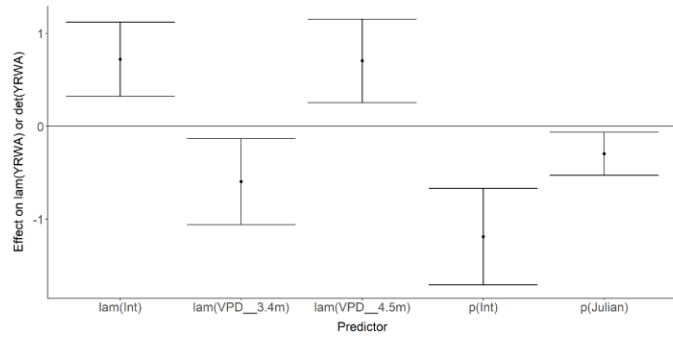
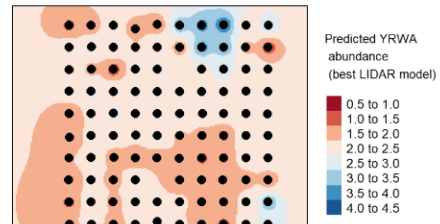


Figure 88. Model coefficients for the best N -mixture model predicting abundance of Yellow-rumped Warbler *Setophaga coronata* from LIDAR-based data at the 150-m scale (AIC= 678.17) (A), and 500-m scale (AIC= 682.21) (C), along with predicted abundances of this species in the Kirby grid from these respective models (B,D).

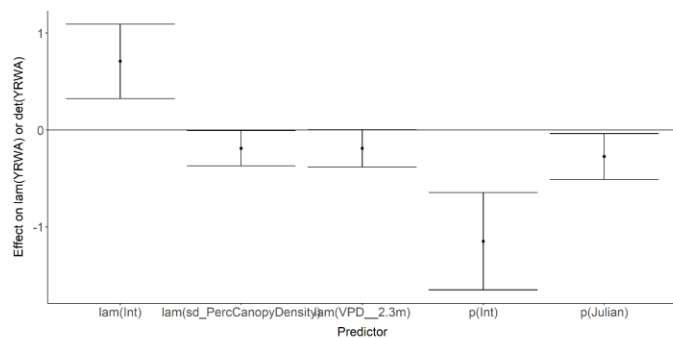
A



B



C



D

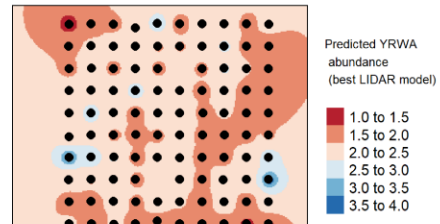


Figure 89. Model coefficients for the A) AVI-based (AIC= 674.11), C) satellite-based (AIC= 679.02), E) lidar-based (AIC= 678.17), and G) composite (AIC= 671.32) N-mixture models predicting abundance of Yellow-rumped Warbler *Setophaga coronata*, along with predicted abundances of this species in the Kirby grid from these respective models (B,D,F,H).

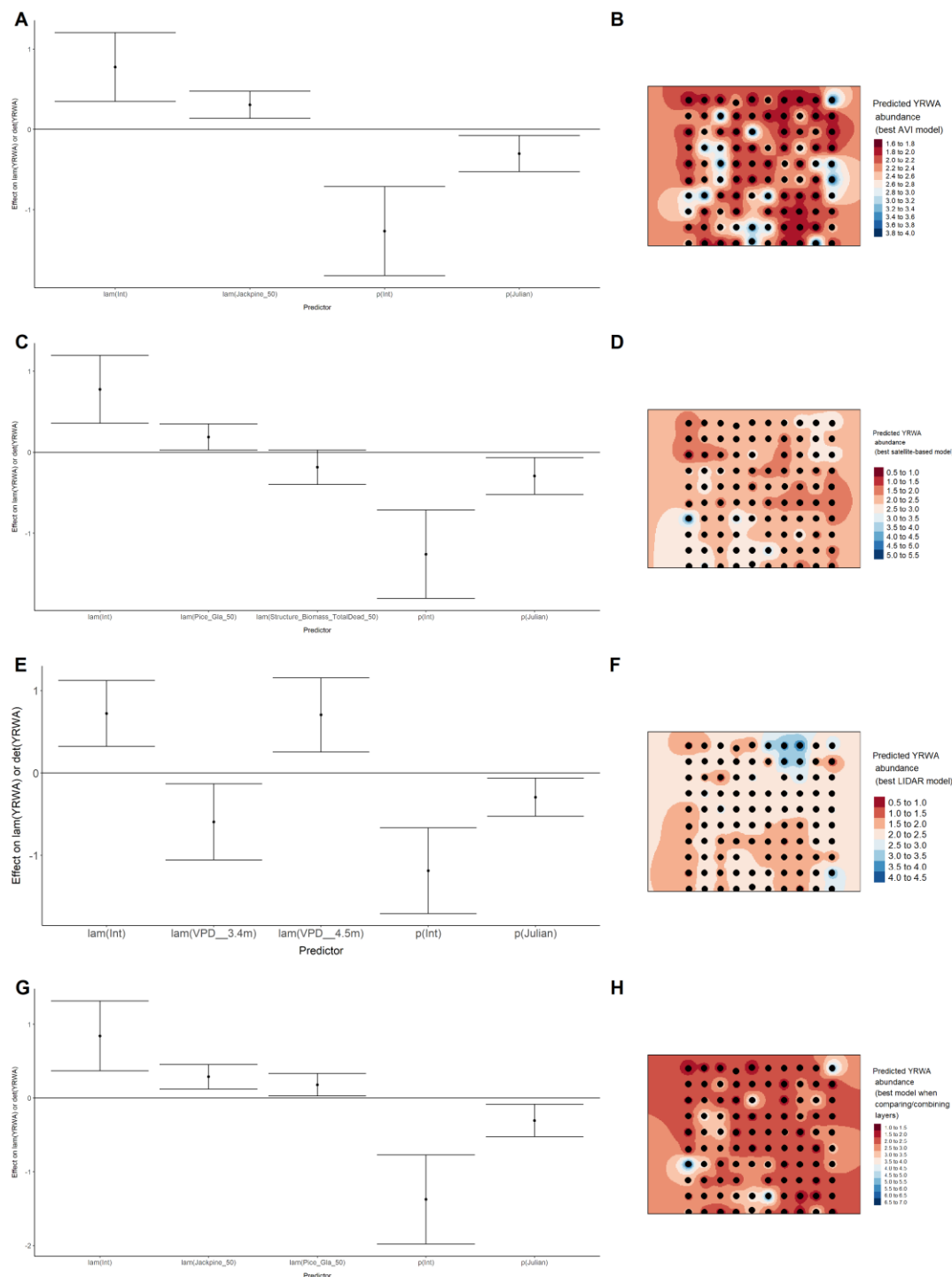
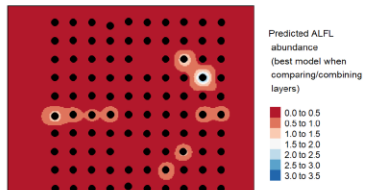
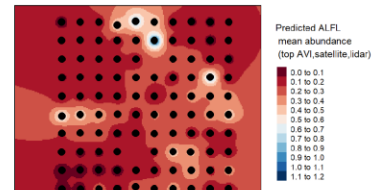


Figure 90. Comparisons of predicted abundance based on the composite model vs. mean predicted abundance from the top AVI, satellite, and lidar models for Alder Flycatcher (*Empidonax alnorum*), American Robin (*Turdus migratorius*), Boreal Chickadee (*Poecile hudsonicus*), and Cedar Waxwing (*Bombycilla cedrorum*).

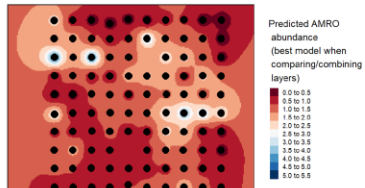
A



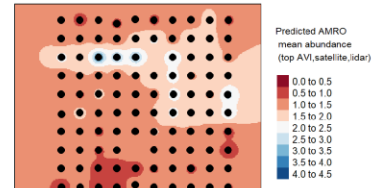
B



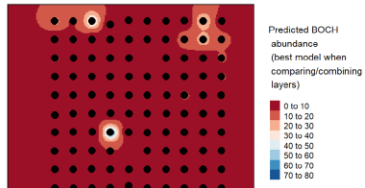
C



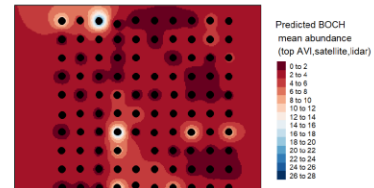
D



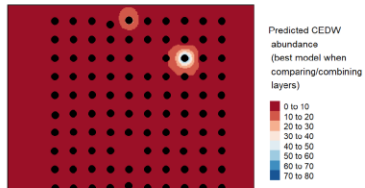
E



F



G



H

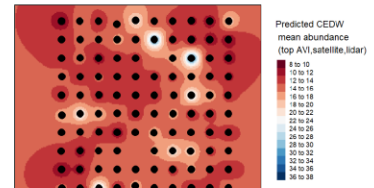
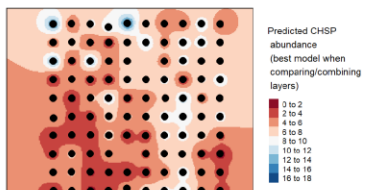
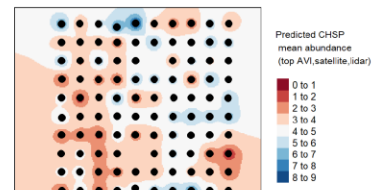


Figure 91. Comparisons of predicted abundance based on the composite model vs. mean predicted abundance from the top AVI, satellite, and lidar models for Chipping Sparrow (*Spizella passerina*), Common Yellowthroat (*Geothlypis trichas*), Dark-eyed Junco (*Junco hyemalis*), and Gray Jay (*Perisoreus canadensis*).

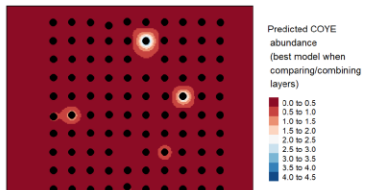
A



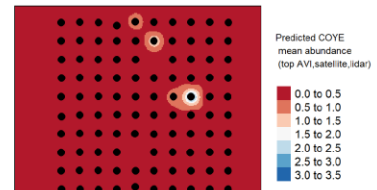
B



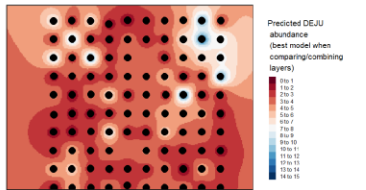
C



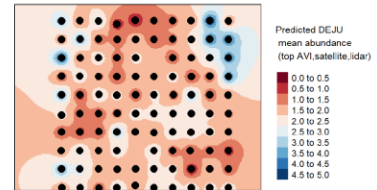
D



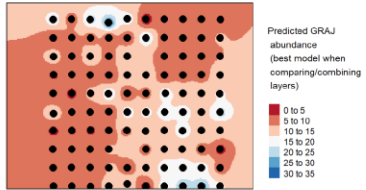
E



F



G



H

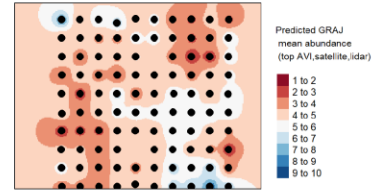
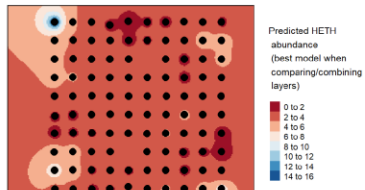
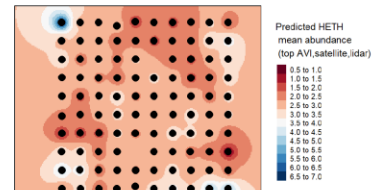


Figure 92. Comparisons of predicted abundance based on the composite model vs. mean predicted abundance from the top AVI, satellite, and lidar models for Hermit Thrush (*Catharus guttatus*), Le Conte's Sparrow (*Ammodramus lecontei*), Olive-sided Flycatcher (*Contopus cooperi*), and Palm Warbler (*Setophaga palmarum*).

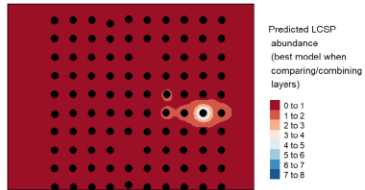
A



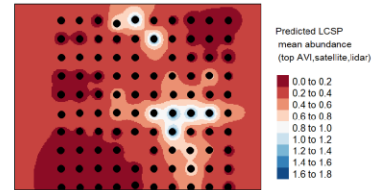
B



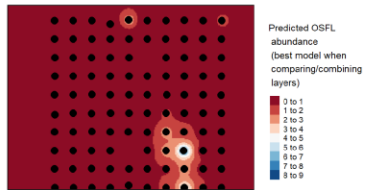
C



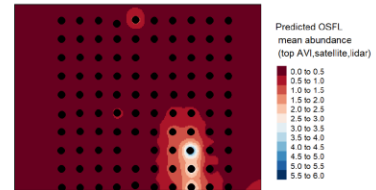
D



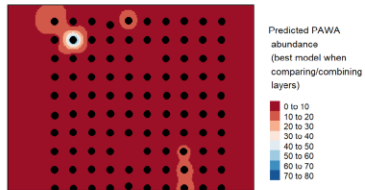
E



F



G



H

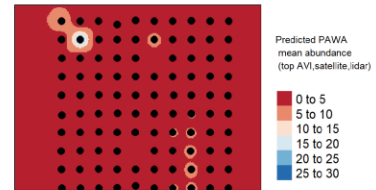
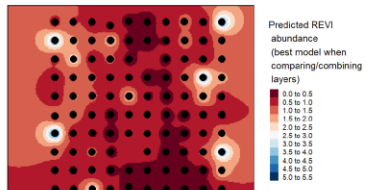
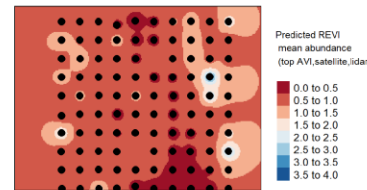


Figure 93. Comparisons of predicted abundance based on the composite model vs. mean predicted abundance from the top AVI, satellite, and lidar models for Red-eyed Vireo (*Vireo olivaceus*), Ruby-crowned Kinglet (*Regulus calendula*), Swamp Sparrow (*Melospiza georgiana*), and Tennessee Warbler (*Leiothlypis peregrina*).

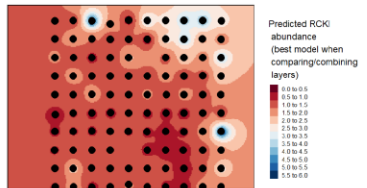
A



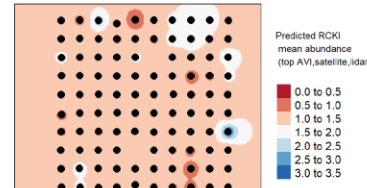
B



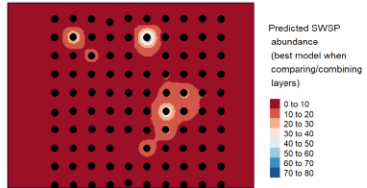
C



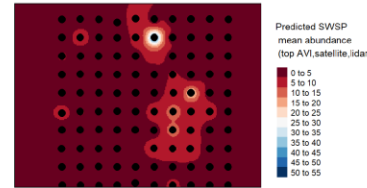
D



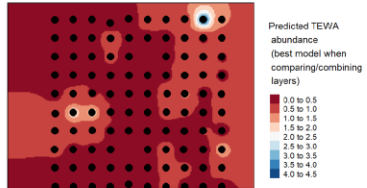
E



F



G



H

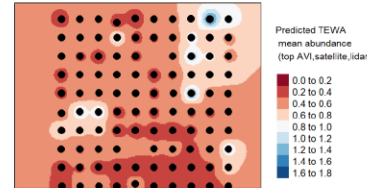
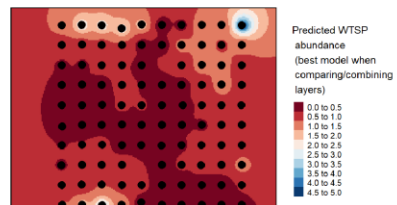
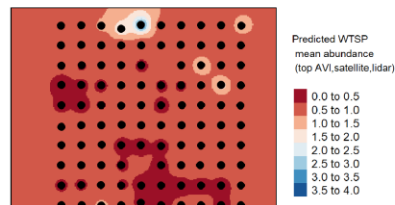


Figure 94. Comparisons of predicted abundance based on the composite model vs. mean predicted abundance from the top AVI, satellite, and lidar models for White-throated Sparrow (*Zonotrichia albicollis*) and Yellow-rumped Warbler (*Setophaga coronata*).

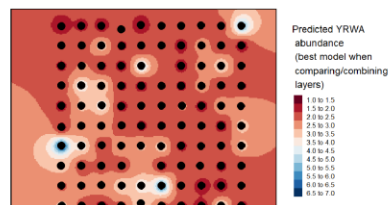
A



B



C



D

